# STUDY OF PHOTOCATALYTIC AND ADSORTIVE BEHAVIOUR OF PURE ZIRCONIUM OXIDE AND CARBON-SULPHUR CO-DOPED ZIRCONIUM OXIDE NANOCOMPOSITES FOR PURIFICATION OF DYE WASTEWATER

**BY**

**ODEH, Emmanuel Igoche**
**MTECH/SPS/2017/7599**

**A THESIS SUBMITTED TO THE POSTGRADUATE SCHOOL FEDERAL UNIVERSITY OF TECHNOLOGY, MINNA, NIGER STATE, NIGERIA IN PARTIAL FULFILMENT OF THE REQUIREMENTS FOR THE AWARD OF DEGREE OF MASTER OF TECHNOLOGY IN ANALYTICAL CHEMISTRY**

**June, 2021**

## ABSTRACT

In this work, $ZrO_2$ nanoparticles were synthesized by green method using *Plumeria acuminata* leaf extract via the variation of pH. Subsequently, carbon and sulphur were incorporated onto the lattice layer of the prepared $ZrO_2$ nanoparticles by wet impregnation method. The prepared undoped, doped and co-doped zirconium oxide based nanomaterials were characterized for their morphology, phase structure, surface area, microstructure, absorption band, crystallinity and elemental composition using HRSEM, XRD, BET, HRTEM, UV-visible and EDS. The photocatalytic and adorptive properties of $ZrO_2$ based materials for the treatment of local dyeing wastewater were investigated. The photocatalytic and adsorptive performance of $ZrO_2$, C-$ZrO_2$, S-$ZrO_2$ and C-S-$ZrO_2$ nanocomposites were determined by measuring the reduction in the level of .the following indicator parameters in local dyeing wastewater (TOC, COD, BOD, $SO_4^{2-}$, $CO_3^{2-}$, $Cl^-$, $NO_3^-$ and pH) in the presence and absence of natural sunlight irradiation. HRSEM analysis revealed the formation of agglomerated spherical particles for $ZrO_2$ alone and mixture of spherical and hexagonal shaped particles for C-S co-doped $ZrO_2$ nanocomposites. The EDS confirmed the presence of Zr and O as the dominant elements for $ZrO_2$ alone and also C and S in C-S-$ZrO_2$ nanocomposites. The XRD pattern of pure $ZrO_2$ and carbon doped $ZrO_2$ revealed the formation of tetragonal phase and doping with sulphur revealed orthorhombic, while the co-doped carbon-sulphur $ZrO_2$ revealed a mixture of tetragonal and orthorhombic phases. The crystalline size decreases with addition of the dopants in the order of $ZrO_2$(20.03 nm), S-$ZrO_2$ (17.51 nm), C-$ZrO_2$(16.03 nm) and C-S-$ZrO_2$ (12.40 nm). Optical characterization of the nanomaterial revealed reduction of band gap from 5.2 eV to 3.4 eV for $ZrO_2$ and C-S-$ZrO_2$ respectively. The BET analysis revealed increase in the surface area upon the addition of the dopants in the order of C-S-$ZrO_2$ (80.165 $m^2/g$) >.C-$ZrO_2$ (52.637 $m^2/g$)>.S-$ZrO_2$(24.824 $m^2/g$)> $ZrO_2$ (10.682 $m^2/g$). It was found that the photocatalytic and adsorptive behaviour of the four materials differ with respect to the target pollutants. Of all the four samples studies, C-S-co-doped $ZrO_2$ nanocomposites with highest mesoporosity exhibited excellent photocatalytic activity under natural sunlight than carbon doped $ZrO_2$ , sulphur doped $ZrO_2$ and $ZrO_2$ alone with TOC, COD, BOD, $Cl^-$, $NO_3^-$ and pH removaal efficiency of 97.7%, 77.3%, 87.6%, 63.9%, 84.4%, 70.3%, 83.3% and 19.4% within 120 minutes respectively. The order of adsorptive behaviour of the four samples for the removal of TOC, COD, BOD, $Cl^-$, $NO_3^-$ and pH were C-S-$ZrO_2$ (82.9%) >.C-$ZrO_2$ (82.7%)>.S-$ZrO_2$(81.7%)> $ZrO_2$ (80.3%). This study revealed carbon-sulphur co-doped $ZrO_2$ have excellent adsorption and photocatalytic properties for the removal of target pollutants from local dyeing wastewater except for COD, BOD, $Cl^-$, $SO_4^{2-}$ and $CO_3^{2-}$ that were above the permissible limits.

## TABLE OF CONTENTS

**LIST OF TABLES**

## LIST OF FIGURES

## LIST OF PLATES

## LIST OF ABBREVIATIONS

| | |
|---|---|
| BET | Brunauer-Emmett-Teller |
| BOD | Biological Oxygen Demand |
| COD | Chemical Oxygen Demand |
| DO | Dissolved Oxygen |
| EDS | Energy dispersive X-ray spectroscopy |
| EPA | Environmental Protection Agency |
| HRSEM | High Resolution Scanning Electron Microscope |
| HRTEM | High Resolution Transmission Electron Microscope |
| IUPAC | International Union of Pure and Applied Chemistry |
| TDS | Total Dissolved Solids |
| TEM | Transmission Electron Microscopy |
| UV | Ultraviolet |
| WHO | World Health Organization |
| XRD | X-ray diffraction |

# CHAPTER ONE

## 1.0 INTRODUCTION

### 1.1 Background to the Study

Local dyeing industry is one of the oldest and most complex due to consumption and generation of high amount of wastewater (Kaliraj *et al.,* 2019). It is a known fact that most textile industries in Nigeria have folded up due to enabling environment and lack of managerial skills (Mondal *et al.,* 2017). As a consequence, there has been increased number of indigenous dyeing industries across the country due to the increasing demand of the citizens for the dye fabrics (Yaghoubi *et al.,* 2020). This cottage industry accounts for two third of the total dyestuff market, and during dyeing process approximately 10-15% of the dye used are released into the wastewater (Aneyo *et al.,*2016). These activities are widely recognized as the root cause of environmental pollution because the wastewater contains complex organic aromatic compounds and colours that can cause several health problems (Kaliraj *et al.,* 2019). The effect of exposure to such wastewater includes skin irritation, diarrhea, vomiting, bladder cancer depending on the length of time of exposure and concentration (Zhang *et al.,* 2019).

The treatment of local dyeing wastewater using membrane separation process, equalization and sedimentation, coagulation and sedimentation have proved to be insufficient in removing colour, toxic organic dyes and inorganic constituents (Yaghoubi *et al.,* 2020). Conventional treatment techniques suffer from high application cost, low treatment efficiency and severe secondary pollution. Therefore, it is critical and urgent to develop cost effective and sustainable technology to treat local dyeing

wastewater. Recently, advance oxidation processes (AOPS) have attracted attention due to their strong ability to treat complex industrial wastewater containing organic pollutants (Ameta *et al*., 2018). Among the AOPS, photocatalytic technology is considered as a primary wastewater technique due to its high efficiency, environmental protection and eco-friendliness. In fact some dyes are difficult to biodegrade, particularly, the azo types, reactive and certain acidic dyes which are not readily absorbed by active sludge (Zhang *et al.,* 2019).

In the recent times, metal oxides nanoparticles such as $TiO_2$, $ZrO_2$, $WO_3$, ZnO have been widely used in the area of environmental remediation particularly $ZrO_2$ semiconductor due to its low cost, physical and chemical stability, excellent photocatalytic properties under an excitation by UV or visible light through absorption, scattering and reflection of light (Mondal *et al.,* 2017). The optical, mechanical, electrical, chemical and photocatalytic properties of this material ($ZrO_2$) made it suitable for different applications (Zarei *et al.*, 2019). However, the band gap of $ZrO_2$ in the range of 5-7eV is high and hence limits its photocatalytic activity in the visible region. To reduce this band gap, several strategies has been adopted including the incorporation of metallic and non-metallic elements as dopants (Yadav *et al.*, 2020). Doping using metal or non-metal alone has not been able to show any significant band gap reduction, while metal doping in most cases produced controversial photocatalytic activity results at both above UV and visible wavelengths (Mondal *et al.*, 2017). In addition, metal doping with $ZrO_2$ also cause thermal instability, an increase of carrier-recombination centres (Kianfar *et al.,* 2021). Other effects include, dopant insolubility, the formation of secondary phase or surface aggregation rather than substitution, phase transformation among the polymorphs (Kianfar *et al.,* 2021). There is also problem of

alteration of charged carrier diffusion length and narrow band bending, amongst others (Melchor-Lagar *et al.*, 2020). In view of these, non-metal doping has been identified as a more viable strategy to reduce the band gap and hence improve the visible light driven photocatalytic activity of $ZrO_2$ (Danilenko *et al.*, 2018). Co-doping of $ZrO_2$ nanoparticle with non-metals is expected to bring about a significant reduction in band gap and enhancement of photocatalytic properties of $ZrO_2$ (Zhang *et al.*, 2019). Non-metal elements such as C, N, P , S, and B has been doped with metal oxides and enhanced visible light driven photocatlytic activity was observed (Renuka *et al*., 2021). Carbon and sulphur have strong oxidizing ability and ionic radius of 180 pm and 170 pm respectively (Sun *et al*., 2018). These values are greater than the ionic radius of oxygen (152 pm) which allows the two (non-metal) to displace oxygen from $ZrO_2$ and form zirconium carbide and zirconium sulphide respectively. Moreso, researches have shown that effective band gap narrowing take place as a result of the mixing of the 2p and 3p state of carbon and sulphur with the 2p state of oxygen in $ZrO_2$ (Farag *et al*., 2020). Till date, satisfactory results in terms of appropriate band gap and photocatalytic performance of $ZrO_2$ under visible light have not been reported on the degradation of organic pollutants. Efforts are still ongoing towards developing highly visible light driven photo-catalyst with enhanced efficiency.

In this work, $ZrO_2$ nanoparticle was synthesized and co-doped with carbon and sulphur via combination green synthesis and wet impregnation method. Subsequently, the synthesized materials were analyzed using several characterization tools to ascertain its morphology, microstructures, elemental composition, crystallinity, phase structure, surface area. The photocatalytic/adsorptive properties of the synthesized carbon-sulphur

co-doped $ZrO_2$ nanoparticles on local dyeing wastewater in the presence or absence of sunlight was investigated.

## 1.2 Statement of the Research Problem

Local dyeing wastewater constitute a serious threat to the environment, especially in the aquatic environment because it contains considerable amount of heavy metals, oil, grease and organic aromatic compounds (Aneyo *et al.,* 2016). Exposure to local dyeing wastewater could lead to several health problems such as skin irritation or bleaching of skin depending on the dose and time (Mondal *et al.*, 2017).

The local dyeing wastewater unlawfully discharged into aquatic eco-system depleted the dissolve oxygen content, chemical oxygen demand, biochemical oxygen thereby making life difficult for aquatic species (Aghabeygi and Khademi-Shamami, 2018). In addition, more than 80% of the local dyeing wastewater is coloured due to reactive dyes and the presence of coloured wastewater is an evidence of high biological oxygen demand (BOD) values and low dissolved oxygen (Aghabeygi and Khademi-Shamami, 2018).The treatment of wastewater from local dyeing industry involving the use of membrane separation process, equalization and sedimentation, coagulation and sedimentation have proved to be insufficient in removing colour, toxic organic dyes and inorganic constituents (Danilenko *et al.,* 2018). Some of these organic dyes are difficult to degrade, particularly the reactive and certain acidic dyes are not readily absorbed by active sludge. Physical and chemical methods of preparing $ZrO_2$ nanoparticles namely vapour phase, pyrolysis, hydrolysis, precipitation, hydrothermal and microwave plasma

has shown problems of complicated procedure, high reaction temperature, long reaction time, toxic reagent and high cost of production which makes it difficult to produce $ZrO_2$ nanoparticles in a large scale. Mono doping of $ZrO_2$ nanoparticle with metal did not cause a significant band gap reduction, while the co-doping with two metals shows controversial photo-catalytic properties in thin film and bulk sample (Zhang *et al.*, 2019).

### 1.3 Justification of the Study

Adsorption and photocatalytic technology in lieu of other conventional methods is expected to reduce the COD, BOD, TOC, DO level in the local dyeing wastewater. Adsorption and photocatalytic treatment of local dyeing wastewater by carbon-sulphur doped $ZrO_2$ nanocomposite is expected to remove toxic dyes and inorganic constituents from wastewater (Aneyo *et al.,* 2016). Green synthesis method of producing nanoparticles is simple and less complicated and operates at a very low temperature compared to other physical and chemical synthesis methods (Shinde *et al.,* 2018). Co-doping of $ZrO_2$ nanoparticles with non-metals with 2p electrons such as carbon and sulphur is expected to show effective band gap reduction, increased surface area and enhance photo activity under visible light (Aneyo *et al.*, 2016). Carbon and sulphur have the ionic radius of 180pm and 170pm respectively. This values is greater than the ionic radius of oxygen (152pm) which allows the two to displace oxygen from $ZrO_2$ and form zirconium sulphide and zirconium carbide respectively (Kianfar *et al.*, 2021).

### 1.4 Aim and Objectives of the Study

The aim of this study is to synthesize, characterize and examine the catalytic and adsorptive properties of carbon-sulphur co-doped zirconium oxide nanocomposite for the purification of local dyeing wastewater.

The aim was achieved through the following objectives;

(i) Synthesis of zirconium oxide nanoparticles based on variation of solution pH.

(ii) Incorporation carbon and sulphur onto the prepared $ZrO_2$ nanoparticles.

(iii) Characterization of zirconium oxide ($ZrO_2$), carbon doped $ZrO_2$, sulphur doped $ZrO_2$ and carbon-sulphur co-doped $ZrO_2$ nanocomposite using different analytical tools.

(iv) Physico-chemical analysis of the local dyeing wastewater for (pH, COD, BOD, TOC, DO, $Cl^-$, $NO_3^-$, $SO_4^{2-}$, $PO_4^{2-}$) before and after adsorptive and photocatalytic experiment.

(v) Evaluation of the adsorptive and photocatalytic behaviour of $ZrO_2$, carbon doped $ZrO_2$, sulphur doped $ZrO_2$ and carbon-sulphur co-doped $ZrO_2$.

(vi) Evaluation of the adsorptive/photocatalytic data using different kinetic models (parabolic, pseudo-first, modified freundlich and zero order)

# CHAPTER TWO

# 2.0 LITERATURE REVIEW

## 2.1 Zirconium Oxide ($ZrO_2$)

Zirconium(IV) oxide ($ZrO_2$), also referred to as zirconia is a white crystalline oxide of zirconium which occurs naturally and can be converted to other forms (Anandan *et al.,* 2020). $ZrO_2$ is chemically inert and can be slowly attacked by concentrated hydrofluoric acid and sulfuric acid (Renuka *et al.,* 2021). It can be converted to zirconium carbide on exposure to heat with carbon or formed zirconium tetrachloride when exposed to heat with carbon in the presence of chlorine. $ZrO_2$ is amongst the most widely studied nanomaterials containing three crystal structures of which depends on temperature (Renuka *et al.,* 2021). $ZrO_2$ adopts a monoclinic crystal structure at room temperature and converted to tetragonal and cubic at higher temperatures (Saraswathi *et al.,* 2017). The induce stress may be responsible for the change of volume transition of structure from tetragonal to monoclinic to cubic induces in most cases, which cause cracking upon cooling from high temperatures (Sasaki *et al*., 2017). However, the blending of $ZrO_2$ with some other oxides caused the stability of the tetragonal and/or cubic phases.

The incorporation of dopants such as magnesium oxide (MgO), yttrium oxide ($Y_2O_3$, yttria), calcium oxide (CaO), and cerium(III) oxide ($Ce_2O_3$) may however improve the stability of cubic/tetragonal phase (Sigwadi *et al.,* 2017).

$ZrO_2$ becomes more useful especially when the phase is 'stabilized' upon heating and can undergo disruptive phase changes when small percentages of ytterbium oxide were added (Bharathi *et al.,* 2020). These phase transformation often resulted to preparation of material with superior thermal, mechanical, and electrical properties (Anandan *et al.,* 2020). On the other hand, the tetragonal phase can be metastable and can be converted to monoclinic depending on the applied stress which often can cause the associated volume expansion. This phase transformation can convert the crack into compression, retarding its growth, and enhancing the fracture toughness (Gurushantha *et al.,* 2017). This mechanism is known as transformation toughening, and significantly extends the reliability and lifetime of products made with stabilized $ZrO_2$ (Sigwadi *et al.,* 2017). Also, $ZrO_2$ is widely studied due to its physical and chemical characteristics, low cost, high stability and environmental friendliness (Chen *et al.,* 2017). The various phases of $ZrO_2$ is shown in Fig 2.1.

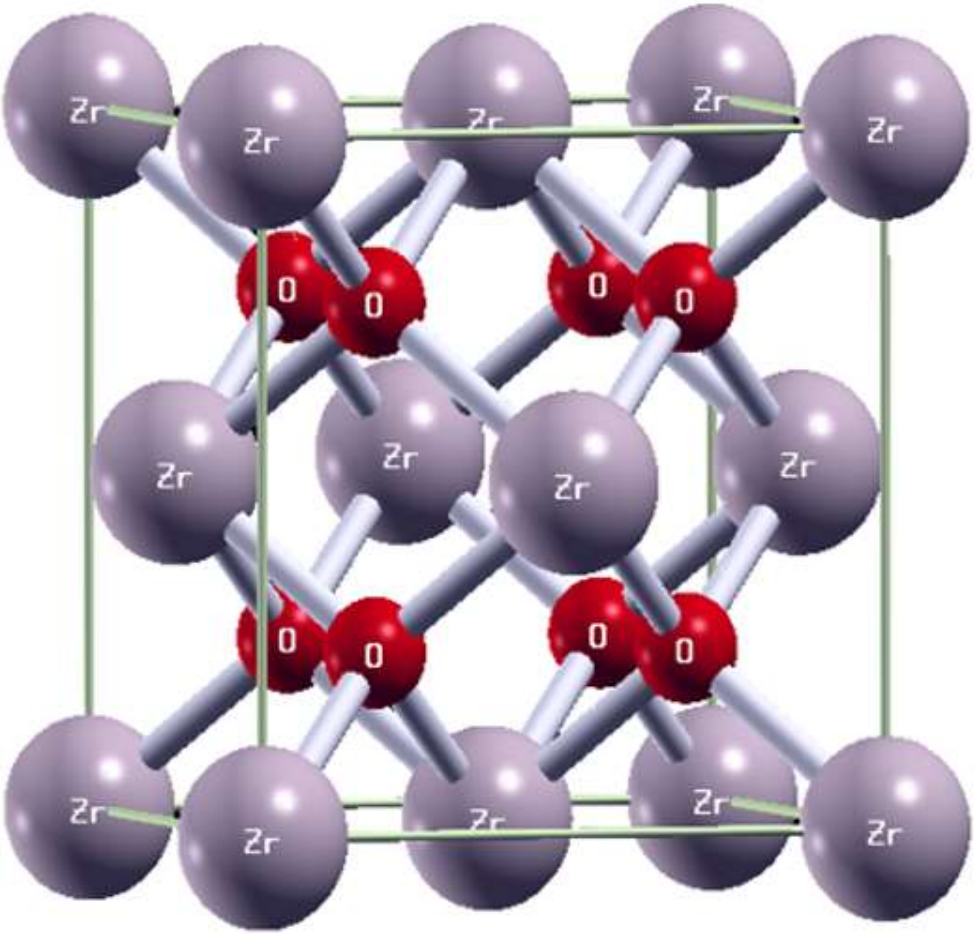


**Figure: 2.1 Crystal structure of Pure zirconium oxide** ( Sigwadi *et al.*, 2017).

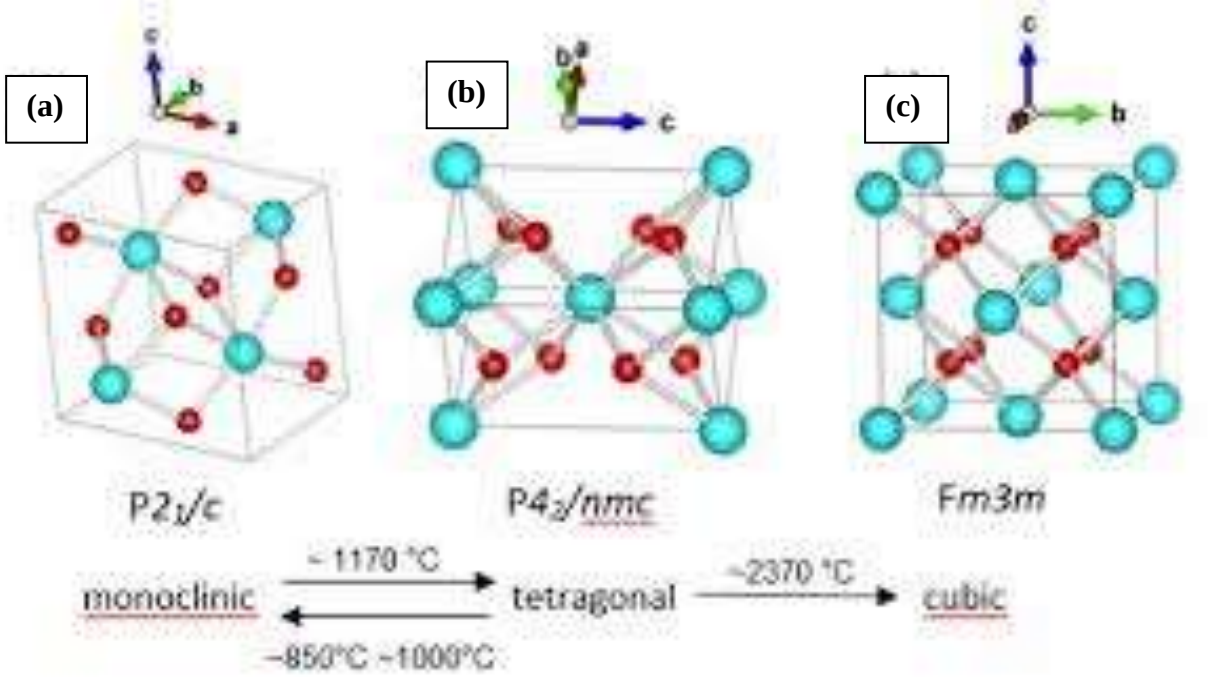


**Figure: 2.2 Crystal structure of (a) monoclinic (b) tetragonal (c) cubic phase of $ZrO_2$** ( Sigwadi *et al.,* 2017).

## 2.2 Photocatalysis

Photocatalysis is the acceleration of photoelectrons from the valence band to conduction band of a semiconductor metal oxide catalyst and light source (UV-Visible light) (Dharr *et al.,* 2020). In $ZrO_2$, the photocatalytic activity is dependent on the ability of the catalyst to create electron-hole pairs which generate free radical such as hydroxyl (OH) radical and able to undergo secondary reactions (Mondal *et al.,* 2017). Zirconia was found to be photocatalytically active for the degradation of anionic dyes such as orange G, amido black, remazol brilliant blue R, and alizarin green under sunlight irradiation (Mondal *et al.,* 2017). Furthermore, Fe doped $ZrO_2$ has shown controversial photocatalytic activity under both UV and visible wavelength, complicated thermal instability, an increase in career recombination centre (Shinde *et al.,* 2018). Other problems of metal doped $ZrO_2$ nanoparticles include dopant insolubility, formation of

secondary phase aggregation rather than substitution, phase transformation amongst others (Sun *et al.*, 2018). While non-metal doped zirconia ( N, C, S) shows viable band gap reduction and enhance visible light driving photocatalytic activities (Shinde *et al.*, 2018).

### 2.3 Adsorption Technology

The adhesion of atoms, ions, or molecules from a gas, liquid, or dissolved solid to a surface is known as adsorption. This procedure forms an adsorbate coating on the adsorbent's surface. This differs from absorption, which occurs when a fluid (the absorbate) dissolves or permeates a liquid or solid (the absorbent). Adsorption is a surface phenomenon, whereas absorption affects the entire volume of the substance; yet, adsorption frequently occurs before absorption (Muya *et al*., 2016). Both processes are referred to as sorption, while desorption is the opposite. Adsorption occurs as a result of surface energy. In a bulk material, all of the constituent atoms' bonding requirements (whether ionic, covalent, or metallic) are met by other atoms in the substance. However, because atoms on the adsorbent's surface are not completely surrounded by other adsorbent atoms, they can attract adsorbates (Aghabeygi and Khademi-Shamami, 2018). The exact nature of the bonding relies on the specifics of the species involved, however the adsorption process can be classed as either physisorption (characterized by mild van der Waals forces) or chemisorption (characterized by strong van der Waals forces) (characteristic of covalent bonding). Electrostatic attraction may also play a role. Aluminium oxide ($Al_2O_3$), Zinc oxide (ZnO), Zirconium oxide ($ZrO_2$) and Titanium oxide ($TiO_2$) amongst others have been used as nanoadsorbents and excellent adsorptive efficiency has been reported (Luengas *et al*., 2015).

## 2.4 Mechanism of Zirconium Oxide Nanoparticles

The mechanism of $ZrO_2$ nanoparticles lie in its ability to create electron hole pairs and generates free reactive species such as hydroxyl radicals ($OH^{\cdot}$) which is able to react selectively with organic compounds (Chen *et al.*, 2017). The chain of reactions leading to the formation of hydroxyl radicals are shown in figure 2.1 to 2.5.

$$ZrO_2 + hv \longrightarrow h^+vB + e^-CB \quad (2.1)$$

$$H_2O + h^+vB \longrightarrow H^+ + {\cdot}OH \quad (2.2)$$

$$O_2 + e^-CB \longrightarrow O_2^{\cdot} \quad (2.3)$$

$$2H_2O + 2O_2 \longrightarrow H_2O_2 + O_2 \quad (2.4)$$

$$H_2O_2 + e^-CB \longrightarrow 2HO^{\cdot} \quad (2.5)$$

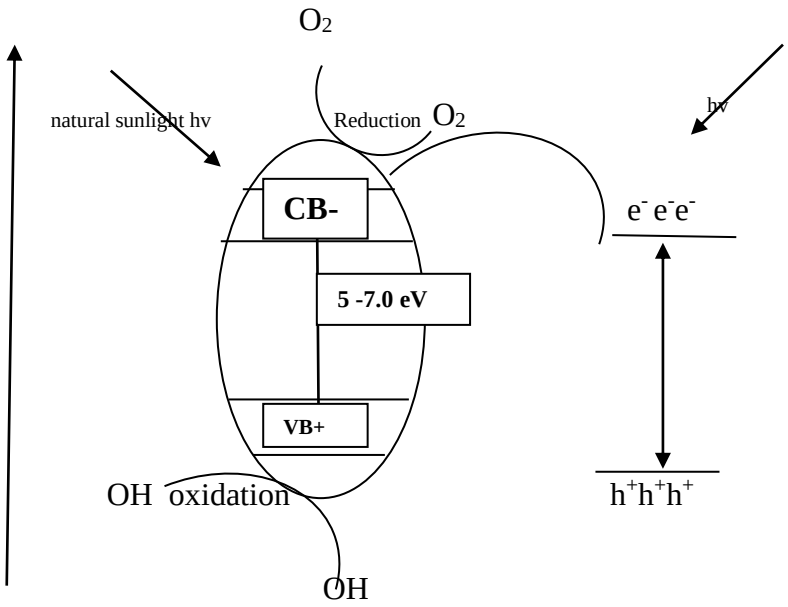


**Figure 2.3 Mechanism of reaction of $ZrO_2$ under light source**

## 2.5 Shortcomings of Zirconium Oxide

One of the major shortcomings of $ZrO_2$ is the wide band gap (5-7eV) which limits photoactivity in the visible region (Dharr *et al.*, 2020). This wide band gap allows it to operate at a very high volatge, frequency and temperature. This wide band gap contribute to its low photocatalytic activity under UV and visible light source.In addition, $ZrO_2$ nanoparticles also have low surface area which may be responsible for its low photocatalytic activity under UV and visible light sources. Furthermore, $ZrO_2$ nanoparticles are easy to agglomerate and challenging to recover due to the nanocrystalline size, which seriously limits its practical application.

## 2.6 Doping of Zirconium Oxide

Doping of $ZrO_2$ is a method of incorporating metallic or non-metallic impurities into $ZrO_2$ lattice layer to reduce the band gap; to change the properties and crystal phase of $ZrO_2$ and also enhance its surface area (Gautam *et al.*, 2016).

### 2.6.1 Doping of $ZrO_2$ nanoparticles with metals

Doping of $ZrO_2$ with metal is a method of incorporating metallic material onto $ZrO_2$ to reduce its band gap and hence improve its photoactivity (Feng *et al.,* 2019). Metal doping has shown controversial photocatalytic activity results at both above UV and visible wavelengths (Aghabeygi and Khademi-Shamami, 2018). For instance, Arjun *et al.,* (2020) prepared copper doped $ZrO_2$ nanoparticles via solgel technique and found that the addition of copper was responsible for the reduction of band gap energy from 3.35 to 3.27 eV. For instance, Song *et al.* (2019) employed chemical method to prepared Iron doped $ZrO_2$ nanoparticles and found that the surface area of $ZrO_2$ reduced on the introduction of Fe dopant from 143.93 $m^2/g$ to 104.3 $m^2/g$. In the same vein, Rajesh *et*

*al.* (2020) doped magnesium with $ZrO_2$ via increase in concentration of dopant from (0.2M-0.8M) and the photocatalytic degradation efficiency was found to increase from 70% to 94% upon increase in Mg dopant concentration. Similarly, Muhammad *et al.* (2021) doped $ZrO_2$ nanoparticles with chromium and tested for the degradation of methylene blue under UV light and the degradation efficiency of the catalyst decreased from 78.41% to 73.07% upon increase in the amount of dopant from 1 g to 3 g.

### 2.6.2 Doping of zirconium oxide nanoparticles with non-metal

Doping of $ZrO_2$ with non-metal involves incorporation of non-metallic elements onto the lattice layer of $ZrO_2$ in order to reduce its band gap and enhance its photoactivity (Mishra *et al.,* 2021). Non-metal elements such as C, I, P, S, and B has been doped with $ZrO_2$ nanoparticles and improve visible light driving photocatalytic activity were observed. Non-metal doping is thought to be more viable strategy to reduce the band gap and enhance the visible light driven photocatalytic activity of $ZrO_2$ (Anandan *et al.,* 2020). For instance, Agorku *et al.* (2015) investigated photocatalytic activity of N, S co-doped $ZrO_2$ for the degradation of indigo carmine and observed degradation efficiency of co-doped N-S $ZrO_2$and pure $ZrO_2$ to be (98%) and (66%) within 71 minutes.

### 2.6.3 Co-doping of zirconia with metals/non-metals

Co-doping of $ZrO_2$ simultaneously by incorporating two metallic or non-metallic elements as dopants is expected to bring about a significant reduction in band gap and enhancement of its surface area and photocatalytic properties of $ZrO_2$ (Vattikuti *et al.,* 2019). In this method, two non-metallic or metallic elements is simultaneously added dropwise to an already synthesized zirconium oxide nanoparticle. Main-while, co-

doping of metallic oxide show controversial photocatalytic properties in thin film and bulk sample. Co-doping of zirconium oxide nanoparticles with non-metallic elements has produced a more viable light driven photocatalytic property under excitation by UV light.

For instance Tamm *et al.* (2017) synthesized Fe, Co co-doped $ZrO_2$ nanoparticles using solvothermal method and it was found that Fe and Co exhibited electromagnetic behaviour at low temperature. Also, the phase property of the nanoparticles changed from tetragonal to monoclinic due to addition of the two metals. Moreso, Anku *et al.* (2016) co-doped $ZrO_2$ with cobalt and carbon via chemical method and applied the nanocatalyst for the degradation of indigo carmin and eosin Y dyes. The authors reported increased in the percentage degradation from 21 % to 88.8% after 180 minutes attributable to the introduction of the cobalt and carbon dopant onto the crystal lattice of $ZrO_2$ nanoparticles.

### 2.6.4 Choice of carbon as dopant

Doping of $ZrO_2$ with non-metals for instance carbon has been found to be one of the methods of effective band gap reduction to enhance photocatalysis under UV or visible region (Kucio *et al.*, 2020). Carbon is p-block elements with electronic configuration of $1s^2\ 2s^2\ 2p^2$ and has the tendencies to dope with metal oxides to reduce the band gap and increase the number of active sites. The band gap reduction takes place as a result of the effective mixing of the 2p state of $ZrO_2$ with the 2p state of carbon (Melchor-Lagar *et al.*, 2020). Carbon doping favoured the formation of oxygen vacancies in $ZrO_2$, which results in the modest variation of the band gap and induction of several localized

occupied state in the gap. Addition of carbon often lead to red shift of the absorption edge of $ZrO_2$ towards visible region

### 2.6.5 Choice of sulphur as dopant

Doping of $ZrO_2$ with non metals for instance sulphur has been found to be one of the methods of effective band gap reduction to enhance photocatalysis under UV or visible region (Kucio *et al.*, 2020). The decrease in band gap of $ZrO_2$ upon doping with sulphur may be explained based on the presence of an impurity state of sulphur 3p on the up spin of the $ZrO_2$ valence band (Mishra *et al.*, 2021). p-block elements have the tendencies to dope with metal oxides to reduce their band gap. The band gap reduction takes place as a result of the mixing of the 2p state of $ZrO_2$ with the 3p state of sulphur (Melchor-Lagar *et al.*, 2020). Studies have shown significant reduction of band gap energy of semiconductor metal oxides and strong absorption in the visible lightwere observed when optimal amount of sulphur was added to metal oxide of interest. The shift in the absorption spectra caused S to substitute or displace oxygen and formed sulphur-doped metal oxide. However, the integration mechanism of sulphur onto the lattice layer of metal oxide, from a structural point of view, is still under debate. This is because sulphur predominantly in the form of sulphate ion could be adsorbed at the surface of metal oxide nanoparticles, or entrapped within the lattice layer of metal oxide.

## 2.7 Synthesis of Zirconium Oxide Nanoparticles

Zirconium oxide nanoparticles can be synthesized using different methods such as hydrothermal method, spray pyrolysis, sputtering, microwave-assisted reduction, photodeposition, electron deposition, chemical vapour deposition, solvothermal, thermal

deposition, green synthesis and sol-gel method (Renuka *et al.*, 2021). Others, apart from biosynthesis have complex procedures, longer reaction time, use of toxic chemicals. On the contrary, the green synthesis method seems to be the most viable approach of producing nanoparticles because it is simple, operates at a very low temperature, requires simple and less complicated procedure compared to other physical and chemical methods. Some of these methods are explained as follows.

### 2.7.1 Hydrothermal method

This method involves the growth of nanomaterials at high temperature (500°C) and pressure of 1500 atm (Gurushantha *et al.*, 2017). The synthesized nanomaterials are practically insoluble under normal conditions. The parameters that influence the size and shapes of the nanoparticle include initial pH of the medium, reaction time, temperature of the synthesis and the pressure in the system. In hydrothermal synthesis, the reacting mixture depends on the process kinetic of the resulting products put in a sealed autoclave. This in turn determines the overall performance of the nanomaterial that can withstand high temperature and pressure for a long time (Iqbal *et al.*, 2020). Nanoparticles are normally produced either by means of high temperature hydrolysis reaction of various compounds in an autoclave or hydrothermal treatment of reaction products at room temperature. The hydrothermal approach is based on the sharp increase in the rate of crystallization formation of several amorphous phases under the hydrothermal conditions. The autoclave is loaded with aqueous solution of precursor salts in the while the suspension of products derived from solutions react under normal conditions. Advantages of the hydrothermal method include the ability to synthesis

crystals which are unstable near the melting point. Disadvantages include high cost of equipment and inability to monitor the crystal growth formation. For instance, Munawar *et al.* (2020) utilized hydrothermal method to prepare $ZrO_2$ nanoparticles and found that crystalline particle size and phase structured $ZrO_2$ nanoparticleswas31nm and face cubic centre phase respectively.

### 2.7.2 Solvothermal method

Solvothermal methods combined the benefit of both the hydrothermal and sol-gel methods (Sartale and Gophane, 2019). Thus, solvothermal synthesis allow for the precise particle size control over the shape distribution and crystallinity of metal oxide nanoparticles (Kucio *et al.*, 2020). These characteristics can be altered by changing certain experimental parameters namely reaction temperature, reaction time, solvent type, surfactant type and precursor type (Rozana *et al.*, 2017). Solvothermal process involves the use of solvent under moderate to high pressure (typically between 1atm and 10,000 atm) and temperature (typically between 100°C and 1000°C) which facilitates the interaction of precursors during synthesis (Mondal *et al.*, 2017). Solvothermal synthesis has been used in the laboratory to produced nanoparticles such as titanium dioxide, graphene, $ZrO_2$, carbon nanotube and other materials (Yang *et al.*, 2019). Lin *et al.* (2018) employed solvothermal synthesis method to prepare $ZrO_2$ nanostructure using zirconium carbonate via the variation of calcinations temperature from 300°C to 500°C and the XRD analysis revealed a monoclinic crystalline phase with average crystallite size of 49 nm.

### 2.7.3 Thermal deposition

Thermal deposition basically involves two processes which are evaporation of a hot source material followed by the condensation of the vapour on the substrate (Pei *et al.,* 2017). This method resembles the familiar process where liquid water appears on the lid of a boiling pot, under different, gaseous environment and heat source (Mondal *et al.,* 2017). Evaporation take place in a vacuum and the vapours other than source materials are almost entirely removed before the process begins (Zhang *et al.,* 2019). In high vacuum, evaporated particles can travel directly to the deposition target without colliding with the background gas (Ghosh *et al.,* 2019). The advantages of thermal deposition includes short time deposition period, easy deposition of thin film, the ability to form on a non-uniform surface and ability to control the thickness of the film (Pei *et al.,* 2017). Evaporated atoms that collide with foreign particles may react with metals in the presence of oxygen to form metal oxides and subsequently deposited on the substrate. For instance Jimenez *et al,* (2016) studied the enhanced thermal properties of $ZrO_2$ nanoparticles and chitosan based flame retardant coating by varying the calcination temperatures from 300°C to 500°C. The XRD spectra revealed formation of tetragonal phased zirconium oxide nanoparticles with a crystallite size of 85 nm.

### 2.7.4 Sol gel method

This process involves conversion metal salts into a colloidal solution (Sol), which further act as the precursor for the intergrated network (or gel) of either discrete particles or network polymers (Pei *et al.,* 2017). A typical precursor mostly used in sol-gel method is metal alkoxides, metal halides among others (Sigwadi *et al.,* 2017). Sol-gel is considered as one of the most successful techniques for preparing nano-sized metallic oxide material with excellent photocatalytic potentials (Choi *et al*., 2017). Sol-gel process excellently involves two basic chemical reactions namely hydrolysis and

condensation (Zhang *et al.,* 2017). During hydrolysis the metal alkoxides, M-OR is broken down by water molecules while one or more of thealkoxide groups are replaced by hydroxide group. During condensation water and alcohol molecules are eliminated through the following different mechanism such as alkoxolation, oxolation, polycondensation and eventually oxygen bridges are formed in between the metal atoms (Wahba *et al.,* 2020). For instance, Bashir *et al.* (2018) employed sol-gel method to prepare $ZrO_2$ nanoparticles with a micro organic precursor via variation of dopant concentration and revealed a crystallite particle size of 53 nm with a monoclinic phase structure.

### 2.7.5 Green synthesis method

Green synthesis method seems to be the most suitable method of producing nanoparticles due to its simplicity and operate at a very low temperature without generation of byproducts compared to other methods (Yadav *et al.,* 2020). Nanoparticles can be synthesized using physical, chemical, biological and hybrid techniques (Mondal *et al.,* 2017). However, these methods such as physical and chemical methods are bound with various limitations such as high cost of reagents, generation of hazardous toxic chemical, complex preparation procedure among others (Jabir *et al.,* 2018). This has led researchers to seek for safe, eco-friendly alternative approaches in the synthesis of nanoparticles (Kucio *et al.,* 2020). Studies have shown that plants have the potential to reduce metal ions both on their surface and in various organs and tissues to zero valence state (Mondal *et al.,* 2017). The reduction of metals

ions into nanoparticles is due to the presence of plants phytochemical components such as sugars, terpenoids, polyphenols, tannins, alkaloids and protein. These constituents played an important role as both reducing, stabilizing and capping agent (Kaviya *et al.*, 2020). Generally, different workers have employed either top down process and bottom up process to produce $ZrO_2$ nanoparticles. For instance, top-down process involves the breaking down bulk material into nanoparticles using various techniques such as grinding and milling (Shinde *et al.*, 2018). While in the case of bottom-up process, atoms are self-assemble to create new nuclei which further grow into a particle at nanoscale (Taufik *et al.*, 2018). For instance Ali *et al.*, (2016) employed green method using *Allium sativum* and zirconium chloride via variation of calcinations time. The XRD pattern shows the formation of cubic phase with crystallite size of 20 nm.

### 2.8 Application of Zirconium Oxide Nanoparticles

The main use of $ZrO_2$ is in production of ceramics, such as in dentistry (Wang *et al.*, 2020). Other uses include protective coating on particles of titanium dioxide pigments, as a refractory material in insulation, abrasive and enamels (Iqbal *et al.*, 2020). Stabilized $ZrO_2$ is used in oxygen sensors and fuel cell membrane because it has the ability to allow oxygen ion to move freely through the crystal structure at high temperature (Balagangadharan *et al.*, 2018). $ZrO_2$ nanoparticles has high ionic conductivity and low electronic conductivity, this makes it one of the most useful electroceramics (Bharathi *et al.*, 2020).

Transformation toughened $ZrO_2$ is used to make ceramic knives. Because of the hardness, ceramic-edged cutlery stays sharp longer than steel edged products (Feng *et*

*al.*, 2019). Due to its infusibility and brilliant luminosity when incandescent, it was used as an ingredient of sticks for limelight (Gurushantha *et al.*, 2017). $ZrO_2$ is also a potential high-k dielectric material with potential applications as an insulator in transistors.

$ZrO_2$ is also employed in the deposition of optical coatings; it is a high-index material usable from the near-UV to the mid-IR, due to its low absorption in this spectral region. In such applications, it is typically deposited by PVD. $ZrO_2$ nanoparticles are used as catalyst to eliminate pollution caused by industrial wastewater and in bioengeneering in the production of prosthesis and implants as well as carrier medicine.

## 2.9 Local Dyeing Wastewater

Local dyeing wastewater are coloured and toxic wastewater generated from indigenous dyeing industries, in Nigeria the local dyeing textile industries are increasing as textile industries continue to fold up across the country due to poor managerial skills and government policies (Gurushantha *et al.*, 2017). Also the increase in demand for local dyeing fabric has resulted into the increase in local dyeing industries and hence an increase in the amount of local dyeing wastewater released into the water bodies. Local dyeing wastewater contain organic dyes and inorganic constituents that constitute environmental pollution upon release into the environment (Aghabeygi and Khademi-Shamami, 2018). Dyes are coloured substance that chemically bonds to the substrate to which they are being applied (Aneyo *et al.*, 2016). This distinguishes dyes from pigments which do not chemically bind to the material they color. The dye is generally applied in an aqueous solution, and may require a mordant to improve the

fastness of the dye on the fiber. The majority of natural dyes are derived from plant sources: roots, berries, bark, leaves, wood, fungi and lichens.

## 2.10 Environmental Effects of Local Dyeing Wastewater

The discharge of large amount of untreated dyeing wastewater into the water bodies is creating pollution problems and thus requires immediate actions (Aghabeygi and Khademi-Shamami, 2018). Specifically, local dyeing industry is one of the oldest and most complex industries because it consumes and generate high quantity of wastewater (Bharathi *et al.,* 2020). The dye wastewater when discharged into our water bodies significantly compromise its aesthetic quality, increase biochemical and chemical oxygen demand (BOD and COD), impair photosynthesis, inhibit plant growth, enter the food chain, provide recalcitrance and bioaccumulation, and may promote toxicity in aquatic environments by undergoing toxic reactions (Danilenko *et al.,* 2018). Local dyeing wastewater also cause several health problems to human ranging from skin irritation, diarrhea, vomiting, cancer etc depending on the dose and length of exposure (Aghabeygi and Khademi-Shamami, 2018). These organic pollutants such as azo dyes, nitro dye, acid or base type are non biodegradable and may persist for long in the environment.

## 2.11 Classification of Organic Dyes

Dyes can be classified as follows;

### 2.11.1 Acid dyes

Acid dyes are water-soluble anionic dyes, they contain one or more sulphonic acid substituents and acidic groups. An example is Acid Yellow 36.

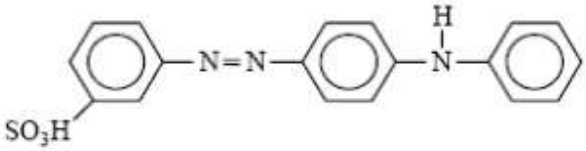


**Figure 2.4: Acid Yellow 36**

Acid dyes are water-soluble anionic dyes which can be used on fibers such as silk, wool, nylon and modified acrylic fibers using neutral to acid dye baths. Acid dyes are not substantive to cellulosic fibers. Most synthetic food colours are in this category (Gurushantha *et al.*, 2017).

### 2.11.2 Basic or cationic dye

This group of dyes was the first synthetic dyes to be taken from coal-tar derivatives. As textile dyes, they have been largely replaced but are still being used in discharge printing, and for preparing leather, paper, wood, and straw (Aghabeygi and Khademi-Shamami, 2018). More recently they have been successfully used with some readymade fibers, especially the acrylics (Aneyo *et al.*, 2016). Basic dyes were used originally to colour wool, silk, linen, hemp among others, without the use of a mordant, or using agent. With a mordant like tannic acid they were used on cotton and rayon. Basic dyes give brilliant colours with exceptional fastness to acrylic fibers. They can also be used on basic dyeable variants of nylon and polyester (Gurushantha *et al.*, 2017). For instance Basic Brown 1.

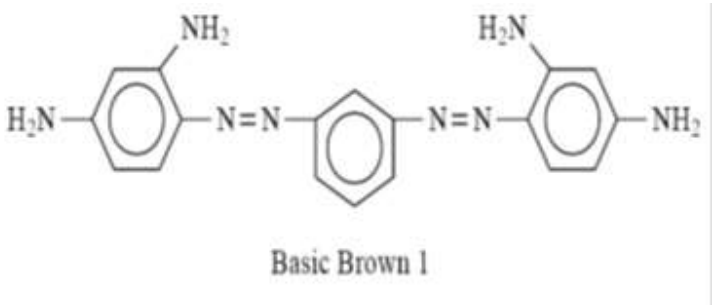


**Figure 2.5: Basic Brown 1**

### 2.11.3 Direct dye

Direct dyes are the dyes that can be applied directly to the fabrics from an aqueous solution. These are most useful for fabrics that can form hydrogen bonds with the dyeing fabrics (Aghabeygi and Khademi-Shamami, 2018). The direct dyes are mainly the basic widely used as mordant or a binder in dyeing cotton. The colours are not as brilliant as those in the basic dyes but they have better fastness to light and washing, and such fastness can be measurably improved by after treatments. Direct dyes can be used on cotton, linen, rayon, wool, silk and nylon. These dyes usually have azo linkage –N=N- and high molecular weight. They are water soluble because of sulphonic acid groups (Eljaaly *et al.*, 2020).

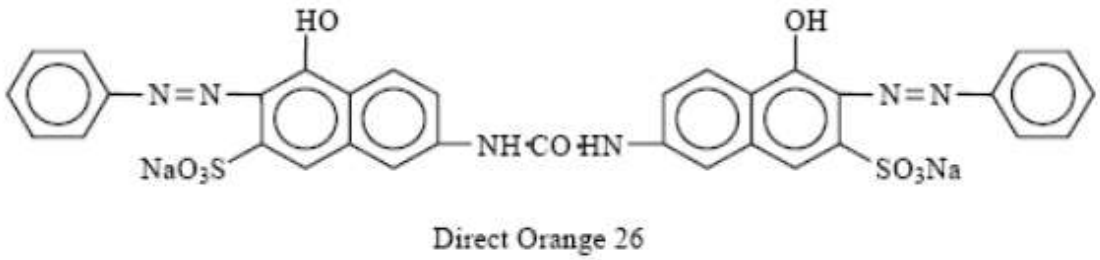


**Figure 2.6: Direct Orange 26**

### 2.11.4 Azoic dye

Azo dyes contain at least one azo group (-N=N-) attached to one or often two aromatic rings. These dyes are used primarily for bright red shades in dyeing and printing since

most other classes of fast dyes lacks good red dyes and absorbs in the UV-visible region of (300nm-400nm) (Bharathi *et al.*, 2020). Azoic dyes are actually manufactured in the fabric by applying one half of the dye while the other half is then put on and they combine to form the finished colour. Unless they are carefully applied and well washed, they have poor fastness to rubbing or crocking (Eljaaly *et al.*, 2020). The production of bluish red azoic dye from the following two components is shown as follows.

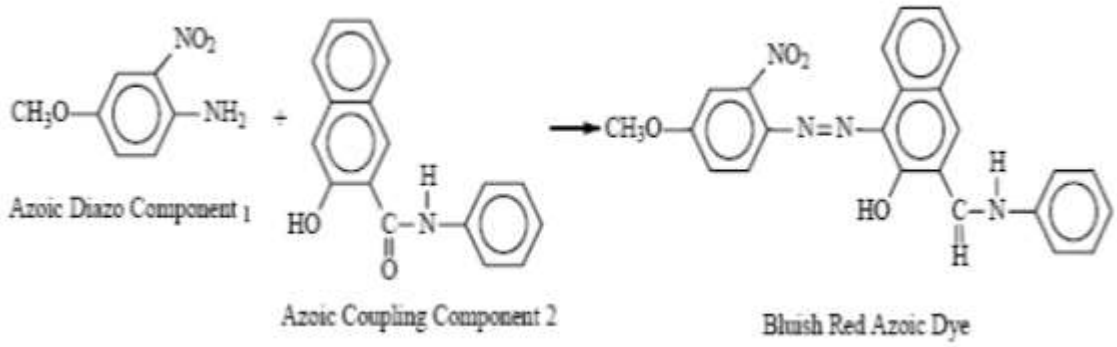


**Figure 2.7: The production of bluish red azoic dye**

### 2.11.5 Nitro dye

Nitro dyes are polynitro derivatives of phenol containing at least one nitro group ortho or para to the hydroxyl group. It is used to dye wool and consist of two or more aromatic rings namely (benzene and naphthalene) (Ossai *et al.*, 2018).

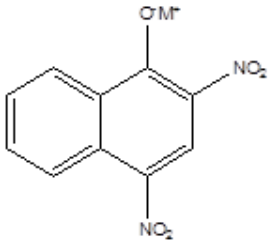


**Figure 2.8: Maritus Yellow**

### 2.11.6 Vat dye

The vat dyes are insoluble complex polycyclic molecules based on the quinone structure . Vat dyes are made from indigo, anthraquinone and carbazole. They are successfully used on cotton, linen, rayon, wool, silk, and sometimes nylon. Vat dyes are also used in the continuous piece of dyeing process sometimes called the pigment application process. The dyeing produced in this way have high wash and light fastness (Danilenko *et al.,* 2018).An example of a vat dye is Vat Blue 4.

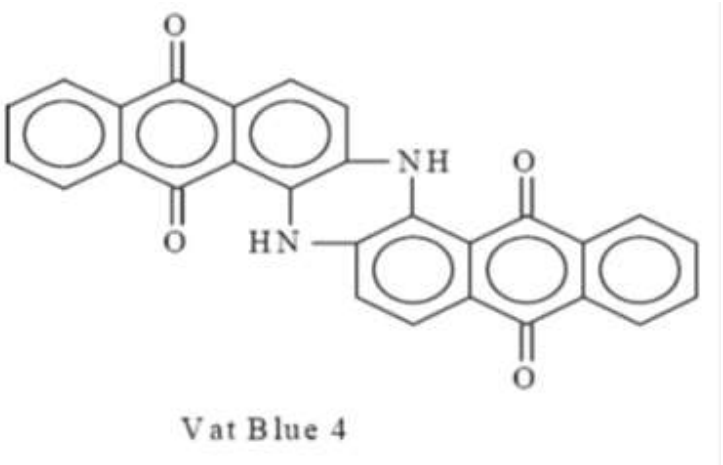


**Figure 2.9: Vat Blue 4**

### 2.11.7 Mordant dye

Mordant dye do not dye the fabric directly but require a binding agent known as mordant. The mordant acts as a binding agent between the fibre and the dye (Kianfar *et al.,* 2021). Some dyes combine with metal salts to form insoluble coloured complexes (lakes). These materials are usually used for the dyeing of cotton, wool or other protein fiber. The metallic precipitate is formed in the fiber producing very fast colours that are highly resistant to both light and washing (Gurushantha *et al.,* 2017).

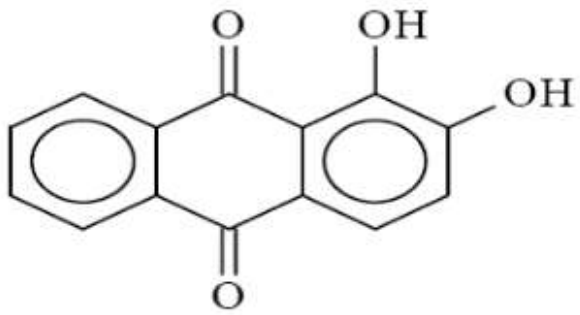


Mordant Red 11

**Figure 2.10: Mordant Red 11**

### 2.11.8 Reactive dye

These dyes react with the cellulosic fiber to form a covalent bond and produces dyed fiber with extremely high wash fastness properties (Mishra *et al.,* 2021). These are the dyeing of fabrics which contain a reactive group which combines directly with the hydroxyl or the amino group of the fibre. Because of the chemical reaction the colour is fast and has a very long life and can be used to dye cotton, wool and silk. There are various types of reactive dyes used in dyeing industry for instance reactive blue 5 (Mondal *et al.,* 2017).

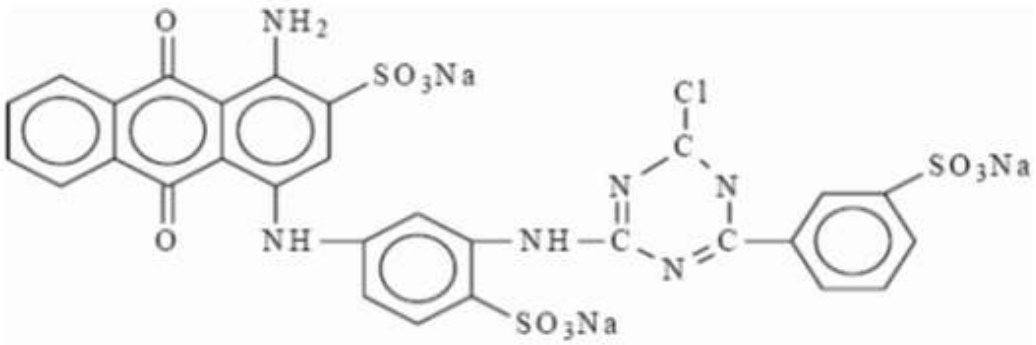


Reactive Blue 5

**Figure 2.11: Reactive Blue 5**

### 2.12 *Plumeria Acuminata*

*Plumeria* is a genus of flowering plants in the family Apocynaceae (Kaviya *et al.*, 2020). Most species are deciduous shrubs or small trees. The species variously are endemic to Mexico, Central America and the Caribbean, and as far south as Brazil and north as Florida, but are grown as cosmopolitan ornamentals in warm regions (Shinde *et al.*, 2018). Common names for plants in the genus vary widely according to region, variety, and whim, but frangipani or variations on that theme are the most common. *Plumeria* is also used as a common name, especially in horticultural circles

**Plate 1:Image of *Plumeria acuminata* plant** (Kaviya *et al.*, 2020).

The scientific classification are as follows.

| | |
|---|---|
| Kingdom | Plantae |
| Order | Gentianales |
| Family | Apocynaceae |
| Subtribe | Plumeriinae |
| Genus | Plumeria |

Studies have shown that different part of *Plumeria acuminata*are rich in phytochemical constituents such as alkaloids, tannins, phenols, flavinoids and others (Aghabeygi and Khademi-Shamami, 2018). These chemical components can perform the same function as toxic commercial reducing agents like $NaBH_4$, $LiAlH_4$, sodium citrate and others. Thus, the plant materials are readily available and affordable at little or no cost and can serve as close substitute to commercial reducing agent thereby contributing to environmental sustainability (Kaviya *et al.*, 2020).

## 2.13 Analytical Tools for Characterization of Zirconium Oxide Nanoparticles

### 2.13.1 High resolution scanning electron microscopy

High resolution scanning electron microscope (HRSEM) is a type of electron microscope that produces images of a sample via scanning the surface with a focused beam of electrons. The interaction of electrons with atoms in the sample, produced various signals containing information about the surface topography and composition of the sample (Zhang *et al.*, 2019). The electron beam is scanned in a raster scan pattern, and the position of the beam is combined with the detected signal to produce an image. HRSEM can achieve resolution better than 1 nanometer (Yaghoubi *et al.*, 2020).

The most common HRSEM mode is the detection of secondary electrons emitted by atoms excited by the electron beam. The number of secondary electrons that can be detected depends, among other things, on specimen topography. By scanning the sample and collecting the secondary electrons that are emitted using a special detector, an image displaying the topography of the surface is created (Yousefi *et al.*, 2018).

Characteristic X-rays are emitted when the electron beam removes an inner shell electron from the sample, causing a higher-energy electron to fill the shell and release

energy. The energy or wavelength of these characteristic X-rays can be measured by Energy-dispersive X-ray spectroscopy or Wavelength-dispersive X-ray spectroscopy and used to identify and measure the abundance of elements in the sample and map their distribution (Sigwadi *et al.,* 2017).

### 2.13.2 High resolution transmission electron microscopy

High-resolution transmission electron microscopy (HRTEM) is an imaging mode of specialized transmission electron microscopes (TEMs) that allows for direct imaging of the atomic structure of the sample (Sigwadi *et al.,* 2017). While HRTEM is often also used to refer to high resolution scanning TEM (STEM, mostly in high angle annular dark field mode), this describes mainly the imaging of an object by recording the 2D spatial wave amplitude distribution in the image plane, in analogy to a "classic" light microscope (Rozana *et al.,* 2017). The technique is also often referred to as phase contrast TEM. At present, the highest point resolution realized in phase contrast TEM is around 0.5 angstroms (0.050 nm) (Reddy *et al.,* 2020). At these small scales, individual atoms of a crystal and its defects can be resolved.

One of the difficulties with HRTEM is that image formation relies on phase contrast (Sigwadi *et al.,* 2017). In phase-contrast imaging, contrast is not necessarily intuitively interpretable, as the image is influenced by aberrations of the imaging lenses in the microscope. The latter can be estimated from the so-called Thon ring pattern appearing in the Fourier transform modulus of an image of a thin amorphous film (Gautam *et al.,* 2016).

### 2.13.3 Energy dispersive x-ray spectrometry

EDS makes use of the X-ray spectrum emitted by a solid sample bombarded with a focused beam of electrons to obtain a localized chemical compositions of the sample. All elements from atomic number 4 (Be) to 92 (U) can be detected in principle, though not all instruments are equipped for 'light' elements (Z < 10). Qualitative analysis involves the identification of the lines in the spectrum and is fairly straightforward owing to the simplicity of X-ray spectra (Gautam *et al.,* 2016). Quantitative analysis (determination of the concentrations of the elements present) entails measuring line intensities for each element in the sample and for the same elements in calibration with standard of known composition. By scanning the beam in a television-like raster and displaying the intensity of a selected X-ray line, element distribution images or 'maps' can be produced. The scanning electron microscope (SEM), which is closely related to the electron probe, is designed primarily for producing electron images, but can also be used for element mapping, and even point analysis (Sigwadi *et al.,* 2017).

### 2.13.4 Selected area electron diffraction

Selected Area Electron Diffraction is a crystallographic experimental technique that can be performed inside a transmission electron microscope (TEM). In a TEM, a thin crystalline specimen is subjected to a parallel beam of high-energy electrons. As TEM specimens are typically ~100 nm thick, and the electrons typically have an energy of 100–400 kiloelectron volts pass through the sample easily. In this case, electrons are treated as wave-like, rather than particle-like (Dong *et al.,* 2018). Because the wavelength of high-energy electrons is a few thousandths of a nanometer and the spacing between atoms in a solid is about a hundred times larger, the atoms act as a diffraction grating to the electrons, which are diffracted (Elshereksi *et al.,* 2017). That is, some fractions will be scattered to particular angles, determined by the crystal

structure of the sample, while others continue to pass through the sample without deflection. As a result, the image on the screen of the TEM are often series of spots—the selected area diffraction pattern, (SADP) each spot corresponding to a satisfied diffraction condition of the sample's crystal structure. If the sample is tilted, the same crystal will stay under illumination, but different diffraction conditions will be activated, and different diffraction spots will appear or disappear (Huang *et al.*, 2018).

### 2.13.5 Brunauer emmett teller

Brunauer-Emmett-Teller (BET) technique aims to explain the physical adsorption of gas molecules on a solid surface and serves as the basis for an important analytical technique for the measurement of the specific surface area of materials (Elshereksi *et al.*, 2017).

The BET theory applies to system of multilayer adsorption and usually utilizes probing gases that do not chemically react with material surfaces as adsorbates to quantify specific surface area, pore size and pore diameter (Ismael *et al.*, 2019). Nitrogen is the most commonly employed gaseous adsorbate used for surface probing by BET methods for this reason, standard BET analysis is most often conducted at the boiling temperature of nitrogen (77K) (Zang *et al.*, 2020). Further probing adsorbates such as argon, carbon dioxide and water are utilized, albeit with lower frequency, allowing the measurement of surface area at different temperature and measurement scales (Zhang *et al.*, 2017).

### 2.13.6 XRD

XRD analysis is based on constructive interference of monochromatic X-rays with crystalline sample: The X-rays are generated by a cathode ray tube, filtered to produce

monochromatic radiation, collimated to concentrate, and directed toward the sample. The interaction of the incident rays with the sample produce constructive interference (and a diffracted ray) when conditions satisfy Bragg's Law ($n\lambda=2d \sin \theta$). This law relates the wavelength of electromagnetic radiation to the diffraction angle and the lattice spacing in a crystalline sample. The characteristic x-ray diffraction pattern generated in a typical XRD analysis provides a unique "fingerprint" of the crystals present in the sample. When properly interpreted, by comparison with standard reference patterns and measurements, this fingerprint allows identification of the crystalline form (Jaramillo-Paez *et al.,* 2017).

### 2.13.7 UV-visible spectroscopy

UV-visible absorbance spectroscopy is one of the most known analytical techniques for the determination of the absorption bands of the synthesized nanoparticles (Dong *et al.,* 2018). This technique employ light of different wavelength which is absorb by the sample and the incident and transmitted light intensities are measured and interpreted using Beer Lambert law relationship A=Kbc, where K is a constant of proportionality, called absorbtivity (2.11). C is the concentration ($mol/dm^3$) or the absorbing species, b is the path length (cm).

Some of the approaches used to prepare $ZrO_2$ nanoparticles and identified research gaps are provided in Table 2.1.

## 2.14 Kinetic Models

### 2.14.1 Pseudo first order

When a process is 2nd order overall but first order with regard to two reactants, it is called pseudo first order kinetics. When A and B are generic reactants, the initial rate is determined by both A and B, and as the reaction progresses, both A and B's concentrations change, affecting the rate. To assess whether the reaction process is physical or chemical, a pseudo first order kinetic model is used (Noviyanti *et al*., 2021). Equation 2.6 is used to express it.

$$\boldsymbol{In\left(\frac{Co}{Ct}\right) = -kt} \qquad (2.6)$$

Where $C_o$= initial concentration $C_t$= final concentration

k= rate constant t= time

### 2.14.2 Zero order

A zero-order reaction, unlike the other orders of reaction, has a rate that is independent of the reactant concentration. As a result, increasing or reducing the concentration of the reactive species has no effect on the rate of the reaction. When a material that is required for the reaction to proceed, such as a surface or a catalyst, is saturated by the reactants, zero-order reactions occur. A zero-order reaction's rate law is rate = k, where k is the rate constant. The rate constant k for a zero-order reaction will have units of concentration/time, such as M/s. (Encinar *et al*., 2021) . Zero order kinetic model is represented by equation 2.7.

$$\boldsymbol{Co - Ct = kt} \qquad (2.7)$$

Where $C_o$= initial concentration $C_t$= final concentration

k= rate constant t= time

### 2.14.3 Parabolic model

A parabola is a curve in which any two points are at the same distance from each other: a fixed point (the focus), and a fixed straight line (the directrix ). The directrix is not the center of attention. The locus of points in that plane that are equidistant from both the directrix and the focus is known as the parabola. A parabola is also known as a conic section, which is formed when a right circular conical surface meets a plane parallel to another plane that is tangential to the conical surface. (Shooto *et al*., 2016). Parabolic model is represented by equation 2.8

$$\left(\frac{1-Ct/Co}{t}\right) = kt^{1/2} + \propto \qquad (2.8)$$

Where $C_o$= initial concentration $C_t$= final concentration

k= rate constant t= time

α= kinetic order of parabolic diffusion model

### 2.14.4 Modified freudlich model

The Freundlich equation, also known as the Freundlich adsorption isotherm, is an empirical relationship that exists between the amount of gas adsorbed onto a solid surface and the gas pressure. The concentration of a solute adsorbed onto the surface of a solid and the concentration of the solute in the liquid phase have the same relationship. (Augustus *et al*., 2017). Freundlich adsorption isotherm or Freundlich adsorption equation is the name given to this equation. In the case where adsorption behavior can be well modeled by isotherms with a theoretical basis, as demonstrated in equation 2.9, this relationship is totally empirical.

$$\frac{Co-Ct}{Co} = kt^{b} \qquad (2.9)$$

Where $C_o$= initial concentration $C_t$= final concentration

k= rate constant t= time

b= Freudlich constant

**Table 2.1: Synthesis of $ZrO_2$ nanoparticles using different methods and conditions is introduced in table 2.1**

| Author/Year | Title | Research findings | Research gap |
|---|---|---|---|
| Yungjun *et al.* (2010) | Synthesis, characterization and electrochemical properties of mesoporous $ZrO_2$ materials prepared by self assembly sol-gel method with tween 20 as a template. | Tween 20 proved to suitable structure directing agent in the formation of mesoporous $ZrO_2$ nanoparticles and their derived film with high BET surface area ($152m^2/g$) and pore volume decreased particle size and good structural integrity. | The authors did not report the optical and photocatalytic properties of mesoporous $ZrO_2$ nanoparticles. |
| Eshed *et al.* (2011) | $ZrO_2$ nanoparticles prepared by the reduction of zirconium oxide using RAPET method | $ZrO_2$ nanoparticles have two crystalline phases, the monoclinic and tetragonal phase with the monoclinic phase been the major component of the solid mix | The particle size was not evaluated from the XRD spectra. |
| Dharmaraj. (2012) | Synthesis and characterization of $ZrO_2$ nanofibre by electrospining | The observed X-ray diffraction patterns (XRD) of the fibres showed the presence of both tetragonal and monoclinic phase after calicination at $300^0C$ and $700^0C$. However, the samples obtained after calcination at $1000^0C$ showed the presence of only | The photocatalytic activity of $ZrO_2$ nanoparticles was not investigated. |

| | | | |
|---|---|---|---|
| | | monoclinic phase in XRD patterns. | |
| Tharani. (2013) | Green synthesis of $ZrO_2$ nanoparticles using *Alcalypha indica* leaf extract | The preparation of $ZrO_2$ nanoparticles using *Alcalyphaindica*was ecofriendly andeffectivesubtitute for the large scale production of $ZrO_2$ nanoparticles using physical and chemical methods. The nanoparticle produced have a monoclinic faced structure with particle size of 58 nm. | The optical and textural properties of $ZrO_2$ was not determined . |
| Muthuchudarkodi. (2014) | Preparation and electrochemical characterization of manganese dioxide doped zirconium oxide nanorod. | SEM and TEM studies show a uniform rod-like morphology in the case of mixed oxide. CV studies revealed that the mixed oxide exhibited good adherent and electrochemical activity on GC and thus it was found to be corrosive protection agent for paints formulation. The capacitance of chemically synthesized mixed oxide was suggested that, the material can be used as an electronic material. | Band gap of manganese dioxide doped $ZrO_2$ was not determined and the photocatalytic behaviour of the zirconium oxide base material was not examined. The author employed chemical method of preparation of $ZrO_2$ |

| | | | |
|---|---|---|---|
| | | | nanoparticles. |
| Arreche *et al.* (2015) | Synthesis and characterization of $ZrO_2$ for use as antimicrobial activity in paints | The solids ecologically synthesized are promising for use in paints additives solids. | Proper optimization of the synthesis parameters including doping either with metal or non metals were not done. |
| Stolzenburg *et al.* (2016) | Facial growth of $ZrO_2$ nanoparticles induced by synthesis conditions | $ZrO_2$ grown into either spherical or fractal morphologies. Particles grown during non acqueous synthesis were highly controlled by the chemical reaction. | The evaluation of the fractal growth of $ZrO_2$ nanoparticles was not done and the band gap was not determine. |
| Chen *et al*, (2017) | Synthesis of nano $ZrO_2$ and its application in dentistry | $ZrO_2$ can be employed in dental ceramics, implants, radiopacifying agents, denture basement and tissue engineering. Nearly all the showed works have displayed the characteristics improvement following adding nano-$ZrO_2$. Besides, nano-$ZrO_2$ exhibits the superior biocompatibility. | Greater depth investigation about the interaction between nano-$ZrO_2$ and stem cells need to be explored |

| | | | |
|---|---|---|---|
| Rajendran *et al.* (2018) | Characterization and toxicology examination of $ZrO_2$ nanoparticles on the embryonic developement of zebrafish | The zebrafish was reliable and suitable model for evaluating potentialnanotoxicity induced by $ZrO_2$ nanoparticles The study demonstrated that chemically synthesized $ZrO_2$ nanoparticles caused developmental embryonic toxicity | Bio-safety evaluations of usage of $ZrO_2$ nanoparticles and their molecular mechanisms were not elucidated. |
| Hu *et al.* (2019) | Preparation and characterization of high surface area $ZrO_2$ nanoparticle for fuel cell application | The hydrothermal method was found to be the suitable method to synthesise a high surface area $ZrO_2$, as confirmed by BET results which reveal a high specific surface area of 543 $m^2/g$ and pore volume of 0.5 $cm^3/g$. | The crystallite size of the prepared nanomaterials was not calculated |
| Mahtabiam *et al.* (2020) | Synthesis and characterization of hierarchial mesoporous-macroporous $TiO_2$-$ZrO_2$ nanocomposite scaffolds for cancellous bone tissue. | The study showed that scaffold with a lower amount of $ZrO_2$ had less structural defects. This scaffold has pore size, pore wall size, and mesoporous in range of 185 µm to 15 µm. | The author did not report the optical and textural properties of the two materials. |

## 2.15 Chapter summary and Research gap

In this chapter, the synthesis, characterization and application of ordinary metals, non-metals doping and co-doping of $ZrO_2$ nanoparticles have been reported. This chapter also contain information on the photocatalytic activity of $ZrO_2$ nanoparticles and mechanism of generation of hydroxyl radicals. Also, different analytical techniques mostly used to characterize $ZrO_2$ based nanomaterial have been reviewed and reported accordingly. Local dyeing wastewater, its composition and environmental impact of untreated dye wastewater have equally been reviewed. However, there is no information on the synthesis and carbon-sulphur co-doped $ZrO_2$ nanoparticle. Also, the photocatalytic/adsorptive behaviour of carbon-sulphur co- doped $ZrO_2$ nanoparticles on local dyeing wastewater containing different kinds of organic dyes in the presence or absence of natural sunlight has not been reported.

# CHAPTER THREE

## 3.0 MATERIALS AND METHODS

### 3.1 Chemicals and Reagents

Table 3.1 shows the list of chemicals/reagents used for this study with their % purities and the names of suppliers, while Table 3.2 is the list of analytical tools/ equipments that were used for this study with their models and locations.

**Table 3.1 List of chemicals/reagents.**

| Chemicals/reagent | %purity | Supplier |
|---|---|---|
| Zirconyl chloride | 99% | Sigma aldrich |
| Buffer solution | 99% | Sigma aldrich |
| Phenophthalein indicator | 99% | Sigma aldrich |
| Hydrogen sulphide | 99% | Sigma aldrich |
| Polyvinylpyrrolidone | 99% | Sigma aldrich |

**Ta ble 3.2 List of Analytical techniques used in this study**

| Analytical equipments | Model | Country of manufacture | Location |
|---|---|---|---|
| HRSEM | Zeiss auriga | Germany | Department of Physics, University of the Western Cape, South Africa |
| HRTEM | Zeiss auriga | Germany | Department of physics University of the Western cape, South Africa |
| XRD | Bruker A&S D8 Cu-K | United State of America | Ithemba laboratory, Cape town, South Africa |
| UV-visible spectrophotometry | Shimadzu UV 1800 | United State of America | Step B, FUT, Minna |
| BET | NOVA 2400e | United State of America | Step B, FUT, Minna |
| pH | Jenway 3010 | United kingdom | Chemistry laboratory, FUT, Minna |

## 3.2 Sampling

### 3.2.1 Sampling of *Plumeria acuminata* leaves

*Plumeria acuminata* leaves were collected within the Federal University of Technology, Bosso, Minna and taken to the chemistry laboratory, federal university of technology, Minna. The leaves were washed thoroughly to remove dirt and sand particles, after which it was allowed to dry at room temperature for two weeks.

### 3.2.2 Sampling of dye wastewater

The sample bottle was washed thoroughly with Nitric acid, rinsed with double distilled water and allow to dry to avoid contamination of the sample. The wastewater was collected in a dark sample bottle from a local dyeing cottage industry in Bosso, Minna, transported to chemistry laboratory federal university of technology, Minna and stored at a temperature of $4^{\circ}C$ for further use.

## 3.3 Sample Pre-treatment

### 3.3.1 Preparation of *Plumeria acuminata* leaves extract

The dry leaves of *Plumeria acuminata* were pounded into powdery form and 50g was washed with distilled water into 1L volumetric flask followed by the addition of distilled water. The mixture was allowed to stand for 24 hours after which the solution was filtered using Whatmann No 1 filter paper to obtain the extract.

### 3.3.2 Preparation of 0.5M solution of zirconyl chloride

A known weight (28.0 g) of zirconyl chloride was weighed into 250 $cm^3$ beaker followed by the addition of 100$cm^3$ distilled deionized water and stirred thoroughly for about 5 min until it dissolved completely in distilled water and the solution was then

transferred into a 1000$cm^3$ volumetric flask. After which, the volumetric flask was made to the 1000$cm^3$ mark with the distilled water to obtain a 0.5 M solution of zirconyl chloride.

### 3.4 Synthesis of zirconium oxide nanoparticles

The green synthesis of $ZrO_2$ nanoparticles can be described as follows; 40 $cm^3$ of 0.5M zirconyl chloride solution was added into 40 $cm^3$ solution of the *Plumeria acuminata*leaves extract in the ratio of 1:1 and stirred at 500rpm on a magnetic stirrer for 30 minutes. After which the pH of the solution was adjusted to the desired pH 6, 9 and 11 with 0.5M NaOH solution. At pH 6, no particles were formed, while at pH of 9 and 11, a light and deep yellow precipitates were formed and allowed to settle for 24 hours and were separated via decantation. The precipitates were washed thoroughly with deionized water repeatedly to remove all impurities after which the precipitates were oven dried at 80$^{\circ}$C for 3 hours. The precipitates were transferred into a furnace and calcined at 500$^{\circ}$C for 2 hours to produce $ZrO_2$ nanoparticles (Deshmukh *et al.*, 2017).

#### 3.4.1 Doping of zirconium oxide nanocomposite with Sulphur

Sulphur doped $ZrO_2$ nanoparticles was prepared using the wet inpregnation method as described. 10 $cm^3$ of 3% hydrogen sulphide was added dropwise to the already prepared $ZrO_2$ nanoparticle obtained in section 3.4 and stirred at 500 rpm for about 2hours. The mixture was centrifuged at 1000 rpm for 15 minutes. The residue was washed with distilled water and again centrifuge at 1000 rpm and the seperated sample was oven dried at 80$^{\circ}$C for 3hours and calcined in the furnace at 550$^{\circ}$C for 2hours (Shinde *et al.*, 2018).

#### 3.4.2 Doping of zirconium oxide nanocomposite with Carbon

Carbon doped $ZrO_2$ nanoparticles was prepared using the wet inpregnation method as described; 10 $cm^3$ of 3% polyvinylpyrolidone solution was added dropwise to the already prepared $ZrO_2$ nanoparticle obtained in section 3.4 and stirred at 500 rpm for about 2hours. The mixture was centrifuged at 1000 rpm for 15 minutes. The residue was washed with distilled water and again centrifuged at 1000 rpm and the separated sample was oven dried at 80°C for 3hours and calcined in the furnace at 550°C for 2hours (Elshereksi *et al.*, 2017).

### 3.4.3 Doping of zirconium oxide nanocomposite with Carbon and sulphur

Carbon-Sulphur co-doped zirconium oxide nanocomposite were prepared following the wet inpregnation method described as follows; 10 $cm^3$ of 3% polyvinylpyrolidone and 3% hydrogen sulphide were simultaneously added dropwise to the already prepared $ZrO_2$ nanocmposite obtained in section 3.4 and stirred at 500 rpm for about 2hours. The mixture was centrifuged at 1000 rpm for 15 minutes. The residue were washed with distilled water and again centrifuged at 1000 rpm and the separated sample was oven dried at 80°C for 3hours and calcined at a temperature of 550°C in a furnace for 2 hours (Dong *et al.*, 2018).

## 3.5 Characterization of Zirconium Oxide Nanocomposite

### 3.5.1 Morphological arrangement and elemental composition analysis

The morphology of the prepared samples was obtained using Zeiss Auriga High Resolution Scanning Electron Microscope (HRSEM) fitted with secondary electron detector and the Energy Dispersive X-ray spectroscopy (EDS). The sample (0.05mg) was first sprinkled on a metal sample holder called a stub using a double sided tape. The sample was then sputtered coated with gold and palladium (ratio 4: 1) to prevent

charging which distort imaging during analysis using a coating machine and thereafter was ready for HRSEM/EDS observation at a voltage range of 10-15 kV. The EDS was done by adjusting the measurement angle to 150°C and applied voltage to 20 KV.

### 3.5.2 Microstructure and crystalline analysis.

High Resolution Transmission Electron Microscopy images model Zeiss Auriga operated at acceleration voltage of 20kV was used to examine the microstructure and particle size. Ethanolic solution (0.5 g in 10 $cm^3$) was used to disolve the powder sample followed by ultrasonication for 30 minutes. Thereafter, mixtuure (10 uL) was measured onto holey carbon grid and exposed to photo light for 3 minutes before being analysed. The sample with the grids was then mounted on a single tilt holder.

### 3.5.3 Absorption band determination by UV-Visible spectroscopy

UV-Visible Spectroscopy in this case, the Shimadzu UV 1800 was used to determine the wavelength of adsorption. The synthesized nanoparticles was dissolved with distilled water (3 $cm^3$) was put in a cuvette and then scanned in the range of 200-800nm at scanning speed rate of 50 nm/minute.

### 3.5.4 Surface area evaluation

The specific surface area of the synthesized nanoparticles and nanocomposite were determined using NOVA 2400e by applying $N_2$ as an absorbate on a micrometer ASAP 2020 chemisorption surface area analyser. Prior to measurement, the samples (8.6 mg) was degassed at 200°C under nitrogen for 3 hours to remove moisture and other

impurities which blocked the pores. The adsorption and desorption curve of the various sample were obtained at -196 °C.

### 3.6 Determination of Physicochemical Parameters of Local Dyeing Wastewater

#### 3.6.1 Identification of different dyes in collected wastewater using UV-visible spectrophotometer

UV-Visible Spectroscopy in this case, the Shimadzu UV 1800 was used to determine the wavelength of absorption of the dye wastewater. 1 $cm^3$ of the wastewater was added into a cuvette followed by the addition of 1 $cm^3$ distilled water and then scanned in the range of 200-800 nm at scanning speed rate of 50 nm/minute.

#### 3.6.2 Determination of TOC

Firstly, 15$cm^3$of the wastewater was measured into 50$cm^3$volumetric flask followed by addition of 3$cm^3$ of 0.5% (v/v) $H_3PO_4$. Then thereafter, the solution pH was adjusted to 2 and maintained under continuous purging of purified $O_2$ for 10 minutes at a flow rate of 150$cm^3$/min. The sample was digested in an autoclave at 115$^{\circ}$C for 2 hours. Distillation of the digested sample was dry by passing through 5g CuO at a flow rate of 2-3$cm^3$/min for 30min. This aided the conversion of the volatile organic carbons while 0.05g $K_2S_2O_8$ was equally added to decompose the non-volatile organic compounds. The TOC value was determined from the amount of converted non-purging bonded

carbon to $CO_2$ measured by non dispersive infrared analyzer, model 8869 (Bailón-García *et al.*, 2017).

### 3.6.3 Determination of COD

About 10$cm^3$of local dyeing wastewater was pipetted in a round bottom flask. 1$cm^3$ mercury sulphate ($HgSO_4$) and 5$cm^3$ potassium dichromate ($K_2Cr_2O_7$) were added and mixed. Thereafter 3$cm^3$ concentrated sulphuric acid ($H_2SO_4$) was added in a controlled manner under continuous stirring and subsequently digested for approximately 150$^0$C for 2hours. About 5 $cm^3$distilled water was added through the condenser to cool it down and the mixture was titrated with standard sulphate while 2-4 drops of ferroin indicator was added as indicator. The amount of $O_2$ required was calculated from the quantity oxidant consumed.

### 3.6.4 Determination of BOD

The wastewater was conditioned to ensure favourable growth condition for bacteria which will include pH adjustment, dilution with appropriate amount of seed bacteria. Initial dissolved oxygen (DO) of 50$cm^3$ of sample was recorded and then incubated for 5 days at 20°C. After 5 days period, the sample was removed and final DO was measured using dissolved oxygen probe . BOD was calculated from the DO depletion and volume of the sample used using equation 3.1.

$BOD_5$= BOD mg/L = [($DO_1$- $DO_5$) - seed correction] x dilution factor (3.1)

Where; $DO_1$=day 1 and $DO_{2=}$ day 2

### 3.6.5 Determination of TDS

Clean porcelain dish was washed and dried in a hot air oven at $180^0$C for 1hour. The empty evaporating dish was weighed in a weighing balance and recorded as (W1).

Approximately 100 $cm^3$ of the wastewater was filtered and about 75$cm^3$of unfiltered wastewater was transferred into the porcelain and the oven was switched on and allowed to reach a temperature of 105˚C. The wastewater was placed in the hot air oven, dried to get constant mass after 2hours, later cooled in a dessicator and then weighed and recorded as($W_2$). The TDS was calculated using equation 3.2

$$TDS=W_2 - W_1 \quad (3.2)$$

Where; $W_2$ = weight of the dry sample + porcelain dish

$W_1$= weight of the dry porcelain dish.

### 3.6.6 Determination of chloride

Approximately (250 $cm^3$) of the wastewater sample was measured into a conical flask and the pH was measured using a pH meter, then few drops of potassium dichromate indicator solution was added. Silver nitrate solution was titrated to pinkish yellow end point and the volume of titrant used was noted and the pH also measured using a pH meter. The chloride ion concentration was calculated using equation 3.3

$$\text{Chloride ion concentration (mg/L)} = (A \times N \times 35.45) \times 1000/V_{sample} \quad (3.3)$$

Where; A = volume of titrant used.

N = normality of $AgNO_3$ (0.0141)

$V_{sample}$= volume of the sample used.

### 3.6.7 Determination of pH

An electrode on the pH meter was dropped into a solution of known pH and the power switch on to take the reading, the pH meter was standardized using the calibration knob. The electrode was cleaned and dip in a buffer solution of pH, 4 and 7 then the reading was noted and calibrated. The electrode was washed again with distilled water and dipped in the solution and the reading of the dial indicates the pH of the solution.

### 3.6.8 Determination of alkalinity

Approximately 50$cm^3$ of wastewater sample was collected and about 3 drops of phenolphthalein indicator was added and then titrated against 0.02N sulphuric acid to a pH of 8.3. The pH at which the indicator changedcolour from pink to colourlesswas noted and the alkalinity of the wastewater was estimated using equation 3.4

Phenophthalein alkalinity= A x N x 50,000/V (3.4)

Where; A= volume of sulphuric acid

N= normality of sulphuric acid

V= volume of wastewater sample used.

## 3.7 Application of Synthesized Zirconium Oxide Nanocomposite to dye Wastewater under Natural Sunlight Irradiation (Photocatalytic experiment)

The photocatalytic experiments of the synthesized undoped, mono-doped and co-doped $ZrO_2$ nanoparticles were evaluated using a 250 $cm^3$ capacity photoreactor with a magnetic stirrer. Natural sunlight was used as irradiation source. 0.5 g of the nanocatalyst ($ZrO_2$ alone) was added to 50 $cm^3$of the local dyeing wastewater. The solution was kept in dark under magnetic stirring of the wastewater effluent for 30

minutes in order to establish the adsorption-desorption process. Thereafter, the mixture in a reactor were exposed to natural sunlight and stirred continuously with stirring speed 500 rpm for 2 hours. Sampling of 5 $cm^3$ of the wastewater was done at regular time intervals (0 minutes, 30 minutes, 60 minutes, 90 minutes, 120 minutes) and filtered using Whatmann No. 1 filter paper. The photocatalytic degradation of the local dyeing wastewater using the nanocatalyst was evaluated by measuring the level COD, BOD , TOC $SO_4^{2-}$, $CO_3^{2-}$, $NO_3^-$, $Cl^-$ and pH. The procedure was repeated for carbon doped $ZrO_2$, sulphur doped $ZrO_2$ and carbon-sulphur doped $ZrO_2$ nanocomposites.

### 3.8 Adsorption Study of Zirconium Oxide Based Nanomaterials in the Dark

The adsorption experiment of the synthesized undoped, mono-doped and co-doped $ZrO_2$ nanoparticles were evaluated in the dark using the magnetic stirrer. 0.5 g of the undoped catalyst was added to the 50 $cm^3$ of dyeing wastewater in a 250 $cm^3$ conical flask. the conical flask was corked and kept in the dark under magnetic stirring. The mixture was stirred in the dark on a magnetic stirrer maintained at 500 rpm for 2 hours. 5 $cm^3$ of the wastewater was taken at regular time intervals (0 minutes, 30 minutes, 60 minutes, 90 minutes, 120 minutes) and filtered using Whatmann No. 1 filter paper. The adsorption of the local dyeing wastewater were evaluated by measuring COD, BOD, TOC $SO_4^{2-}$, $CO_3^{2-}$, $NO_3^-$, $Cl^-$ and pH. The procedure was repeated for carbon doped $ZrO_2$, sulphur doped $ZrO_2$ and carbon-sulphur doped $ZrO_2$ nanocomposites.

# CHAPTER FOUR

## 4.0 RESULTS AND DISCUSSION

### 4.1 HRSEM Analysis of $ZrO_2$ Based Nanomaterial

HRSEM was employed to examine the morphology of the prepared $ZrO_2$ based nanomaterial and their corresponding micrographs are shown in Plate I.

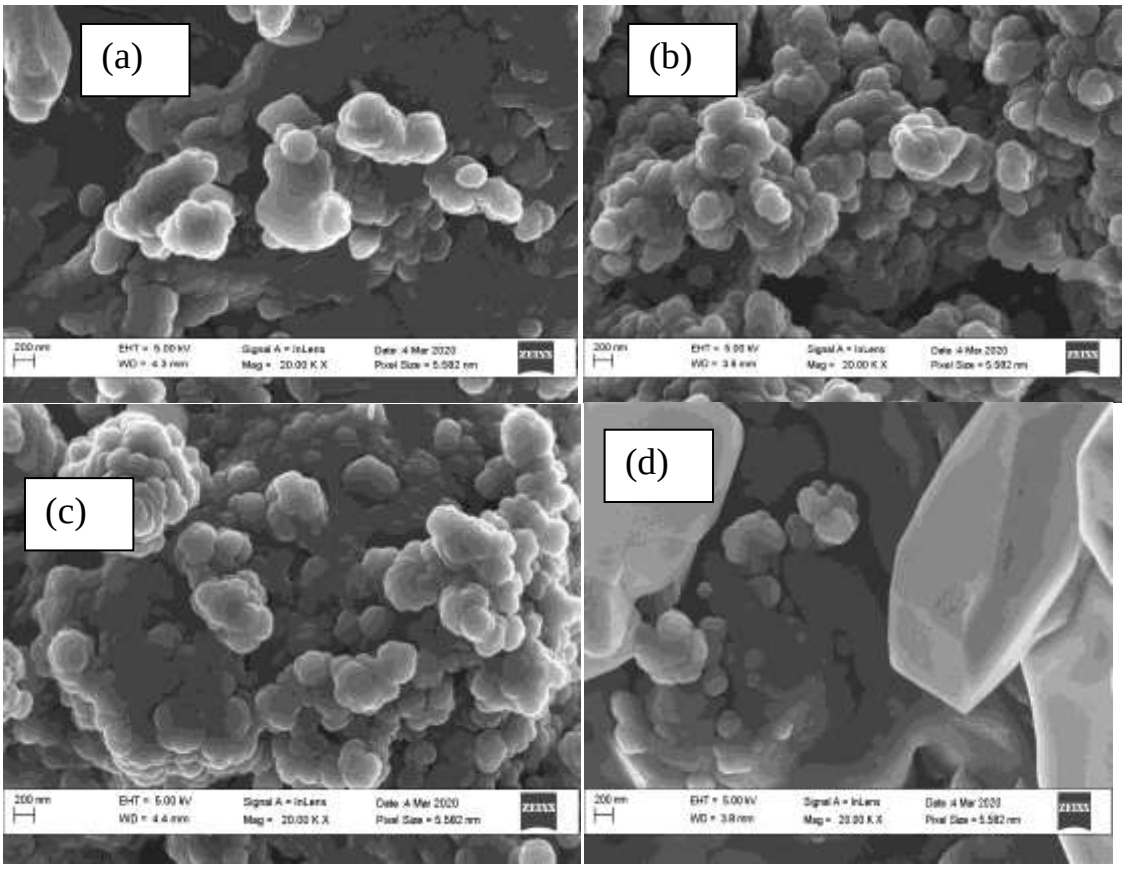


**Plate II: HRSEM Image of (a) pure $ZrO_2$ (b) $ZrO_2$ doped with 3% sulphur (c) $ZrO_2$ doped with 3% carbon (d) $ZrO_2$ co-doped with 3% carbon-sulphur**

HRSEM image of pure $ZrO_2$ nanoparticle shown in plate 1(a) revealed formation of sparsely distributed, aggregated and spherical particles with size in the range of 20.03 nm. While the HRSEM image of 3% sulphur-$ZrO_2$ nanoparticle in plate 1(b) also demonstrated the presence of well distinct homogenously distributed but agglomerated spherical particles. This degree of aggregation could be attributed to the introduction of sulphur as a dopant onto the lattice layer of $ZrO_2$ nanoparticles. The dispersion of sulphur particles on the $ZrO_2$ matirx can be explained on the basis of displacement of oxygen in $ZrO_2$ by sulphur due to greater ionic radius of sulphur (180 pm) than oxygen (80 pm). The HRSEM micrograph of 3% carbon doped $ZrO_2$ shown in plate 1(c) revealed the presence of well dispersed and aggregated dopant particles compared to

pure $ZrO_2$ nanoparticle alone. The slight change in morphological properties may be attributed to the nature of the carbonaceous material introduced onto the $ZrO_2$ matrix and substitution of oxygen by carbon based on ionic radius mechanism. The ionic radius of carbon (170 pm) is also higher than oxygen (80 pm) and thus allow easy displacement of oxygen in $ZrO_2$ by carbon. HRSEM image of 3% carbon-sulphur co-doped $ZrO_2$ in plate 1(d) revealed the presence of spherical and irregular hexagonal shape. This change in crystal structure from spherical to hexagonal may be ascribed to the co-doping phenomenon of carbon-sulphur on the lattice layer of $ZrO_2$. Arjun *et al.*, (2020) produced copper doped $ZrO_2$ nanoparticles via sol-gel method and revealed a phase change from cubic phase to spherical phase upon change in dopant concentration from 0 to 0.05 %.

## 4.2 XRD Analysis of Zirconium Oxide Nanoparticles Prepared at pH 9 and 11.

XRD techniques were employed to examine the diffraction peaks pattern and minerological phase developed at different pH. The $ZrO_2$ nanoparticles produced at pH 9 and 11 is shown in figure 4.1.

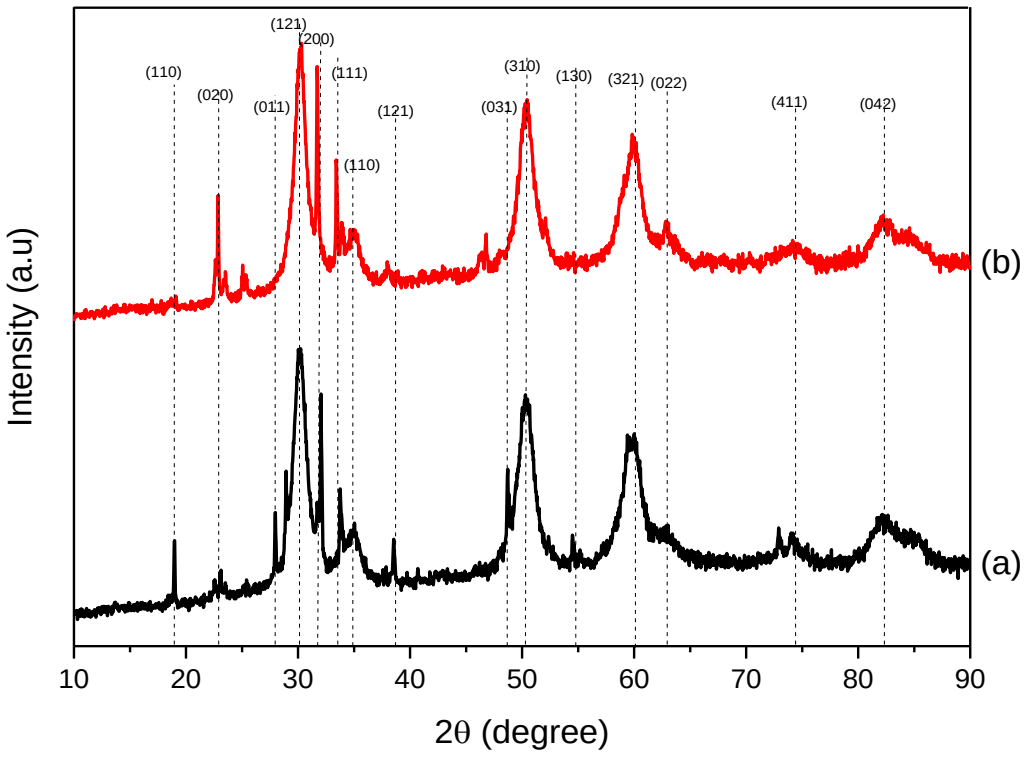


**Figure4.1: XRD pattern of $ZrO_2$ nanoparticles synthesized at (a) pH 9 (b) pH 11**

The XRD pattern in Fig. 4.1 (a) revealed three prominent diffraction peaks at 2theta values of 30.224°, 50.924°, and 62.855° which corresponds to the crystal plane (011), (310) and (231) respectively. This is in agreement with the crystallite properties of $ZrO_2$ (Renuka *et al.*, 2021). The XRD spectra also reveals a characteristic tetragonal phase according to JCP2_79-1766 card which is in agreement with Kurakaran *et al.* (2014) who employed aqueous gelation method to prepare tetragonal phase $ZrO_2$ nanoparticles. None detection of other peaks depict in the undoped $ZrO_2$ confirmed formation of pure $ZrO_2$ nanoparticles. The XRD spectra at pH 9 shows a more sharper and intense diffraction peak at 2 theta 30.22° than the XRD spectra at pH 11. At pH beyond 7, the concentration of $OH^-$ is high causing strong attraction between the positively charged $Zr^{4+}$ and ($OH^-$) in the medium, thus accelerate crystallization process and formation of a

smaller $ZrO_2$ nanoparticles. At high pH value (11), which implies high concentration of $OH^-$ in the solution, intermediate compound ($Zr(OH)_4$) predominate. However drying and calcination of the products in the furnace usually result to the formation of $ZrO_2$ of larger crystallite size. [During the doping process the hydration polymeric shell of $ZrO_2$ prepared at pH 9 collapsed faster than $ZrO_2$ prepared at pH 11 leading to a small particle size at pH9 compared to large particle size obtained at pH 11.] The crystallite size of the $ZrO_2$ nanoparticles prepared at pH 9 and pH 11 were calculated using Debye-Scherer equation in equation (4.3). The crystalline size at pH 9 was 20.03nm while the crystallite size for pH 11 was 24.18nm. The differences in the crystallite size may be linked to the degree of alkalinity. Hence, the synthesized $ZrO_2$ nanoparticle at pH 9 gave a smaller size than pH 11, thus pH 9 was used for the synthesis of sulphur doped $ZrO_2$, carbon doped $ZrO_2$ and the composite form of the two materials. This further suggests that the growth and nucleation of $ZrO_2$ nanoparticles was faster at pH 9 than pH 11. Kurakaran *et al.* (2014) obtained a crystallite size of 25nm for $ZrO_2$ nanoparticles prepared via an aqueous gelation method. The differences in crystalline size may be linked to the method of synthesis and the nature of zirconium salt precursor used. The reaction mechanism leading to the formation of the $ZrO_2$ nanoparticles starting with zirconium chloride, plant extracts and sodium hydroxide is shown as follows

$$\boldsymbol{ZrCl_4 + 4NaOH \xrightarrow{plant\ extracts} Zr(OH)_4 + 4NaCl} \qquad (4.1)$$

$$\boldsymbol{Zr(OH)_4 \xrightarrow{calcination 500^0C\ (-2H_2O)} ZrO_2} \qquad (4.2)$$

Debye scherrer equation;

$$D = \frac{K\lambda}{\beta cos\theta} \quad \text{----------(4.3)}$$

where; D= Crystalline size, λ= Wavelength

β= Half maximum diffraction peak, θ= Bragg's angle.

## 4.3 XRD Analysis of Mono and Co-doped Zirconium Oxide Nanoparticles

XRD pattern of $ZrO_2$, $ZrO_2$ doped with 3% sulphur, $ZrO_2$ doped with 3% carbon and sulphur-carbon doped $ZrO_2$ is presented in Figure 4.2.

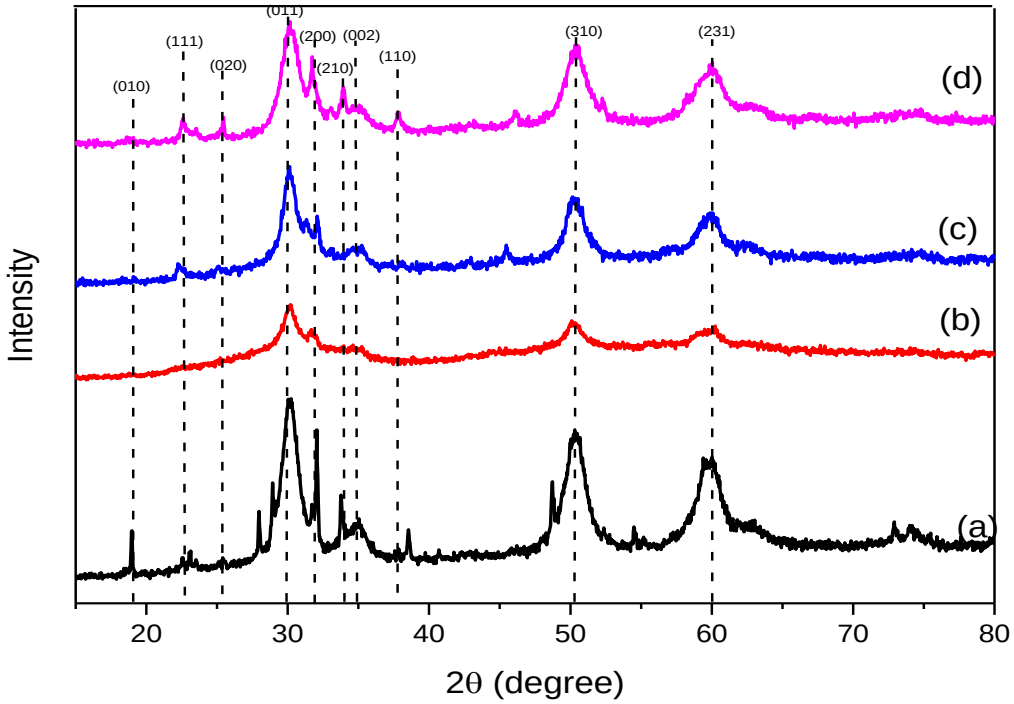


**Figure 4.2: XRD pattern of (a) $ZrO_2$ (b) $ZrO_2$ doped with 3% sulphur (c) $ZrO_2$ doped with 3% carbon (d) $ZrO_2$ co-doped with 3% carbon and sulphur.**

The XRD spectra of pure $ZrO_2$ revealed sharp diffraction peaks at 2 theta values of 30.224°, 50.924°and 62.855°, which corresponds to crystal plane (011), (310), and (231)

respectively. These peaks are characteristic properties of $ZrO_2$ nanoparticle with a tetragonal phase according to JCP2_79-1766 (Renuka *et al.,* 2021). The formation of sharp and intense diffraction peaks confirmed that the synthesized $ZrO_2$ is crystalline in nature.

On the other hand, the XRD spectra of 3% sulphur doped $ZrO_2$ shows three sharp peaks at 2 theta 30.241°, 42.978° and 62.855°which correspond to the crystal plane (011), (121) and (231) respectively of a characteristic orthorombic phase according to JCP2_83-0809 card. The phase change may be linked to excess electron in the outer shell of suphur ($2s^2$, $2p^4$) compared to zirconium with electronic configuration $4d^2$ $5s^{2.}$ The intensity of the diffraction peaks with miller indices (200) decreased remarkably due to the presence of the sulphur dopant in the matrix (Bharathi *et al.*, 2020). Anandan *et al.* (2020) found that variation in temperature from 500°C to 700°Ccaused a phase changed from monoclinic phase to tetragonal for sulphur doped $ZrO_2$ nanoparticles and reduction in intensity of its diffraction peaks pattern. The addition of sulphur also responsible for the change in orientation of $ZrO_2$ resulting to complete disappearance of diffraction peaks with miller indices (200). The phase changed observed in this work corroborated the findings of Zhang *et al.* (2019) who doped sulphur with titanium oxide to produce orthorhombic phase instead of anatase phase. Similarly, Malyi *et al*. (2011) worked on the effect of sulphur impurity on the stability of cubic Zirconium oxide and its interface with water and observed a phase change from cubic phase to tetragonal upon the addition of sulphur to the sample matrix.

The XRD spectra for 3% carbondoped $ZrO_2$ nanoparticle also revealed three sharp peaks similar to 3% sulphur doped $ZrO_2$ nanoparticles. These peaks were assigned tetragonal phase. This implies that addition of carbon did not influence the phase of

$ZrO_2$ nanoparticles because both carbon and zirconium have equal number of electron (4) in their outermost shell. Studies have shown that non-metals such as nitrogen and carbon can generate oxygen vacancy and thus, act as a stabilizer to tetragonal $ZrO_2$ nanoparticles (Bailón-García *et al.*, 2017). None distortion of tetragonal phase of $ZrO_2$ had earlier been reported by Fikhri *et al*. (2016) who doped carbon with zirconium oxide and revealed a tetragonal phase according to (JCPD_79-1771) with to evidence of phase change.

The XRD spectra of carbon/sulphur co-doped $ZrO_2$ nanocomposites revealed three prominent peaks at 2 theta values of 30.224°, 42.987° and 62.855° which correspond to crystal plane (011), (310) and (210) respectively. Also two smaller/less prominent peaks appearing at 2 theta values of 20.959° and 27.490° were attributed to the influence of co-doping of $ZrO_2$ with sulphur and carbon. Also, the co-doping effect of carbon and sulphur resulted to formation of mixed phase (tetragonal and orthorhombic) of $ZrO_2$ nanoparticle (Anandan *et al.*, 2020). This implies that the mono and co-doping influence phase change. The calculated crystallite size of the pure $ZrO_2$ nanoparticles is 20.03nm, $ZrO_2$ doped with sulphur was17.51 nm, $ZrO_2$ doped with carbon is 16.03 nm, While the co-doped $ZrO_2$ with carbon-sulphur is 12.40 nm. The doping influenced the crystallite size and the obtained size also depend on the nature of the dopants. The addition of dopants is also responsible for the reduction in the diffraction peaks pattern with miller indices (200). The peaks at 2 theta values of 22.9° dissapear due to uniform loading of carbon and sulphur in $ZrO_2$ surface, thus weakens the intensity of the peak.

Furthermore, the average grain size of $ZrO_2$ is shown in Table 4.1. The single $ZrO_2$ grain size is larger than that of the composites containing $ZrO_2$, implying that the

introduction of the dopants significantly improved the dispersion of $ZrO_2$, further enhancing the adsorptive and photocatalytic performance. Moreso, the strength and sharpness of the $ZrO_2$ characteristics (intensity) peak decrease due to the addition of the two elements. This indicates binding of carbon and sulphur onto $ZrO_2$. The comparative discussion of the chemistry of $ZrO_2$ nanoparticles based on their crystallite size is shown in Table 4.1

Table 4.1 Comparative crystallite size of $ZrO_2$ nanoparticles prepared using different methods with present study

| Authors | **Method** | **Research findings** | **Crystallite size (nm)** |
|---|---|---|---|
| Ali *et al.* (2011) | Sol-gel synthesis of copper doped $ZrO_2$ nanoparticles via the variation of dopant concentration from 0 to 0.05 % | From the photocatalytic analysis, undoped and Cu-doped $ZrO_2$ used as the catalyst for the degradation of Alizarin Yellow was found to be faster for 0.05 wt% Cu-doped $ZrO_2$ (S3) than undoped (S1) and 0.03 wt% of Cu-$ZrO_2$ (S2). The was attributed to the crystallite size of the 0.05 wt% of Cu-doped $ZrO_2$ nanoparticles | 30 |
| Kurakaran *et al.* (2014) | Synthesis and characterization of $ZrO_2$ nanoparticles prepared by aqueous gelatin method | The DSC analysis coupled with TG and structural information, indicated that the exothermic processes between 349 °C and 460°C can be attributed to the nucleation process of the formation of tetragonal zirconia | 26.5 |
| Arjun *et al.* (2020) | Synthesis and characterization of $ZrO_2$ nanoparticles by an Arc discharge method in water | Dynamic light scattering (DLS) result indicated that the size of the particles increases by increasing the arc current. Absorption spectroscopy of the samples shows a red shift on absorption edge by increasing the arc current | 25 |
| Muhammad *et al.* ( 2021) | Green synthesis and characterization of $ZrO_2$ nanoparticles by using a native *Enterobacter* sp. and its antifungal activity against bayberry twig blight disease pathogen *pestalotiopsis versicolor*. | The SEM and TEM showed the adverse effects of $ZrO_2$ against P. versicolor in terms of extracellular leakage of DNA and proteins | 33 |

| | | | |
|---|---|---|---|
| This study | Investigation of photocatalytic and adsorptive behaviour of pure $ZrO_2$ and carbon-sulphur co-doped $ZrO_2$ nanocomposite. | Carbon-sulphur co-doped $ZrO_2$ nanoparticles exhibited high photocatalytic and adsorptive efficiency in the presence and absence of natural sunlight than Carbon doped $ZrO_2$, sulphur doped $ZrO_2$ and $ZrO_2$ alone. | 16.03 |

It can be noticed from Table 4.1 that the crystallite size of carbon-sulphur co-doped $ZrO_2$ produced at pH 9 was (16.03 nm). This is smaller than the crystallite size reported in Table 4.1 and the difference in crystallite size of the nanoparticles may be attributed to the difference in methods of preparation of the $ZrO_2$ nanoparticles, surface area, band gap energy and other synthesis condition

## 4.4 HRTEM Analysis of $ZrO_2$ Based Nanomaterial

The microstructure and crystallinity nature of the samples were examined at using HRTEM Zeiss Auriga and SAED and the corresponding images are represented as Plates II

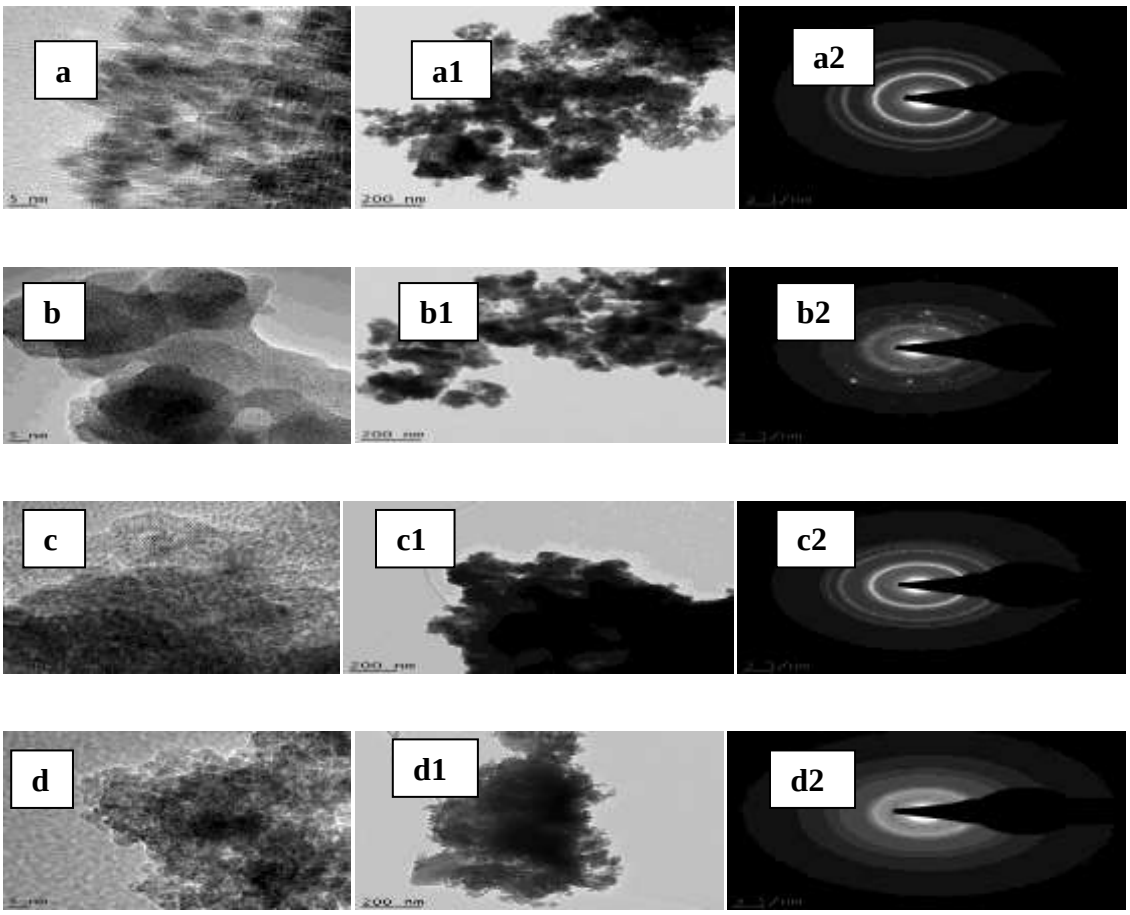


**Plate III: HRTEM images at low and high magnification and selected SAED**

**pattern of (a) pure $ZrO_2$ (b) 3% sulphur doped $ZrO_2$ (c) 3% carbon doped $ZrO_2$ (d) 3% carbon-sulphur doped $ZrO_2$**

Plate II (a and a1) shows the presence of tiny but highly agglomerated particles with lattice fringes, which reveals that the material is crystalline in nature. Plate II (b and b1) shows a tiny but more densely distributed spherical particles with lattice fringes, which is also characteristic of crystalline material. This slight change in property may be attributed to the presence of sulphur (dopant) in the sample. The appearance of densely distributed spherical nanoparticles compared to $ZrO_2$ alone further suggest phase transformation as earlier seen in the XRD result in Figure 2(b).

In the case of plate II (c and c1), tiny and highly agglomerated particle with little lattice fringes were observed. The reduction in lattice fringes indicate a slight reduction in crystallinity of the material due to the presence of carbon acting as dopant. This justified the non-phase transformation revealed in the XRD pattern in Figure 2(c)and evidence of formation of a single crystalline phase (Reddy *et al.*, 2020).Furthermore, Plate II (d and d1) revealed presence of tiny and agglomerated particles with an increase in lattice fringes which indicates an increase in crystallinity. This increase in crystallinity was linked to the co-doping effect mechanism of sulphur and carbon on the host matrix ($ZrO_2$). Also, the increase in lattice fringes corresponds to the surface exposure of the closely packed (011) crystal plane of $ZrO_2$ as indicated by Ali *et al.*, (2016) who reported controlled synthesis of $ZrO_2$ nanoparticles with tailored size morphology via organic/inorganic hybrid films'.

The SAED image in plate II(a2) revealed the presence of tiny, bright, sharp and intense ring pattern which shows that the material is highly crystalline. The ring pattern

correspond to the number of diffraction peaks observed in XRD analysis in Figure 2(a).Plate II (b2) revealed presence of bright dotted ring pattern which indicate a presence of single crystalline material The change in ring pattern from a sharp bright ring to a bright dotted ring revealed the influence of sulphur in the matrix. The formation of a single crystalline phase is an indication of phase change observed in $ZrO_2$ from tetragonal to orthorhombic in 3% sulphur- $ZrO_2$ nanoparticles.Plate II (c2) demonstrate the presence of bright dotted rings pattern indicating that the material is crystalline and the crystallinity was linked to the presence of carbon acting as dopant.

Plate 2 (d2) revealed the presence of a ransom dotted and unclear ring pattern, this indicate that the material is pollycrystalline, the change in ring pattern from a bright dotted ring to a dotted and unclear pattern indicate the influence of carbon-sulphur co-doping of the material (Shinde *et al.,* 2018). This change in ring pattern correspond with the change in crystalline phase as shown in the XRD pattern in figure 2(d).

### 4.5 EDS Analysis of $ZrO_2$ Based Nanomaterial

In order to confirm the formation of $ZrO_2$ nanoparticles, the single doped and the co-doped $ZrO_2$ nanoparticles, EDS analysis (elemental composition) was carried out and the corresponding weight percentage are shown in Figure 4.3 to determine the homogeneity and elemental composition/distribution of the sample structure.

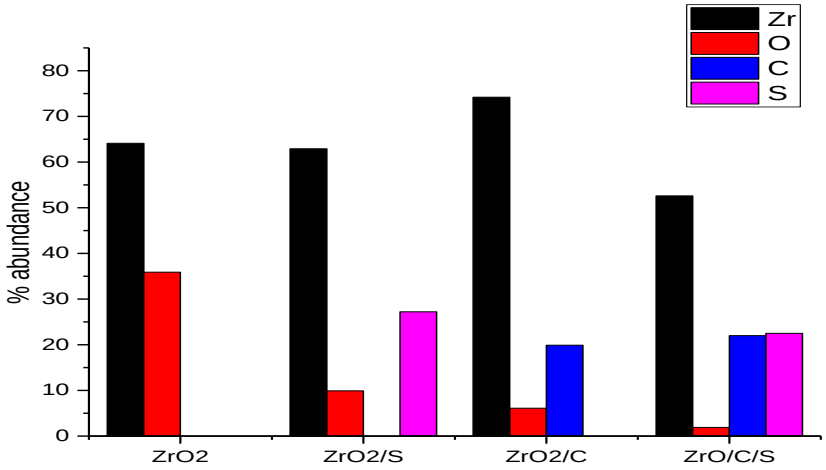


**Figure 4.3: Elemental composition for (a) pure $ZrO_2$ (b) $ZrO_2$ doped with 3% sulphur (c) $ZrO_2$ doped with 3% carbon (d) $ZrO_2$ doped with 3% carbon-sulphur.**

For the pure $ZrO_2$ nanoparticles, the following elements were detected (Zr, and O).

With Zr the most prominent and abundant. Also the presence of O confirms the sample is $ZrO_2$ nanoparticles. For the $ZrO_2$ doped with 3 % sulphur, Zr, S, and O were detected. Zr remain the most dominant, while the presence of sulphur was attributed to the $H_2S$ used as dopant. The O might be from the phytochemical constituents in the leaves extract of *Plumeria acuminata.*

The $ZrO_2$ doped with 3 % carbon revealed the presence of Zr, C and O. Zr continue to dominate the EDS, while C is present as the dopant in the sample matrix originating from pilyvinylpyrrolidone used. while O originated from the phytochemical constituents in the leaves extract of *Plumeria acuminata.*

For the co-doped $ZrO_2$ with sulphur and carbon, Zr, C, S and O were detected. The dominant nature of Zr here was slightly reduce due to the co-doping effect. The

presence of S and C is due to the dopants used, while the presence of O may be attributed to the phytochemical constituent of the leave extract of *Plumeria acuminata.*

### 4.6 UV-Visible Analysis of $ZrO_2$ Based Nanomaterial

UV-visible analysis was carried out to determine the absorption band and the band gap of $ZrO_2$ nanomaterial and the result is represented in Figure 4.4, while the Tauc plot is displayed in figure 4.5

The absorption spectrum of $ZrO_2$ nanomaterial range from 200nm to 700nm. The UV-visible spectrum of $ZrO_2$ revealed an absorption band at 302 nm. This correspond with the findings of Anku *et al.*, (2016) who observed $ZrO_2$ nanoparticle in the wavelength range of (300 nm - 366 nm). Both the UV-visible spectrum of $ZrO_2$ doped with 3%

carbon and $ZrO_2$ doped with 3% sulphur showed an absorption band at 350 nm and 345

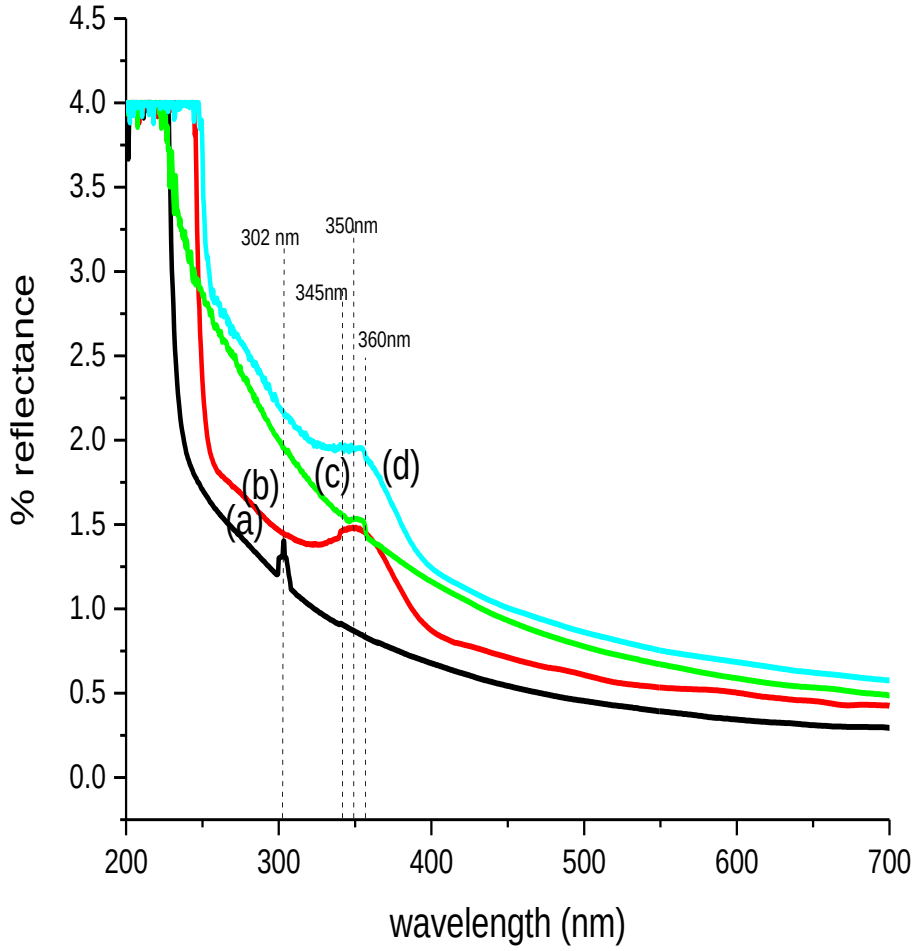


**Figure 4.4: UV-visible spectra of (a) $ZrO_2$ (b) $ZrO_2$ with 3% sulphur (c) $ZrO_2$ 3% carbon (d) $ZrO_2$ with 3% sulphur-carbon.**

nm respectively, while the UV-visible spectrum of $ZrO_2$ co-doped with carbon-sulphur revealed an adsorption band at 360 nm. The slight shift in the adsorption edge of carbon-$ZrO_2$ over $ZrO_2$ alone may be linked to the impact of quantum confinement. The shift in the adsorption band edge towards the visible region may suggest prevention of electron hole pairs from the valence band to conduction band of $ZrO_2$ nanoparticles.

This is an evidence of increase in photocatalytic efficiency from the mono doped to the co-doped $ZrO_2$ nanomaterials.

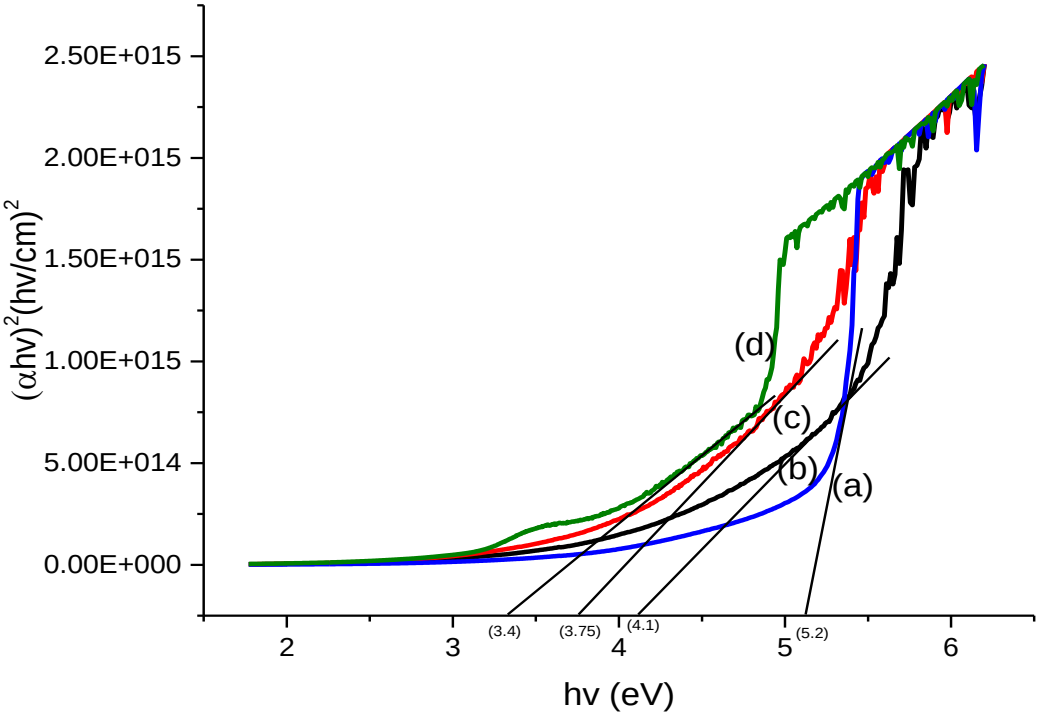


**Figure 4.5: Tauc plot of (a) $ZrO_2$ (b) $ZrO_2$ with 3% sulphur (c) $ZrO_2$ with 3% carbon (d) $ZrO_2$ with 3% sulphur-carbon.**

In order to determine the band gap of the $ZrO_2$ base nonmaterial's, the Tauc plot was introduced. The pure $ZrO_2$ spectrum revealed a band gap of 5.2eV. This corresponds to the value reported in literature for a typical $ZrO_2$ (Dharr *et al*., 2020). The band gap of $ZrO_2$ doped with 3% carbon was 3.75 eV, $ZrO_2$ doped with 3 % sulphur have a band gap of 4.1 eV while the $ZrO_2$ co-doped with 3 % sulphur-carbon revealed a band gap of 3.4 eV. The Tauc plot indicates a significant reduction on the band gap of $ZrO_2$ nanomaterial from (5.2-3.4 eV) from the mono doping to co doping activity. This is in

agreement with literature and corresponds to the findings of (Wahba *et al.,* 2020). The reduction in band gap may be due to the addition of dopants is an indication of the suppression of the electron-hole pairs recombination rate for a typical $ZrO_2$ nanoparticles. The reduction in band gap further suggest the synthesis of enhanced visible light driven $ZrO_2$ based nanocatalysts.

### 4.7 BET analysis of $ZrO_2$ based nanomateria

The BET analysis was carried out to identify the surface areas of the synthesized $ZrO_2$ nanomaterials. The surface area, pore diameter and pore volume including the adsorption-desorption curve are shown in table 4.2 and figure 4.7 respectively.

**Table 4.2: BET analysis of $ZrO_2$ based nanomaterial**

| **Sample** | **Surface area ($m^2/g$)** | **Pore diameter (nm)** | **Pore volume (cc/g)** |
|---|---|---|---|
| $ZrO_2$ | 10.682 | 16.070 | 0.157 |
| $ZrO_2$/S | 24.824 | 8.854 | 0.133 |
| $ZrO_2$/C | 52.637 | 5.293 | 0.127 |
| $ZrO_2$/S/C | 80.165 | 4.053 | 0.061 |

The result indicate that the co-doped $ZrO_2$-carbon-sulphur has the surface area ($80.165 m^2/g$) > $ZrO_2$-C ($52.637 m^2/g$) > $ZrO_2$-S ($24.824 m^2/g$) > pure $ZrO_2$ ($10.682 m^2/g$). Hence, the co-doped $ZrO_2$-carbon-sulphur have the higher tendencies to enhance a visible light driven photocatalysis and adsorption process based on the higher surface area. The increase in surface area from the mono dope to the co-doped can be attributed

to the influence of the dopant on the sample matrix. The pore diameter decrease on incorporation of the dopant from the mono-doped to the co-doped. this could also be linked to the dispersion of the dopants on the pores of the $ZrO_2$ nanomaterial (Yousefi *et al.*, 2018).

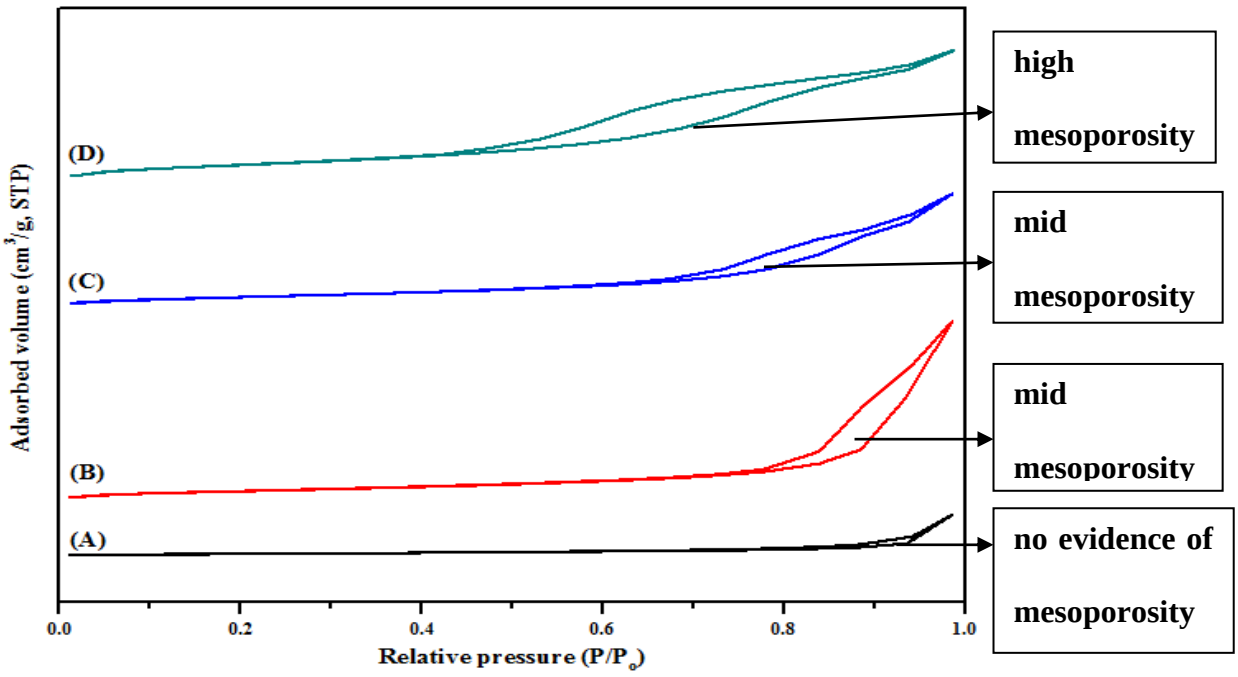


**Figure 4.6: BET spectra of (a) pure $ZrO_2$ (b) $ZrO_2$-S (c) $ZrO_2$-C (d) $ZrO_2$-S-C**

The adsorption isotherm of pure $ZrO_2$ did not show any evidence of mesoporosity. Mainwhile, on the introduction of silphur dopant, the adsorption isotherm revealed a mild mesoporosity. Also, the carbon doped $ZrO_2$ nanoparticles revealed a slight higher mesoporosity than sulphur-doped $ZrO_2$. The carbon-sulphur co-doped $ZrO_2$indicate a high mesoporosity adsorption isotherm. This increase in mesoporosity could linked to the simultaneous displacement or substitution of the two oxygen on the $ZrO_2$ matrix by carbon and sulphur. The surface area of sulphur doped $ZrO_2$ is twice that of pure $ZrO_2$ and carbon doped $ZrO_2$ is five times the pure $ZrO_2$ while the carbon-sulphur co-doped $ZrO_2$ is eight times pure $ZrO_2$. The surface area and pore volume of sulphur-$ZrO_2$, carbon-$ZrO_2$ and carbon-sulphur-$ZrO_2$ increased significantly due to the dispersed

stacking of carbon and sulphur particles on the surface of $ZrO_2$. The loading of carbon and sulphur makes the carbon-sulphur-$ZrO_2$ composite have a large surface area, which is an evidence of enhanced adsorption and photocatalytic removal of pollutant molecules in the aqueous matrix. According to the IUPAC classification, all the samples except $ZrO_2$ alone exhibits type IV adsorption isotherm, a typical of mesoporous material (Zhang *et al*., 2020). However, the degree of mesoporosity differs and depends on the nature of dopants. The existence of several mesoporous on the carbon-sulphur-$ZrO_2$ is an indication of more active sites and high adsorptive capacity. This is beneficial to the synergetic adsorption and photocatalytic reaction.

## 4.8 Physico-chemical Analysis of Local Dye Wastewater Before Photocatalytic Degradation/Adsorption Studies

The adsorption band of the local dyeing wastewater was examined using the UV-visible spectrometer and the adsorption spectra is represented in Figure 4.7. The result of the physico-chemical parameters of the dyeing wastewater is shown in Table 4.3.

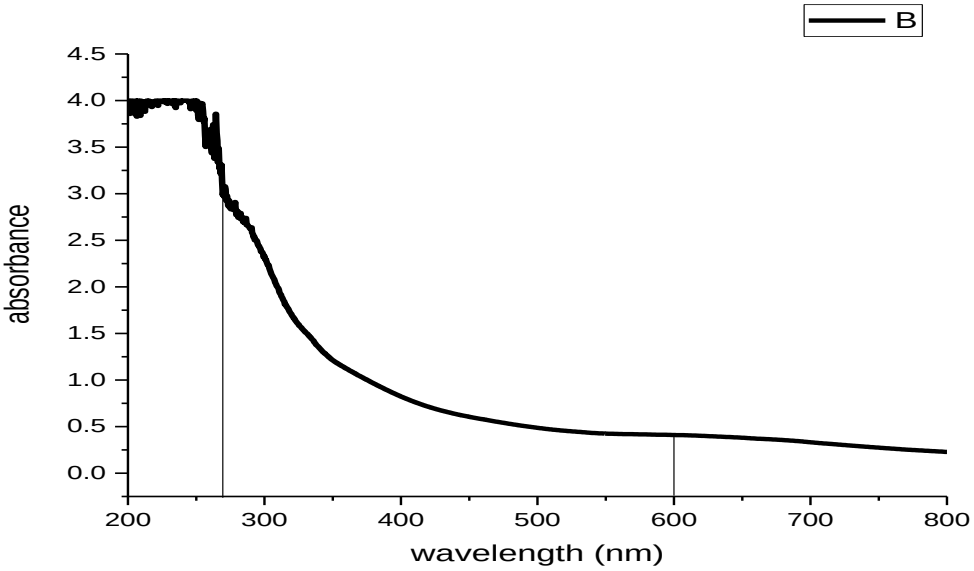

**Figure 4.7: UV-visible spectra of local dye wastewater**

The UV-visible analysis was done to identify the kind of dye present in the local dye wastewater based on the adsorption band of the spectra. The result reveals that the dye wastewater adsorbs near and within the visible region at wavelength of 270 nm and 600 nm respectively. This adsorption band fall within the adsorption range reported for azo dyes (270 nm-600 nm) (Aneyo *et al.,* 2016).

**Table 4.3: Physicochemical properties of untreated local dyeing wastewater**

| **Parameters** | **Values** | **WHO standard (2017)** | **NIS standard (2018)** |
|---|---|---|---|
| Colour | Black | Colourless | Colourless |
| Odour | Objectionable | - | - |
| pH | 8.70 | 6.5-8.5 | 6.5-8.5 |
| COD ($mg/dm^3$) | 1448 | 250 | 500 |
| BOD ($mg/dm^3$) | 670 | 50 | 50 |
| Electrical conductivity (µS/cm) | 1228 | 400 | - |
| Chloride ($mg/dm^3$) | 4200 | 250 | 250 |
| Nitrate ($mg/dm^3$) | 58.80 | 50 | 60 |
| Carbonate ($mg/dm^3$) | 3857.30 | 125-350 | 250 |
| Sulphate($mg/dm^3$) | 1634.90 | 250 | 100 |

| | | | |
|---|---|---|---|
| Total suspended solids (TSS) ($mg/dm^3$) | 450 | 500 | 500 |
| Total dissolved solids (TDS) ($mg/dm^3$) | 1521.22 | 1500-500 | 500 |
| Nitrite ($mg/dm^3$) | 41.20 | 10 | 10 |
| TOC ($mg/dm^3$) | 402 | 5 | 5 |

The results of the physico-chemical parameters of the local dye wastewater in table 4.3 reveals a very high COD, TOC and BOD values which is an indicate a presence of oxidizableorganic and inorganic dyes (Aghabeygi and Khademi-Shamami., 2018). The COD level is 1448 $mg/dm^3$ against WHO/NAFDAC standard of 50 $mg/dm^3$/500 $mg/dm^3$. This indicates high level of biological resistant substance in water. BOD level is 670 $mg/dm^3$ against 50 $mg/dm^3$ which indicate a very limited amount of oxygen for aquatic organisms in wastewater. While TOC is 402 $mg/dm^3$ against 5 $mg/dm^3$ which indicates a very high level of dissolved organic compounds in the wastewater. The nitrate, sulphate, pH and carbonate valueswere considerably higher than the WHO/NIS permissible limit.The pH value at 8.70 is slightly alkaline of which may be due to the usage of different types of dyes and the nitrogen content in the dye and the use of strong base in the dyeing process. The nitrate concentration is 58.8, about six times the recommended value. This could cause blue baby syndrome in infants and pregnant women. The sulphate level is 1634.90 $mg/dm^3$ which is too high and may cause laxative effect. The results indicates that the dye wastewater should be treated prior to release into the environment.

### 4.8.1 Photocatalytic behaviour of $ZrO_2$ based nanomaterials

The photocatalytic behaviour of the local dye wastewater was done using pure $ZrO_2$, $ZrO_2$ doped with 3% sulphur, $ZrO_2$ doped with 3% carbon and $ZrO_2$ co-doped with 3% carbon-sulphur under natural sunlight through variation of reaction time from 0 to 120 minutes. The physico-chemical parameters ( TOC, COD, BOD, $SO_4^{2-}$, $CO_3^{2-}$, $Cl^-$, $NO_3^-$, and pH) of the local dye wastewater was taking and the percentage reduction of each parameter was calculated and represented in Figures 4.8

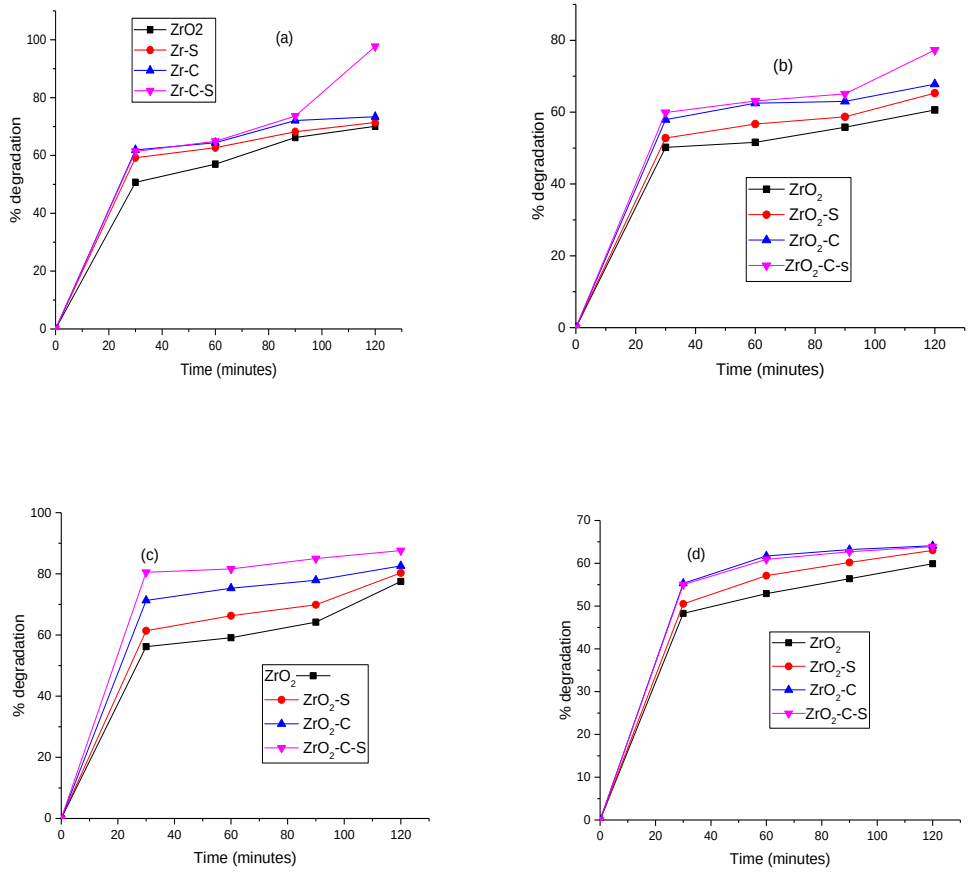

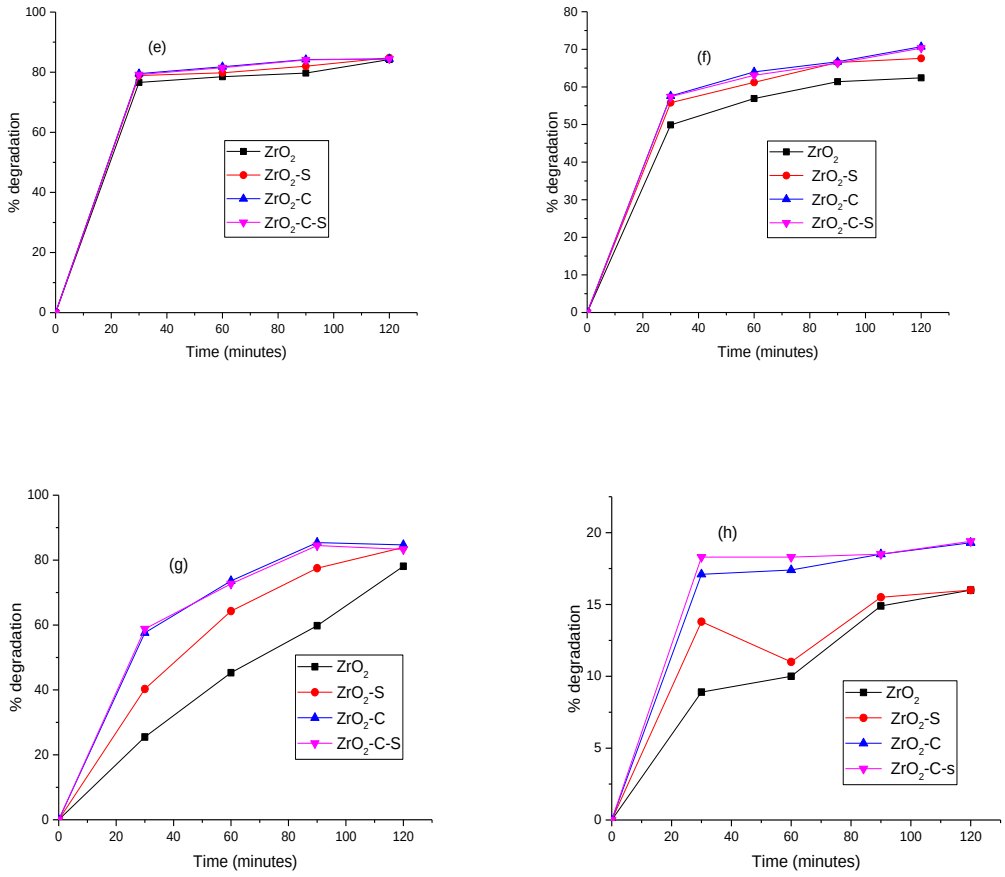


**Figure 4.8: Percentage removal efficiency (a) TOC (b) COD (c) BOD (d) $SO_4^{2-}$ (e) $CO_3^{2-}$ (f)$Cl^-$ (g) $NO_3^-$ (h) pH using (i) $ZrO_2$ alone (ii) $ZrO_2$ with 3% sulphur (iii) $ZrO_2$ with 3% carbon (iv) $ZrO_2$ with 3% carbon-sulphur.**

The photocatalytic degradation in figures 4.8 revealed that the percentage removal of the of indicator parameters increased with increase in reaction time for all the samples. The percentage degradation of the COD, BOD, TOC, $SO_4^{2-}$, $CO_3^{2-}$, $Cl^-$, $NO_3^-$ and pH with respect to nanomaterial follow this order $ZrO_2$<$ZrO_2$-S<$ZrO_2$-C<$ZrO_2$-C-S with the carbon-sulphur co-doped $ZrO_2$ exhibiting greater percentage degradation. The observed trend was attributed to the fact that the co-doped $ZrO_2$-carbon-sulphur have the least band gap (3.4 eV) and highest surface area (80.165 $m^2/g$).This corresponds to the findings of Davoodbeygi *et al.*, (2018) who investigated the photocatalytic

properties of $ZrO_2$-ZnO nanoparticles synthesized microwave irradiation. The percentage degradation of COD for carbon-sulphur co-doped $ZrO_2$ increased with increase in reaction time in the order 60.6% at 30minutes<65.3% at 60 minutes<67.8% at 90 minutes<77.3% at 120 minutes. The degradation order for BOD for carbon-sulphur co-doped $ZrO_2$was 77.5% at 30 minutes<80.3% at 60 minutes<82.6% at 90 minutes<87.6% at 120 minutes. Also the percentage degradation of TOC for carbon-sulphur co-doped $ZrO_2$ was in order of 70.1% at 30 minutes<71.4% at 60 minutes<73.4% at 90 minutes<97.7% at 120 minutes. The percentage removal of $SO_4^{2-}$ increased in the order 59.9% at 30 minutes<63% at 60 minutes<64..1% at 90 minutes<63.9% at 120 minutes. $CO_3^{2-}$increased in order of 84.2% at 30 minutes<84.8% at 60 minutes>84.45 at 90 minutes>84.4% at 120minutes. The percentage removal for $Cl^-$ increase from 62.4% at 30 minute to 67.6% at 60 minutes to 70.7% at 90 minutes and droped to 70.3% at 120 minutes. The percentage dremoval for $NO_3^-$ increased from 78.1 % at 30 minutes to 83.9 % at 60 minutes to 84.7 % at 90 minutes and reduced to 83.3 % at 120minutes. While the percentage degradation of pH was 16% at 30 and 60 minutes, increased to 19.3 at 90 minutes and to 19.4 at 120 minutes.

It was also observed that the reaction time for the removal of each indicator parameter differ with respect to the nanocatalyst. For instance, the maximum removal efficiency of. COD, BOD, TOC occurred at 120 minutes, while the removal efficiency of the anions from the dyeing wastewater were 60 and 90 minutes for $CO_3^{2,}$ $SO_4^{2-}$, $Cl^-$, $NO_3^-$for carbon-sulphur co-doped $ZrO_2$ nanocatalyst. This implies the rate of removal of the pollutants depends on their mobility for the active sites on the nanocatalyst. Thus, the catalytic efficiency of the four materials with respect to removal of pollutants from

dyeing wastewater was $ZrO_2$-S-C >$ZrO_2$-C>$ZrO_2$-S> $ZrO_2$. Hence $ZrO_2$-C-S composite have enhanced visible light driven photocatalytic activity.

Comparatively, carbon doped $ZrO_2$ exhibited slightly higher catalytic activity than sulphur doped $ZrO_2$ nanomaterial due to the difference in band gap and the surface of the nanomaterial. The nanomaterial with the higher surface area has more active sites and tendencies to absorb visible light than material with smaller surface area. The behavioural pattern of the nanocatalyst can also be linked to the phase type. For instance, carbon doped ZrO2 nanoparticles exist in monoclinic phase was photocatalytically active than orthorhombic phase obtained for sulphur doped $ZrO_2$ nanoparticles (Figure 4.2). Renuka *et al.* (2020) synthesized Mg doped $ZrO_2$ using Aloevera extract for the degradation of Rh B under UV light and found that pure $ZrO_2$ degraded 65% of the dye in 60 min and 93% degradation rate when it was doped with Mg. This study record a higher removal efficiency due to its higher surface area and lower band gap. Similar was trends were observed for other parameters in Figures 4.8 (b)-(h).

### 4.8.2 Adsorption behaviour of $ZrO_2$ nanomaterials

The adsorption studies of the local dye wastewater was carried out using pure $ZrO_2$, $ZrO_2$ doped with 3% sulphur, $ZrO_2$ doped with 3% carbon and $ZrO_2$ co-doped with 3% carbon-sulphur in the dark via the variation of reaction time from 0 to 120 minutes. The physico-chemical parameters (TOC, COD, BOD, $SO_4^{2-}$, $CO_3^{2-}$, $Cl^-$, $NO_3^-$, and pH) after the adsorption were measured and the percentage removal was calculated for each of the parameters and represented in figure 4.9

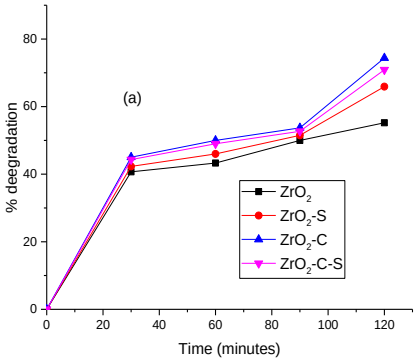
(a)
% deegradation
Time (minutes)
ZrO2
ZrO2-S
ZrO2-C
ZrO2-C-S

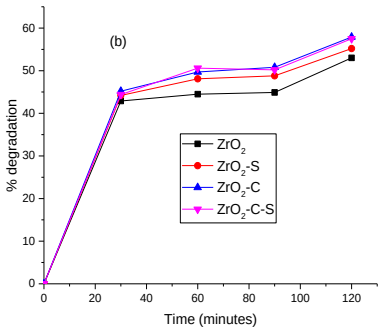
(b)
% degradation
Time (minutes)
ZrO2
ZrO2-S
ZrO2-C
ZrO2-C-S

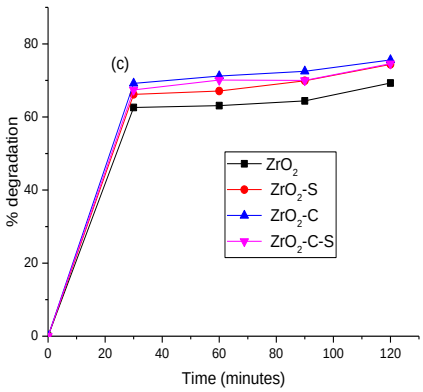
(c)
% degradation
Time (minutes)
ZrO2
ZrO2-S
ZrO2-C
ZrO2-C-S

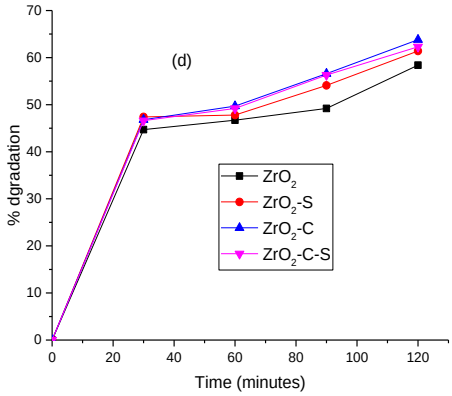
(d)
% dgradation
Time (minutes)
ZrO2
ZrO2-S
ZrO2-C
ZrO2-C-S

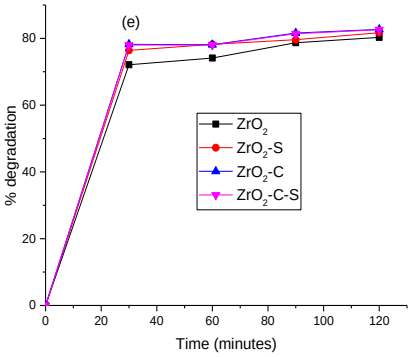
(e)
% degradation
Time (minutes)
ZrO2
ZrO2-S
ZrO2-C
ZrO2-C-S

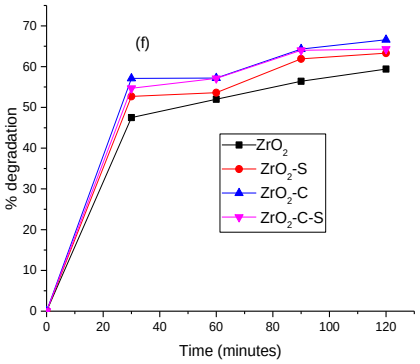
(f)
% degradation
Time (minutes)
ZrO2
ZrO2-S
ZrO2-C
ZrO2-C-S

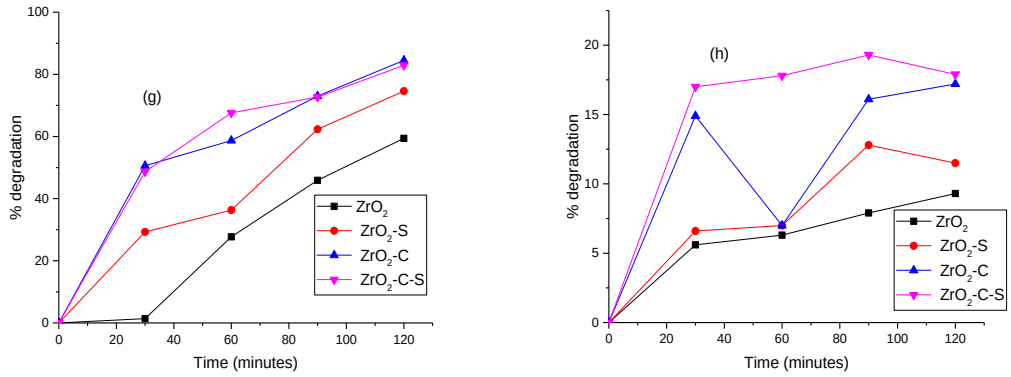


**Figure 4.9: Percentage removal efficiency (a) TOC (b) COD (c) BOD (d) $SO_4^{2-}$ (e) $CO_3^{2-}$ (f)$Cl^-$ (g) $NO_3^-$ (h) pH using (i) $ZrO_2$ alone (ii) $ZrO_2$ with 3% sulphur (iii) $ZrO_2$ with 3% carbon (iv) $ZrO_2$ with 3% carbon-sulphur.**

The plot of the adsorption behaviour of the four sample removal in figures 4.9 revealed that the percentage removal the indicator parameters increased with increasing reaction time. The percentage removal of COD, BOD, TOC, $SO_4$-2-, $CO_3^{2-}$, $Cl^-$, $NO_3^-$ and pH followed the order of $ZrO_2$<$ZrO_2$-S<$ZrO_2$-C<$ZrO_2$-C-S.The removal efficiency of the pollutants from local dyeing wastewater was ascribed to the surface area of the nanomaterials. Carbon-sulphur co-doped $ZrO_2$ which exhibit excellent percentage removal efficiency due to its high mesoporosity and surface area than others (Table 4.2). Zhang *et al.*, (2020) also reported improved photocatalytic efficiency for gully-like double-sized mesoporous structural Sr-doped $ZrO_2$–$TiO_2$ composites with degradation efficiency of 53 to70% phenol after 150 minutes. The percentage removal of COD for carbon-sulphur co-doped $ZrO_2$ increased with increase in reaction time in the order 53% at 30minutes<55.2% at 60 minutes<57.9% at 90 minutes>57.5% at 120 minutes.

The order BOD removal for carbon-sulphur co-doped $ZrO_2$ is 69.3% at 30 minutes<74.4% at 60 minutes<75.6% at 90 minutes>74.6% at 120 minutes. Also the

percentage removal of TOC for carbon-sulphur co-doped $ZrO_2$ is in order of 55.2% at 30 minutes<65.9% at 60 minutes<74.4% at 90 minutes>70.9% at 120 minutes. The percentage removal of the $SO_4^{2-}$ increased in the order 58.4% at 30 minutes<61.4% at 60 minutes<63.2% at 90 minutes>62.3% at 120 minutes. $CO_3^{2-}$ increase in order of 80.3% at 30 minutes<81.7% at 60 minutes<82.7 at 90 minutes>82.6% at 120minutes. The percentage removal for $Cl^-$ increased from 59.4% at 30 minutes to 63.3% at 60 minutes to 66.6% at 90 minutes reduced to 64.3% at 120 minutes. The percentage removal for $NO_3^-$ increased from 59.4% at 30 minutes to 74.6 % at 60 minutes to 84.5% at 90 minutes and reduced to 82.9 at 120minutes. While the percentage removal of pH was 9.3% at 30 and 11.5% at 60 minutes, increased to 17.2 % at 90 minutes and to 17.9 % at 120 minutes. Figures 4.9 indicates that carbon-sulphur co-doped $ZrO_2$behave differently with respect to the target pollutants; for instance, maximum COD, BOD, TOC, occurred within 120 minutes while maximum removal of $CO_3^{2-}$ ,$SO_4^{2-}$ , $Cl^-$, $NO_3^-$, were 60 and 90 minutes. This differences may be linked to the competition for the binding site on the nanoadsorbents by the target pollutants. Table 4.4 and 4.5 show the photocatalytic and adsorptive behaviour of the four samples after treatment of local dyeing wastewater. The obtained values after treatment were compared with WHO and NIS standards.

**Table 4.4: Physico-chemical properties of local dyeing wastewater before and after photocatalytic degradation and WHO guidlines.**

| **Parameters** | **Raw sample** | **Treatment with pure $ZrO_2$** | **Treatment with $ZrO_2$-S** | **Treatment with $ZrO_2$-C** | **Treatment with $ZrO_2$-S-C** | **WHO (2017)** | **NIS (2018)** |
|---|---|---|---|---|---|---|---|

| | | | | | | | |
|---|---|---|---|---|---|---|---|
| TOC | 402 | 1.53 | 1.41 | 1.06 | 0.93 | 5 | 5 |
| COD | 1448 | 580.64 | 534.70 | 505.01 | 415.13 | 250 | 250 |
| BOD | 670 | 130.60 | 123.15 | 100.20 | 82.80 | 50 | 50 |
| Sulphate | 1634.90 | 735.40 | 639.04 | 610.30 | 590.02 | 100 | 100 |
| Carbonate | 3857.30 | 800.12 | 712.18 | 610.02 | 603.49 | 350-125 | 250 |
| Chloride | 4200 | 1790.40 | 1550.03 | 1414.30 | 1246.22 | 250 | 250 |
| Nitrate | 58.80 | 24.20 | 16.04 | 9.12 | 9.01 | 50 | 60 |
| pH | 8.7 | 7.11 | 7.11 | 7.09 | 7.01 | 6.5-8.5 | 6.5-8.5 |

**Table 4.5: Physico-chemical properties of local dyeing wastewater before and after adsorption study with WHO and Nigerian guidelines**

| **Parameters** | **Raw sample** | **Treatment with pure $ZrO_2$** | **Treatment with $ZrO_2$-S** | **Treatment with $ZrO_2$-C** | **Treatment with $ZrO_2$-S-C** | **WHO (2017)** | **NIS (2018)** |
|---|---|---|---|---|---|---|---|
| TOC | 402 | 1.80 | 1.37 | 1.03 | 1.17 | 5 | 5 |
| COD | 1448 | 679.64 | 648.10 | 608.90 | 614.72 | 250 | 250 |
| BOD | 670 | 205.80 | 171.44 | 163.45 | 170.50 | 50 | 50 |

| | | | | | | | |
|---|---|---|---|---|---|---|---|
| Sulphate | 1634.90 | 680.86 | 630.59 | 602.14 | 616.45 | 100 | 100 |
| Carbonate | 3857.30 | 760.10 | 705.49 | 664.91 | 670.40 | 350-125 | 250 |
| Chloride | 4200 | 1704.69 | 1542.10 | 1402.57 | 1500.30 | 250 | 250 |
| Nitrate | 58.80 | 23.90 | 15.15 | 9.09 | 10.07 | 50 | 60 |
| pH | 8.7 | 7.89 | 7.70 | 7.20 | 7.14 | 6.5-8.5 | 6.5-8.5 |

Comparing the two tables (Table 4.4 and 4.5), it revealed that all the four samples have excellent photocatalytic and adsorption properties. However, 100 complete removal of the target pollutants were not achieved due to the high level of TDS and TSS which probably blocked the pores of nanoadsorbent and nanocatalyst. This prevented proper interaction of the pollutants with the active or binding sites of the four materials. In addition, the concentration of sulphates and carbonates after treatment were above the

permissible limits, this may be linked to the tendencies of inorganic anions such as $SO_4^{2-}$ and $CO_3^{2-}$ to inhibit the surface activity of photocatalyst by reducing the number of $OH^-$ available on the photoctalyst surface. This can also be explained in terms of strong competition for the active sites between the hydroxyl radicals produced by $ZrO_2$ during the photocatalysis with the radical scavengers ($SO_4^{2-}$, $NO_3^-$, $Cl^-$, $CO_3^{2-}$) in the dyeing wastewater.

It can be observed from Table 4.6 that carbon-sulphur co-doped $ZrO_2$ nanocomposites in this study compared favourably with percentage removal efficiency of 97.7% than previously reported $ZrO_2$. This was attributed to the fact that carbon-sulphur co-doped $ZrO_2$ has the highest surface area (80.16 $m^2/g$), the lowest particle size of (12.40 nm) and the lowest band gap (3.4 eV). Complete removal of the target pollutants was not achieved due to the partial blockage of active sites on the catalyst/adsorbents by the suspended solids in the local dyeing wastewater. This prevent proper interaction of the catalyst/adsorbent with the adsorbate. The differences in the behaviour of the catalyst/adsorbent may also be linked to the method of synthesizing $ZrO_2$, experimental conditions, crystallite size, surface area and functional groups. The photocatalytic and adsorptive data were subjected to different kinetic models and the results are shown in Table 4.9 and 4.10 respectively

**Table 4.6: Comparison of photocatalytic/adsorptive performance of previous synthesized $ZrO_2$ based nanomaterial with present study.**

| Author | Synthesis method | Nano catalyst | Particle size | Band gap | Surface area | % degradation | Types of Dye |
|---|---|---|---|---|---|---|---|
| Rani *et al.*, 2016 | Combustion method | GR- $ZrO_2$ | 33.9 nm | 3.32eV | 45$m^2$/g | 88% in 120 minutes | Methylene blue |
| Park *et al.*, 2019 | Sol-gel method | Ze- $ZrO_2$ | 40.80 nm | 5.6eV | 76.31$m^2$/g | 90.5% in 120 min | Methyl orange |
| Ahmed *et al.*, 2021 | Combustion method | Ag- $ZrO_2$ | 16 nm | 5.6eV | 30.406$m^2$/g | 75% in 120 minutes | Rhodamine blue |
| Uribe *et al.*, 2021 | Sol-gel | ZnO-$ZrO_2$ | 18.2 nm | 3.75eV | 8$m^2$/g | 50% in 120 minutes | Indigo red |
| This study | Green method | C-S-$ZrO_2$ | 12.40 nm | 2.6eV | 80.16$m^2$/g | 97.7% in 120minutes | Azo dye |

## 4.9 Kinetic Studies of $ZrO_2$ Based Nanocatalyst and Nanoadsorbent

### 4.9.1 Kinetic studies for the photo-catalysis of $ZrO_2$ based nanomaterials

The photocatalytic degradation of local dye wastewater was carried under natural sunlight and there was corresponding decrease in the TOC, COD, BOD, $SO_4^{2-}$, $CO_3^{2-}$, $Cl^-$, $NO_3^-$ and pH values using the synthesized pure $ZrO_2$, $ZrO_2$-S, $ZrO_2$-C and $ZrO_2$-S-C. Four different kinetic models namely zero order,pseudo first order, parabolic model and the modified freundlich model were used to describe the photodegradation of local dye wastewater under natural sunlight by the $ZrO_2$ based nanomaterials. The obtained results are represented in Table 4.7 From the results of the kinetic others obtained, the order of fitness for the prepared nanomaterials was $ZrO_2$/C/S> $ZrO_2$/S> $ZrO_2$/C> $ZrO_2$ for TOC, COD, BOD, $SO_4^{2-}$, $CO_3^{2-}$, $Cl^-$ and $NO_3^-$ in all the kinetic models used. The difference in photcatalytic performance may be due to the decrease in band gap and increase in surface area of the $ZrO_2$ nanomaterial from the mono-doped to the co-doped (Danilenko *et al.,* 2018). Based on the correlation coefficient ($R^2$), the parabolic modelbest fitted for the TOC and $NO_3^-$. This is because the correlation coefficient ($R^2$) is closer to unity in the parabolic model for TOC and $NO_3^-$. This signifies that the degradation of organic the organic dye is based on the reactive species ($OH^-$ and $O_2$). The order of fitness in terms of correlation coefficient ($R^2$) is TOC- parabolic model (0.9805)>pseudo first order (0.9711)>zero order (0.9703)>modified frendlich model (0.9642). COD- parabolic model (0.9984)>modified freundlich model (0.9934)>pseudo first order (0.9912)>zero order (0.9857). $NO_3^-$- parabolic model (0.9805)> pseudo first order (0.9711)>zero order (0.9703)>modified freundlich model (0.9642). The zero order kinetics best fitted for BOD and $Cl^-$. This signifies that, the photocatalytic degradation of the azo dyes in wastewater did not depend on the concentration of the pollutants.

This follows the order of BOD- zero order (0.996)>pseudo first order (0.9907)>modified freundlich model (0.9896)>parabolic model (0.9824). The modified freundlich model was best fitted for $SO_4^{2-}$ and $CO_3^{2-}$. This signifies that, the degradation of organic dyes occurred on photocatalyst surface before desorption in the aqueous medium and the reaction followed homogenous diffusion and adsorption-desorption mechanism. Agarwal *et al.,* (2016) also carried out the synthesis and characterization of polyaniline/$ZrO_2$ for the photocatalytic preparation of anyline using the Pseudo first order, pseudo second order, modified freundlich model and langmuir isotherm. The modified freundlich and langmuir was best fitted for the photocatalytic preparation of aniline.

### 4.9.2 Adsorption kinetics of $ZrO_2$ based nanomaterials

The adsorption studies of the organic dyes from dyeing wastewater was carried in the dark and there was corresponding decrease in the TOC, COD, BOD, $SO_4^{2-}$, $CO_3^{2-}$, $Cl^-$, $NO_3^-$ and pH values using the synthesized pure $ZrO_2$, $ZrO_2$-sulphur, $ZrO_2$-carbon and carbon-sulphur-$ZrO_2$. Four different kinetic models (zero order, pseudo first order, parabolic model and the modified freundlich model) were used to describe the adsorption of local dye wastewater unto the $ZrO_2$ based nanomaterials and the obtained result is presented in Table 4.8.

From Table 4.8, the order of fitness of the prepared $ZrO_2$ nanomaterials for TOC was $ZrO_2$<$ZrO_2$-sulphur<$ZrO_2$-carbon<$ZrO_2$-carbon-sulphur for all the kinetic models. This may be attributed to the increase in surface area and increased mesoporosity as a function of doping and co-doping. The modified frendlich model was best fit with (0.8103)>zero order (0.7368)> parabolic model (0.7344) for TOC. The order of fitness

for the other parameters is as follows. COD- freundlich (0.9597)>parabolic (0.9487)>pseudo first order (0.9203)>zero order (0.9121) with $ZrO_2$-sulphur as best suited nanomaterial. The fittness of freundlich model indicates a homogenous diffusion and the occurance of the degradation of organic dyes on the photocatalyst surface. BOD- zero order is best fitted with (0.7967)>parabolic model (0.7794)>pseudo first order (0.7708)>modified freundlich model (0.7282) with $ZrO_2$-S best suited nanomaterial. $SO_4^{2-}$- parabolic model is best fitted with (0.8922)>modified freundlich model (0.8823)>pseudo first order (0.8197)>zero order (0.8128) with $ZrO_2$-C nanomaterial having the highest correlation. $CO_3^{2-}$- parabolic model (0.9012)>modified freundlich model (0.8955)>zero order (0.8688)>pseudo first order (0.8647) with $ZrO_2$-carbon best fitted nanomaterial. For the $Cl^-$, the parabolic model was best fitted with (0.9101)>zero order (0,8744)>pseudo first order (0.8711)>modified freundlich model (o.8673) with $ZrO_2$-carbon as best fitted nanomaterial. The fitness of parabolic model for sulphate, carbonate and chloride signifies that the degradation of organic dyes through the reactive species ($OH^-$ and $O_2$) based of the diffusion mechanism. While for the $NO_3^-$, the zero order was best fitted with (0.9644)> pseudo first order (0.9622)>modified freundlich model (0.9484)>parabolic model (0.9409) with $ZrO_2$-C having the highest correlation efficiency ($R^2$). Tsegaye *et al.* (2020) carried out the synthesis and adsorption study of Fe-Al co-doped $ZrO_2$ nanocomposite using pseudo first order, pseudo second order, parabolic model and the modified freundlich model. The modified freundlich model was best fitted for the removal efficiency of cadmium and cromium ion.

**Table 4.7: Kinetic Models of Photocatalytic Behaviour of $ZrO_2$, S-$ZrO_2$, C-$ZrO_2$ and C-S-$ZrO_2$ Nanomaterials**

| Pollutant | Sample | Zero-order | | First-order | | Paraboli c | | | Modified Freundlich | |
|---|---|---|---|---|---|---|---|---|---|---|
| | | K | $R^2$ | K | $R^2$ | A | K | $R^2$ | K | $R^2$ |
| TOC | $ZrO_2$ | 0.0030 | 0.7921 | 0.0020 | 0.8099 | 0.0397 | 0.0002 | 0.8606 | 0.0118 | 0.8659 |
| | $ZrO_2$/S | 0.0034 | 0.8202 | 0.0022 | 0.8351 | 0.5758 | 0.0059 | 0.9558 | 0.0144 | 0.8893 |
| | $ZrO_2$/C | 0.0035 | 0.9503 | 0.0028 | 0.9344 | 0.8539 | 0.0098 | 0.9629 | 0.0149 | 0.9004 |
| | $ZrO_2$/C/S | 0.0048 | 0.9703 | 0.0029 | 0.9711 | 1.1358 | 0.0158 | 0.9805 | 0.0162 | 0.9642 |
| COD | $ZrO_2$ | 1.6526 | 0.9233 | 0.0025 | 0.9285 | 0.0010 | 1×10-5 | 0.8402 | 0.0107 | 0.9552 |
| | $ZrO_2$/S | 1.6705 | 0.9743 | 0.0028 | 0.9752 | 0.0012 | 2×10-5 | 0.9572 | 0.0144 | 0.9685 |
| | $ZrO_2$/C | 1.7712 | 0.9841 | 0.0031 | 0.9859 | 0.0015 | 3×10-5 | 0.9745 | 0.0177 | 0.9821 |
| | $ZrO_2$/C/S | 1.9370 | 0.9857 | 0.0034 | 0.9912 | 0.0017 | 4×10-5 | 0.9954 | 0.0244 | 0.9934 |

| | | | | | | | | | | |
|---|---|---|---|---|---|---|---|---|---|---|
| BOD | $ZrO_2$ | 0.7271 | 0.9679 | 0.0091 | 0.9332 | 0.0108 | 0.0002 | 0.6714 | 0.0175 | 0.9355 |
| | $ZrO_2$/S | 1.5873 | 0.9839 | 0.0094 | 0.9552 | 0.0125 | 0.0003 | 0.8505 | 0.0383 | 0.9516 |
| | $ZrO_2$/C | 1.7127 | 0.9959 | 0.0098 | 0.9732 | 0.0162 | 0.0004 | 0.8814 | 0.0418 | 0.9762 |
| | $ZrO_2$/S/C | 1.8478 | 0.9960 | 0.0099 | 0.9907 | 0.0183 | 0.0006 | 0.8824 | 0.0449 | 0.9896 |
| Sulphate | $ZrO_2$ | 1.2032 | 0.8890 | 0.0018 | 0.8145 | 0.0010 | $1\times10^{-5}$ | 0.8601 | 0.0142 | 0.8785 |
| | $ZrO_2$/S | 1.4069 | 0.9159 | 0.0024 | 0.9131 | 0.0014 | $2\times10^{-5}$ | 0.8899 | 0.0169 | 0.9295 |
| | $ZrO_2$/C | 1.6498 | 0.9323 | 0.0028 | 0.9151 | 0.0017 | $3\times10^{-5}$ | 0.9431 | 0.0177 | 0.9525 |
| | $ZrO_2$/S/C | 1.7367 | 0.9369 | 0.0031 | 0.9401 | 0.0019 | $4\times10^{-5}$ | 0.9449 | 0.0277 | 0.9681 |
| Carbonate | $ZrO_2$ | 5.5004 | 0.5007 | 0.0014 | 0.7799 | 0.0036 | 0.0001 | 0.8992 | 0.0010 | 0.8458 |
| | $ZrO_2$/S | 5.9813 | 0.8768 | 0.0020 | 0.9123 | 0.0038 | $2\times10^{-4}$ | 0.9335 | 0.0052 | 0.8831 |
| | $ZrO_2$/C | 6.9547 | 0.9007 | 0.0030 | 0.9250 | 0.0061 | $3\times10^{-4}$ | 0.9335 | 0.0065 | 0.9473 |

| | | | | | | | | | | |
|---|---|---|---|---|---|---|---|---|---|---|
| | $ZrO_2$/S/C | 7.7065 | 0.9577 | 0.0040 | 0.9381 | 0.0242 | $4\times10^{-4}$ | 0.9578 | 0.0090 | 0.9592 |
| Chloride | $ZrO_2$ | 2.1613 | 0.6347 | 0.0014 | 0.6372 | 0.0006 | 0.0002 | 0.8011 | 0.0091 | 0.7228 |
| | $ZrO_2$/S | 3.2516 | 0.8631 | 0.0018 | 0.7855 | 0.0008 | $4\times10^{-4}$ | 0.8543 | 0.0131 | 0.8516 |
| | $ZrO_2$/C | 3.4315 | 0.9023 | 0.0020 | 0.8782 | 0.0009 | $5\times10^{-4}$ | 0.9006 | 0.0141 | 0.9232 |
| | $ZrO_2$/S/C | 3.8707 | 0.9750 | 0.0028 | 0.9154 | 0.0381 | $8\times10^{-4}$ | 0.9327 | 0.0157 | 0.9529 |
| Nitrate | $ZrO_2$ | 0.0030 | 0.7921 | 0.0022 | 0.8099 | 0.0397 | 0.0002 | 0.8606 | 0.0118 | 0.8659 |
| | $ZrO_2$/S | 0.0034 | 0.8202 | 0.0025 | 0.8351 | 0.5758 | 0.0059 | 0.9558 | 0.0144 | 0.8893 |
| | $ZrO_2$/C | 0.0035 | 0.9503 | 0.0028 | 0.9344 | 0.8539 | 0.0098 | 0.9629 | 0.0146 | 0.9004 |
| | $ZrO_2$/S/C | 0.0048 | 0.9703 | 0.0029 | 0.9711 | 1.1358 | 0.0158 | 0.9805 | 0.0205 | 0.9642 |

**Table 4.8: Kinetic Model of Adsorptive Behaviour of $ZrO_2$, S-$ZrO_2$, C-$ZrO_2$ and C-S-$ZrO_2$ Nanomaterials.**

| Pollutant | Sample | Zero-order | | First-order | | Parabolic | | | Modified Freundlich | |
|---|---|---|---|---|---|---|---|---|---|---|
| | | K | $R^2$ | K | $R^2$ | A | K | $R^2$ | K | $R^2$ |
| TOC | $ZrO_2$ | 0.0018 | 0.7857 | 0.0013 | 0.7814 | 0.0375 | 0.0029 | 0.7305 | 0.0019 | 0.8135 |
| | $ZrO_2$/S | 0.0028 | 0.8050 | 0.0015 | 0.7999 | 0.1982 | 0.0231 | 0.8284 | 0.0034 | 0.8293 |
| | $ZrO_2$/C | 0.0054 | 0.8100 | 0.0017 | 0.8038 | 0.3190 | 0.0235 | 0.8818 | 0.0060 | 0.8600 |
| | $ZrO_2$/S/C | 0.0074 | 0.8368 | 0.0053 | 0.8170 | 0.4281 | 0.1474 | 0.8944 | 0.0319 | 0.8703 |
| COD | $ZrO_2$ | 0.2740 | 0.5464 | 0.0003 | 0.5430 | 0.0006 | 0.0003 | 0.9369 | 0.0033 | 0.6340 |
| | $ZrO_2$/S | 0.7444 | 0.6121 | 0.0012 | 0.6203 | 0.0007 | $6\times10^{-4}$ | 0.9487 | 0.0121 | 0.9597 |

| | | | | | | | | | | |
|---|---|---|---|---|---|---|---|---|---|---|
| | $ZrO_2$/C | 0.8664 | 0.7584 | 0.0017 | 0.7610 | 0.0009 | $8\times10^{-4}$ | 0.9507 | 0.0140 | 0.9650 |
| | $ZrO_2$/S/C | 0.9799 | 0.8488 | 0.0022 | 0.8475 | 0.0012 | $9\times10^{-4}$ | 0.9811 | 0.0191 | 0.9951 |
| BOD | $ZrO_2$ | 0.3888 | 0.6471 | 0.0017 | 0.6360 | 0.0009 | 0.0069 | 0.7602 | 0.0043 | 0.7506 |
| | $ZrO_2$/S | 0.4614 | 0.7967 | 0.0026 | 0.7708 | 0.0026 | 0.0078 | 0.7794 | 0.0101 | 0.7682 |
| | $ZrO_2$/C | 0.5286 | 0.8522 | 0.0027 | 0.8892 | 0.0029 | 0.0089 | 0.7851 | 0.0114 | 0.8195 |
| | $ZrO_2$/S/C | 0.6796 | 0.8925 | 0.0029 | 0.8952 | 0.0050 | 0.0096 | 0.7916 | 0.0126 | 0.8932 |
| Sulphate | $ZrO_2$ | 0.2783 | 0.5985 | 0.0003 | 0.6271 | 0.0006 | 0.0001 | 0.7503 | 0.0010 | 0.6202 |
| | $ZrO_2$/S | 0.5109 | 0.7966 | 0.0006 | 07936 | 0.0008 | $3\times10^{-4}$ | 0.8351 | 0.0053 | 0.8391 |
| | $ZrO_2$/C | 1.6019 | 0.8128 | 0.0017 | 0.8197 | 0.0012 | $6\times10^{-4}$ | 0.8922 | 0.0136 | 0.8823 |
| | $ZrO_2$/S/C | 0.9389 | 0.8977 | 0.0019 | 0.8962 | 0.0015 | 0.0009 | 0.9025 | 0.0179 | 0.8855 |
| Carbonate | $ZrO_2$ | 1.2938 | 0.7826 | 0.0016 | 0.5573 | 0.0011 | 0.0003 | 0.7712 | 0.0065 | 0.6529 |

| | | | | | | | | | | |
|---|---|---|---|---|---|---|---|---|---|---|
| | $ZrO_2$/S | 1.4740 | 0.8008 | 0.0026 | 0.7939 | 0.0014 | 0.0006 | 0.7968 | 0.0111 | 0.8580 |
| | $ZrO_2$/C | 1.5284 | 0.8688 | 0.0057 | 0.8647 | 0.0023 | 0.0008 | 0.9009 | 0.0157 | 0.8879 |
| | $ZrO_2$/S/C | 1.7323 | 0.8740 | 0.0075 | 0.8771 | 0.0031 | 0.0009 | 0.9012 | 0.0246 | 0.8955 |
| Chloride | $ZrO_2$ | 1.6675 | 0.6805 | 0.0012 | 0.6704 | 0.0055 | 0.0036 | 0.7683 | 0.0251 | 0.7588 |
| | $ZrO_2$/S | 2.6565 | 0.7740 | 0.0014 | 0.7711 | 0.0083 | 0.0058 | 0.8318 | 0.0305 | 0.8329 |
| | $ZrO_2$/C | 3.5513 | 0.7939 | 0.0021 | 0.8030 | 0.0113 | $3\times10^{-4}$ | 0.9101 | 0.0345 | 0.8673 |
| | $ZrO_2$/S/C | 4.5090 | 0.7956 | 0.0026 | 0.8806 | 0.0124 | $5\times10^{-4}$ | 0.9459 | 0.0405 | 0.8780 |
| Nitrate | $ZrO_2$ | 0.2421 | 0.8700 | 0.0063 | 0.8594 | 0.0009 | 0.0008 | 0.7015 | 0.0691 | 0.9072 |
| | $ZrO_2$/S | 0.2783 | 0.9641 | 0.0095 | 0.9622 | 0.0025 | 0.0017 | 0.7933 | 0.0771 | 0.9484 |
| | $ZrO_2$/C | 0.2800 | 09164 | 0.0181 | 0.9651 | 0.0174 | 0.0234 | 0.8409 | 0.0891 | 0.9672 |
| | $ZrO_2$/S/C | 0.3585 | 0.9212 | 0.0193 | 0.9777 | 0.0258 | 0.0553 | 0.8629 | 0.0960 | 0.9860 |

# CHAPTER FIVE

## 5.0 CONCLUSION AND RECOMMENDATIONS

### 5.1 Conclusion

The synthesis of $ZrO_2$ nanoparticles was carried out via the variation of pH using green synthesis method. The prepared zirconium doped nanomaterial were characterized for their morphology, phase structure, surface area, microstructure, absorption band, crystallinity and elemental composition using HRSEM, HRTEM, SAED, EDS,UV-visible spectroscopy, XRD, and BET. The prepared $ZrO_2$ nanomaterials were utilized as nanocatalyst and nano adsorbent to treat local dyeing wastewater.

Based on these, the following conclusion were drawn; pH 9 is the optimum pH for the synthesis of $ZrO_2$ nanoparticles. HRSEM, XRD, BET, HRTEM, UV-visible spectrometer, SAED and EDS confirmed successful incorporation of carbon and sulphur into the lattice layer of $ZrO_2$ as evidence in the reduction of band gap from 5.2 eV to 3.4 eV. The incorporation of carbon and sulphur onto the lattice layer of $ZrO_2$ enhanced the surface area in the order of sulphur-$ZrO_2$ (24.824 $m^2/g$)<carbon-$ZrO_2$ (52.637 $m^2/g$)<carbon-sulphur-$ZrO_2$ (80.165 $m^2/g$) compared to $ZrO_2$ alone with surface area. The local dyeing wastewater was found to have high amount of TOC, COD, BOD, $SO_4^{2-}$, $CO_3^{2-}$, $Cl^-$, and $NO_3^-$. and the order of photocatalytic/adsorptive performance of the four nanomaterials were carbon-sulphur co-doped $ZrO_2$> carbon doped $ZrO_2$> sulphur- doped $ZrO_2$ > $ZrO_2$. After the treatment, the carbon-sulphur co-doped $ZrO_2$ exhibited excellent adsorption and photocatalytic properties for the removal of target pollutants from local dyeing wastewater in the presence and absence of natural sunlight

TOC (97.7%), COD (77.3%), BOD (87.6%), $SO_4^{2-}$ (63.9%), $CO_3^{2-}$(84.4%), $NO_3^-$ (84.7%) and pH (19.4%) from local dyeing wastewater.

## 5.2 Recommendations

i) The synthesis condition such as the concentration of the precursor salt, variation of calcination temperature, variation of calcination time should also be varied to ascertain the optimal synthesis condition for the production of $ZrO_2$ nanoparticles.

ii) The photocatalytic parameters such as dosage, stirring speed and the volume of the wastewater should be varied to ascertain optimum condition for the photodegradation of local dye wastewater.

## REFERENCES


Agarwal, S., Tyagi, I., Gupta, V. K., Golbaz, F., Golikand, A. N., & Moradi, O. (2016). Synthesis and characteristics of polyaniline/zirconium oxide conductive nanocomposite for dye adsorption application. *Journal of Molecular Liquids*, 218, 494-498.

Aghabeygi, S., & Khademi-Shamami, M. (2018). $ZnO/ZrO_2$ nanocomposite: sonosynthesis, characterization and its application for wastewater treatment. *UltrasonicsSonochemistry*, 41, 458-465.

Agorku, E. S., Kuvarega, A. T., Mamba, B. B., Pandey, A. C., & Mishra, A. K. (2015). Enhanced visible-light photocatalytic activity of multi-elements-doped $ZrO_2$ for degradation of indigo carmine. *Journal of Rare Earths*, 33(5), 498-506.

Ahmed, T., Ren, H., Noman, M., Shahid, M., Liu, M., Ali, M. A., & Li, B. (2021). Green synthesis and characterization of zirconium oxide nanoparticles by using a native Enterobacter sp. and its antifungal activity against bayberry twig blight disease pathogen Pestalotiopsis versicolor. *NanoImpact*, 21, 100281.

Ali, S. W., Rajendran, S., & Joshi, M. (2011). Synthesis and characterization of chitosan and silver loaded chitosan nanoparticles for bioactive polyester. *Carbohydrate Polymers*, 83(2), 438-446.

Ali, Z. A., Yahya, R., Sekaran, S. D., & Puteh, R. (2016). Green synthesis of silver nanoparticles using apple extract and its antibacterial properties. *Advances in Materials Science and Engineering*, 5(3), 26-40.

Ameta, R., Solanki, M. S., Benjamin, S., &Ameta, S. C. (2018). Photocatalysis. In *Advanced Oxidation Processes for Waste Water Treatment*, 3(3) 135-175.

Anandan, K., Rajesh, K., Gayathri, K., Sharma, S. V., Hussain, S. M., &Rajendran, V. (2020). Effects of rare earth, transition and post transition metal ions on structural and optical properties and photocatalytic activities of zirconia ($ZrO_2$) nanoparticles synthesized via the facile precipitation process. *Physica E: Low-dimensional Systems and Nanostructures*, 124, 114342.

Aneyo, I. A., Doherty, F. V., Adebesin, O. A., & Hammed, M. O. (2016). Biodegradation of pollutants in waste water from pharmaceutical, textile and local dye effluent in lagos, Nigeria. *Journal of Health and Pollution*, 6(12), 34-42

Anku, W. W., Oppong, S. O. B., Shukla, S. K., Agorku, E. S., & Govender, P. P. (2016). Cobalt doped $ZrO_2$ decorated multiwalled carbon nanotube: a

promising nanocatalyst for photodegradation of indigo carmine and eosin Y dyes. *Progress in Natural Science: Materials International*, 26(4), 354-361.

Arjun, A., Dharr, A., Raguram, T., & Rajni, K. S. (2020). Study of Copper Doped Zirconium Dioxide Nanoparticles Synthesized via Sol–Gel Technique for Photocatalytic Applications. *Journal of Inorganic and Organometallic Polymers and Materials*, 30, 4989-4998.

Arreche, R., Bellotti, N., Blanco, M., & Vázquez, P. (2015). Synthesis and characterization of zirconium oxides for use as antimicrobial additives in paints. *Procedia Materials Science*, 9, 627-634.

Augustus, E. N., Samuel, A. S., Nimibofa, A., & Donbebe, W. (2017). Removal of congo red from aqueous solutions using fly ash modified with hydrochloric acid. *Current Journal of Applied Science and Technology*, 5, 1-7.

Ayanwale and Reyes-López, (2019). $ZrO_2$–ZnO nanoparticles as antibacterial agents. *ACS Omega*, 4(21), 19216-19224.

Bailón-García, E., Elmouwahidi, A., Carrasco-Marín, F., Pérez-Cadenas, A. F., & Maldonado-Hódar, F. J. (2017). Development of Carbon-$ZrO_2$ composites with high performance as visible-light photocatalysts. *Applied Catalysis B: Environmental*, 217, 540-550.

Balagangadharan, K., Chandran, S. V., Arumugam, B., Saravanan, S., Venkatasubbu, G. D., &Selvamurugan, N. (2018). Chitosan/nano-hydroxyapatite/nano-zirconium dioxide scaffolds with miR-590-5p for bone regeneration. *International Journal of Biological Macromolecules*, 111, 953-958.

Bashir, M., Riaz, S., Kayani, Z. N., & Naseem, S. (2018). Synthesis of bone implant substitutes using organic additive based zirconia nanoparticles and their biodegradation study. *Journal of the Mechanical Behavior of Biomedical Materials*, 88, 48-57.

Bharathi, E., Sivakumari, G., Karthikeyan, B., &Senthilvelan, S. (2020). Hydrothermal implement with supporting of semiconductor $ZrO_2$ (ZO), Ag doped $ZrO_2$ (AZO) nanomaterial and its astrophysical, UV photocatalytic employment on Rh6G dye. *Applied Nanoscience*, 10, 3491-3502.

Chen, S., Yin, Y., Wang, D., Liu, Y., & Wang, X. (2017).Structures, growth modes and spectroscopic properties of small zirconia clusters. *Journal of Crystal Growth*, 282(3-4), 498-505.

Choi, I., Lee, J. Y., Lacroix, M., & Han, J. (2017). Intelligent pH indicator film composed of agar/potato starch and anthocyanin extracts from purple sweet potato. *Food Chemistry*, 218, 122-128.

Danilenko, I., Gorban, O., Gorban, S., Volkova, G., Glazunova, V., &Konstantinova, T. (2018).Production of Composite $ZrO_2$-ZnO Nanoparticles Using Advanced Co-precipitation Process and Determination Their Photo-oxidative Properties by

Oxidation of C60 Fullerene. In 2018 *IEEE 8th International Conference Nanomaterials: Application & Properties (NAP)* (1-5).

Davoodbeygi, Y., & Irankhah, A. (2018). Nanostructured CeCu mixed oxide synthesized by solid state reaction for medium temperature shift reaction: Optimization using response surface method. *International Journal of Hydrogen Energy*, 43(49), 22281-22290.

Deshmukh, K., Sankaran, S., Ahamed, B., Sadasivuni, K. K., Pasha, K. S., Ponnamma, D., & Chidambaram, K. (2017). Dielectric spectroscopy.In *Spectroscopic Methods for Nanomaterials Characterization* (237-299).

Dharmaraj, N. Thenmozhi, S.,., Kadirvelu, K., & Kim, H. Y. (2012). Electrospun nanofibers: New generation materials for advanced applications. *Materials Science and Engineering: B*, 217, 36-48.

Dharr, A., Arjun, A., Raguram, T., & Rajni, K. S. (2020). Influence of pH on the structural, spectral, optical, morphological and photocatalytic properties of $ZrO_2$ nanoparticles synthesized by sol–gel technique. *Journal of Materials Science: Materials in Electronics*, 31(18), 15718-15730.

Dong, Z., Yang, Q., Mei, M., Liu, L., Sun, J., Zhao, L., & Zhou, C. (2018). Preparation and characterization of fluoride calcium silicate composites with multi-biofunction for clinical application in dentistry. *Composites Part B: Engineering*, 143, 243-249.

Eljaaly, K., Alireza, K. H., Alshehri, S., & Al-Tawfiq, J. A. (2020). Hydroxychloroquine safety: a meta-analysis of randomized controlled trials. *Travel Medicine and Infectious Disease*, 36, 101812.

Elshereksi, N. W., Ghazali, M. J., Muchtar, A., &Azhari, C. H. (2017). Studies on the effects of titanate and silane coupling agents on the performance of poly (methyl methacrylate)/barium titanate denture base nanocomposites. *Journal of Dentistry*, 56, 121-132.

Encinar, J. M., Nogales-Delgado, S., & Sánchez, N. (2021). Pre-esterification of high acidity animal fats to produce biodiesel: A kinetic study. *Arabian Journal of Chemistry*, 14(4), 103048.

Eshed, M., Pol, S., Gedanken, A., & Balasubramanian, M. (2011). Zirconium nanoparticles prepared by the reduction of zirconium oxide using the RAPET method. *Beilstein Journal of Nanotechnology*, 2(1), 198-203.

Farag, A. A. M., Hussien, M. S., &Roushdy, N. (2020). Photoelectrical and Photodegradation Characteristics Using Zirconyl Oxychloride as an Efficient Catalyst in Vario, 23, 178-198

Feng, Y., Zuo, M., Wang, T., Jia, W., Zhao, X., Zeng, X., & Lin, L. (2019). Efficient synthesis of glucose into 5-hydroxymethylfurfural with $SO_4^{2-}/ZrO_2$ modified H+ zeolites in different solvent systems. *Journal of the Taiwan Institute of Chemical Engineers*, 96, 431-438.

Fakhri, H., Mahjoub, A. R., & Aghayan, H. (2017). Effective removal of methylene blue and cerium by a novel pair set of heteropoly acids based functionalized graphene oxide: Adsorption and photocatalytic study. *Chemical Engineering Research and Design*, 120, 303-315.

Gautam, C., Joyner, J., Gautam, A., Rao, J., & Vajtai, R. (2016). Zirconia based dental ceramics: structure, mechanical properties, biocompatibility and applications. *Dalton Transactions*, 45(48), 19194-19215.

Ghosh, S., Santhosh, R., Jeniffer, S., Raghavan, V., Jacob, G., Nanaji, K., & Grace, A. N. (2019). Natural biomass derived hard carbon and activated carbons as electrochemical supercapacitor electrodes. *Scientific Reports*, 9(1), 1-15.

Gurushantha, K., Renuka, L., Anantharaju, K. S., Vidya, Y. S., Nagaswarupa, H. P., Prashantha, S. C., & Nagabhushana, H. (2017). Photocatalytic and photoluminescence studies of $ZrO_2$/ZnO nanocomposite for LED and waste water treatment applications. *Materials Today Proceedings*, 4(11), 11747-11755.

Hu, C., Sun, J., Long, C., Wu, L., Zhou, C., & Zhang, X. (2019). Synthesis of nano zirconium oxide and its application in dentistry. *Nanotechnology Reviews*, 8(1), 396-404.

Huang, Z., Wang, Z., Li, C., Yin, K., Hao, D., &Lan, J. (2018). Application of Plasma Sprayed Zirconia Coating in Dental Implant: Study in Implant. *The Journal of Oral Implantology*, 29, 303-416.

Iqbal, J., Shah, N. S., Sayed, M., Khan, J. A., Muhammad, N., Khan, Z. U. H., & Polychronopoulou, K. (2020). Synthesis of nitrogen-doped Ceria nanoparticles in deep eutectic solvent for the degradation of sulfamethaxazole under solar irradiation and additional antibacterial activities. *Chemical Engineering Journal*, 394, 124869.

Iqbal, J., Shah, N. S., Sayed, M., Muhammad, N., Khan, J. A., Khan, Z. U. H., & Polychronopoulou, K. (2020). Deep eutectic solvent-mediated synthesis of ceria nanoparticles with the enhanced yield for photocatalytic degradation of flumequine under UV-C. *Journal of Water Process Engineering*, 33, 101012.

Ismael, M., Wu, Y., &Wark, M. (2019). Photocatalytic activity of $ZrO_2$ composites with graphitic carbon nitride for hydrogen production under visible light. *New Journal of Chemistry*, 43(11), 4455-4462.

Jabir, M. S., Taha, A. A., & Sahib, U. I. (2018). Linalool loaded on glutathione-modified gold nanoparticles: a drug delivery system for a successful antimicrobial therapy. *Artificial Cells, Nanomedicine, and Biotechnology*, 46(2), 345-355.

Jaramillo-Páez, C., Navío, J. A., Hidalgo, M. C., &Macías, M. (2017).High UV-photocatalytic activity of ZnO and Ag/ZnO synthesized by a facile method. *Catalysis Today*, 284, 121-128.

Jimenez, M., Guin, T., Bellayer, S., Dupretz, R., Bourbigot, S., & Grunlan, J. C. (2016). Microintumescent mechanism of flame-retardant water-based chitosan–

ammonium polyphosphate multilayer nanocoating on cotton fabric. *Journal of Applied Polymer Science*, 133(32).

Kaliraj, L., Ahn, J. C., Rupa, E. J., Abid, S., Lu, J., & Yang, D. C. (2019). Synthesis of panos extract mediated ZnO nano-flowers as photocatalyst for industrial dye degradation by UV illumination. *Journal of Photochemistry and Photobiology B: Biology*, 199, 111588.

Kaviya, S. (2020).Evolution of ZnO-Based Photocatalyst for the Degradation of Pollutants. In *Green Photocatalysts for Energy and Environmental Process* (109-139).

Kianfar, A. H., Arayesh, M. A., &Momeni, M. M. (2021). Degradation of MB and RhB by modified $ZrO_2$ nanoparticles via sunlight. *Applied Physics A*, 127(2), 1-9.

Kucio, K., Sydorchuk, V., Khalameida, S., &Charmas, B. (2020). Mechanochemical and microwave treatment of precipitated zirconium dioxide and study of its physical– chemical, thermal and photocatalytic properties. *Journal of Thermal Analysis and Calorimetry*, 1-10.

Kurakaran, S., George, A., & Nair, A. S. (2014). Synthesis and characterization of zirconium oxide nanoparticle prepared by aqueous gelation method. *Journal of the Indian Chemical Society*, 91(1), 47-52.

Lin, K., Xing, J., Quan, L. N., de Arquer, F. P. G., Gong, X., Lu, J., & Wei, Z. (2018). Perovskite light-emitting diodes with external quantum efficiency exceeding 20 per cent. *Nature*, 562(7726), 245-248.

Luengas, A., Barona, A., Hort, C., Gallastegui, G., Platel, V., & Elias, A. (2015). A review of indoor air treatment technologies. *Reviews in Environmental Science and Bio/Technology*, 14(3), 499-522.

Mahtabian, S., Yahay, Z., Mirhadi, S. M., & Tavangarian, F. (2020). Synthesis and Characterization of Hierarchical Mesoporous-Macroporous $TiO_2$-$ZrO_2$ Nanocomposite Scaffolds for Cancellous Bone Tissue Engineering Applications. *Journal of Nanomaterials*, 72, 75-80.

Malyi, O. I., Chen, Z., Shu, G. G., & Wu, P. (2011). Effect of sulfur impurity on the stability of cubic zirconia and its interfaces with metals. *Journal of Materials Chemistry*, 21(33), 12363-12368.

Melchor-Lagar, V., Ramos-Ramírez, E., Morales-Pérez, A. A., Rangel-Vázquez, I., & Del Angel, G. (2020).Photocatalytic removal of 4-chlorophenol present in water using $ZrO_2$/LDH under UV light source. *Journal of Photochemistry and Photobiology A: Chemistry*, 389, 112251

Mishra, S., Debnath, A. K., Muthe, K. P., Das, N., &Parhi, P. (2021). Rapid synthesis of tetragonal zirconia nanoparticles by microwave-solvothermal route and its photocatalytic activity towards organic dyes and hexavalent chromium in single and binary component systems. *Colloids and Surfaces A: Physicochemical and Engineering Aspects*, 608, 125551.

Mondal, S., Reyes, M. E. D. A., & Pal, U. (2017). Plasmon induced enhanced photocatalytic activity of gold loaded hydroxyapatite nanoparticles for methylene blue degradation under visible light. *RSC Advances*, 7(14), 8633-8645.

Muhammad, Z., Ali, F., Sajjad, M., Ali, N., Bilal, M., Shaik, M. R., & Khan IV, M. (2021). Zirconium-Doped Chromium IV Oxide Nanocomposites: Synthesis, Characterization, and Photocatalysis towards the Degradation of Organic Dyes. Catalysts 2021, 11, 117.

Munawar, T., Iqbal, F., Yasmeen, S., Mahmood, K., & Hussain, A. (2020). Multi metal oxide NiO-CdO-ZnO nanocomposite–synthesis, structural, optical, electrical properties and enhanced sunlight driven photocatalytic activity. *Ceramics International*, 46(2), 2421- 2437.

Muthuchudarkodi, R. R., & Vedhi, C. (2014). Preparation and electrochemical characterization of manganese dioxide-zirconia nanorods. *Applied Nanoscience*, 5(4), 481-491.

Muya, F. N., Sunday, C. E., Baker, P., & Iwuoha, E. (2016). Environmental remediation of heavy metal ions from aqueous solution through hydrogel adsorption: a critical review. *Water Science and Technology*, *73*(5), 983- 992.

NIS (Nigerian Industrial Standard),(2018) Nigerian standard or Drinking Water Quality, NIS 554:2007, ICS 13.060.20, Approved by the Standard Organisation of Nigeria (SON) Governing Council, pp: 14-18.

Noviyanti, A. R., Rahayu, I., & Fauzia, R. P. (2021). The effect of Mg concentration to mechanical strength of hydroxyapatite derived from eggshell. *Arabian Journal of Chemistry*, 14(4), 103032.

Ossai, C. I., &Raghavan, N. (2018).Nanostructure and nanomaterial characterization, growth mechanisms, and applications. *Nanotechnology Reviews*, 7(2), 209-231.

Park, S., & Shao, G. (2019). Microstructure and Materials Characterization of Sol-Gel Synthesized ZrO2 Systems. *Tanzania Journal of Science*, 45(2), 190-208.

Pei, X., Ma, L., Zhang, B., Sun, J., Sun, Y., Fan, Y., & Zhang, X. (2017). Creating hierarchical porosity hydroxyapatite scaffolds with osteoinduction by three-dimensional printing and microwave sintering. *Biofabrication*, 9(4), 045008.

Rajendran, S., Annadurai, G., & Rajeshkumar, S. (2018). Characterization and toxicology evaluation of zirconium oxide nanoparticles on the embryonic development of zebrafish, Danio rerio. *Drug and Chemical Toxicology*, 42(1), 104-111.

Rajesh, G., Akilandeswari, S., Govindarajan, D., & Thirumalai, K. (2020). Enhancement of photocatalytic activity of ZrO 2 nanoparticles by doping with Mg for UV light photocatalytic degradation of methyl violet and methyl blue dyes. *Journal of Materials Science: Materials in Electronics*, 31(5), 4058-4072.

Rani, S., Aggarwal, M., Kumar, M., Sharma, S., & Kumar, D. (2016). Removal of methylene blue and rhodamine B from water by zirconium oxide/graphene. *Water Science*, 30(1), 51-60.

Reddy, C. V., Reddy, I. N., Ravindranadh, K., Reddy, K. R., Kim, D., & Shim, J. (2020).Ni- dopant concentration effect of $ZrO_2$ photocatalyst on photoelectrochemical water splitting and efficient removal of toxic organic pollutants. *Separation and Purification Technology*, 252, 117352.

Renuka, L., Anantharaju, K. S., Gurushantha, K., Nagabhushana, H., Vidya, Y. S., Suresh, C., &Sennappan, M. (2021). Phase-transformation synthesis of Li codoped $ZrO_2$ Eu3+ nanomaterials: Characterization, photocatalytic, luminescent behaviour and latent fingerprint development. *Ceramics International*, 47(7), 10332-10345.

Rozana, M., Tan, W. K., Matsuda, A., &Lockman, Z. (2017). Characterizations and photoelectrochemical properties of $Fe_2O_3$ and $ZrO_2$ nanotubes formed by anodic oxidation process.In *AIP Conference Proceedings* 1865(1), 020007.

Saraswathi, V. S., &Santhakumar, K. (2017). Photocatalytic activity against azo dye and cytotoxicity on MCF-7 cell lines of zirconium oxide nanoparticle mediated using leaves of Lagerstroemia speciosa. *Journal of Photochemistry and Photobiology B: Biology*, 169, 47-55.

Sartale, D., &Gophane, A. (2019). Santosh B. Babar, Nana L. Gavade, Dhanaji P. Bhopate, Abhijit. N. Kadam, Sanjay B. Kokane, Shrikrishna. *J Mater Sci: Mater Electron*, 30, 1133-1147.

Sasaki, H., Hamanaka, I., Takahashi, Y., & Kawaguchi, T. (2017).Effect of reinforcement on the flexural properties of injection-molded thermoplastic denture base resins. *Journal of Prosthodontics*, 26(4), 302-308.

Sigwadi, R., Dhlamini, S., Mokrani, T., &Nonjola, P. (2017).Effect of synthesis temperature on particles size and morphology of zirconium oxide nanoparticle. In *Journal of Nano Research* 50, 18-31.

Shinde, H. M., Bhosale, T. T., Gavade, N. L., Babar, S. B., Kamble, R. J., Shirke, B. S., & Garadkar, K. M. (2018). Biosynthesis of $ZrO_2$ nanoparticles from Ficusbenghalensis leaf extract for photocatalytic activity. *Journal of Materials Science: Materials in Electronics*, 29(16), 14055-14064.

Shooto, N. D., Ayawei, N., Wankasi, D., Sikhwivhilu, L., & Dikio, E. D. (2016). Study on cobalt metal organic framework material as adsorbent for lead ions removal in aqueous solution. *Asian Journal of Chemistry*, 28(2), 277.

Song, W., Anselmo, A. C., & Huang, L. (2019). Nanotechnology intervention of the microbiome for cancer therapy. *Nature Nanotechnology*, 14(12), 1093-1103.

Stolzenburg, P., Freytag, A., Bigall, N. C., & Garnweitner, G. (2016). Fractal growth of $ZrO_2$ nanoparticles induced by synthesis conditions. *CrystEngComm*, 18(43), 8396-8405.

Sun, J., Kormakov, S., Liu, Y., Huang, Y., Wu, D., & Yang, Z. (2018). Recent progress in metal-based nanoparticles mediated photodynamic therapy. *Molecules*, 23(7), 1704.

Tamm, A., Joost, U., Mikkor, M., Kalam, K., Mändar, H., Seemen, H., & Kukli, K. (2017). Properties of zirconium oxide and cobalt ferrite layered nanocomposite. *ECS Journal of Solid State Science and Technology*, 6(12), P886.

Taufik, A., Tju, H., Prakoso, S. P., & Saleh, R. (2018). Different routes of synthesized CdO nanoparticles through microwave-assisted methods and photocatalytic study. In *AIP Conference Proceedings* 2023(1), 020035

Tharani, S. S. N. (2013). Green synthesis of zirconium dioxide ($ZrO_2$) nano particles using Acalypha indica leaf extract. *International Journal of Engineering and Applied Sciences*, 3(4), 257689.

Tsegaye, F., Taddesse, A. M., Teju, E., & Aschalew, M. (2020). Preparation and sorption property study of Fe3O4/Al2O3/ZrO2 composite for the removal of cadmium, lead and chromium ions from aqueous solutions. *Bulletin of the Chemical Society of Ethiopia*, 34(1), 105-121.

Uribe, M., Lemus, M. A., Hidalgo, M. C., López, R., Quintana, P., Oros, S., ... & Acosta, J. Structural and Optical Characterization of ZnO-ZrO2 Nanocomposites for Photocatalytic Degradation and Mineralization of Phenol 123, 35-64

Vattikuti, S. P., Devarayapalli, K. C., Nagajyothi, P. C., & Shim, J. (2019). Binder-free $WS_2/ZrO_2$ hybrid as a photocatalyst for organic pollutant degradation under UV/simulated sunlight and tests for $H_2$ evolution. *Journal of Alloys and Compounds*, 809, 151805.

Wahba, M. A., Yakout, S. M., Mohamed, W. A., &Galal, H. R. (2020). Remarkable photocatalytic activity of Zr doped ZnO and $ZrO_2$/ZnO nanocomposites: Structural, morphological and photoluminescence properties. *Materials Chemistry and Physics*, 256, 123754.

Wang, Q., Edalati, K., Koganemaru, Y., Nakamura, S., Watanabe, M., Ishihara, T., & Horita, Z. (2020). Photocatalytic hydrogen generation on low-band gap black zirconia ($ZrO_2$) product

World Health Organization. (2017). Safely managed drinking water: thematic report on drinking water 2017.

Yadav, P., Dwivedi, P. K., Tonda, S., Boukherroub, R., &Shelke, M. V. (2020). Metal and non-metal doped metal oxides and sulfides. In *Green Photocatalysts* (89-132).

Yaghoubi, A., Ramazani, A., &Taghavi F, S. (2020). Synthesis of $Al_2O_3/ZrO_2$ Nanocomposite and the Study of Its effects on Photocatalytic Degradation of Reactive Blue 222 and Reactive Yellow 145 Dyes. *Chemistry Select*, 5(32), 9966-9973.

Yang, W., Prabhakar, R. R., Tan, J., Tilley, S. D., & Moon, J. (2019). Strategies for enhancing the photocurrent, photovoltage, and stability of photoelectrodes for photoelectrochemical water splitting. *Chemical Society Reviews*, 48(19), 4979-5015.

Yungjun C., Lunsford, S. K., Song, Y., Ju, H., Falaras, P., Kontos, A. G., & Dionysiou, D. D. (2010). Synthesis, characterization and electrochemical properties of mesoporous zirconia nanomaterials prepared by self-assembling sol–gel method with Tween 20 as a template. *Chemical Engineering Journal*, 170(2-3), 518-524.

Yousefi, R., Beheshtian, J., Seyed-Talebi, S. M., Azimi, H. R., &Jamali-Sheini, F. (2018).Experimental and theoretical study of enhanced photocatalytic activity of Mg-doped ZnO NPs and ZnO/rGO nanocomposites. *Chemistry–An Asian Journal*, 13(2), 194- 203.

Zarei, M., Bahrami, J., & Zarei, M. (2019).Zirconia nanoparticle-modified graphitic carbon nitride nanosheets for effective photocatalytic degradation of 4-nitrophenol in water. *Applied Water Science*, 9(8), 1-11.

Zhang, K., Zhou, M., Yu, C., Yang, K., Li, X., Dai, W., & Huang, W. (2020). Construction of S-scheme g-$C_3N_4$/$ZrO_2$heterostructures for enhancing photocatalytic disposals of pollutants and electrocatalytic hydrogen evolution. *Dyes and Pigments*, 180, 108525.

Zhang, X., Li, L., Zhou, Q., Liang, X., & Liu, D. (2019).Facile synthesis of novel gully-like double-sized mesoporous structural Sr-doped $ZrO_2$–$TiO_2$ composites with improved photocatalytic efficiency. *Journal of Solid State Chemistry*, 269, 375-385.

Zhang, X., Li, L., Wen, S., Luo, H., & Yang, C. (2017). Design and synthesis of multistructured three-dimensionally ordered macroporous composite bismuth oxide/zirconia: Photocatalytic degradation and hydrogen production. *Journal of Colloid and Interface Science*, 499, 159-169.

## APPENDICES

Appendix A: TOC

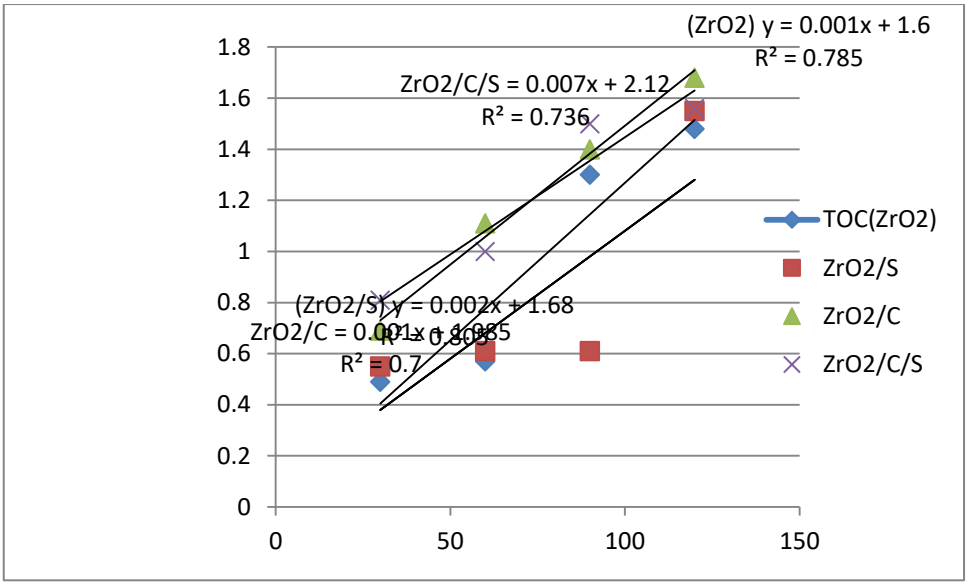


Apendix B: COD

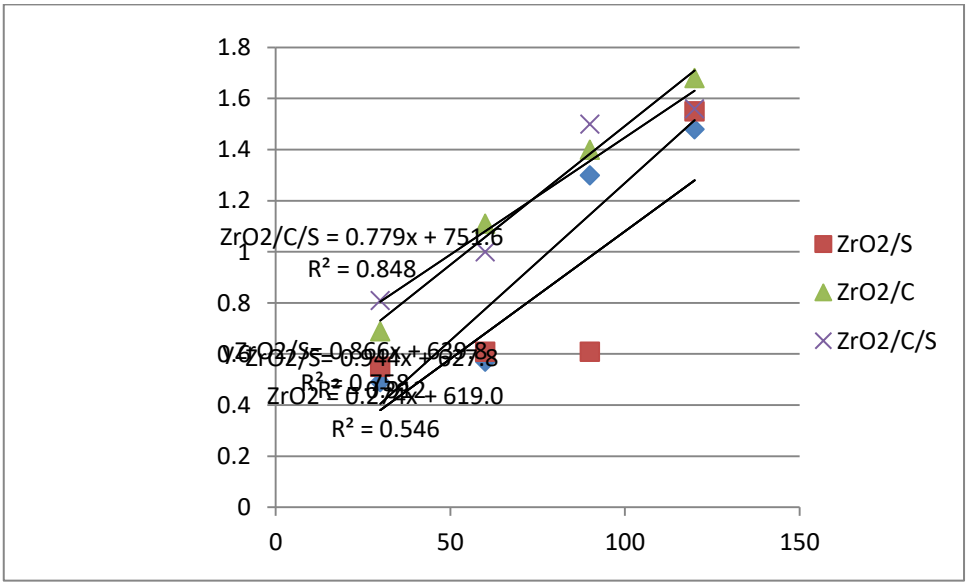

Appendix C: BOD

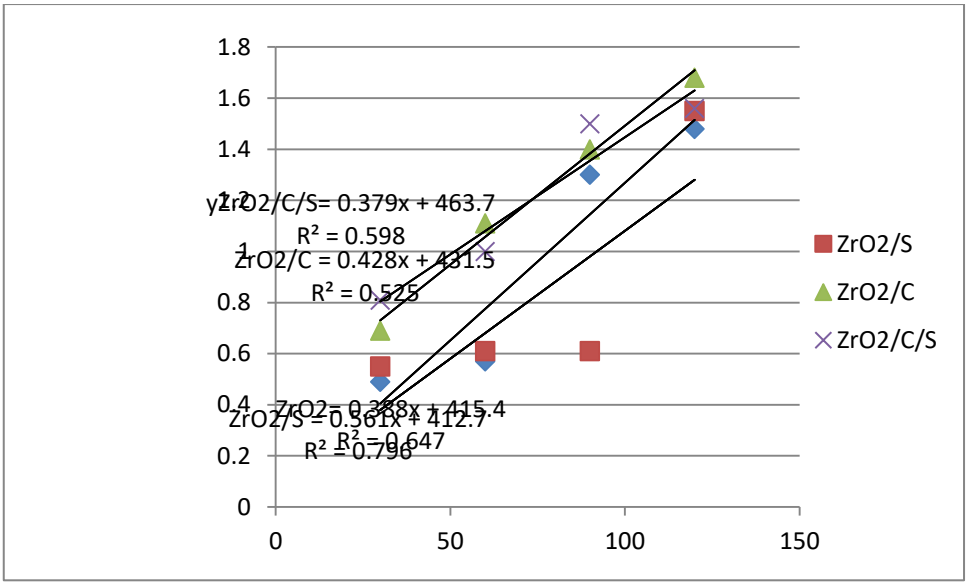


Appendix D: $NO_3^-$

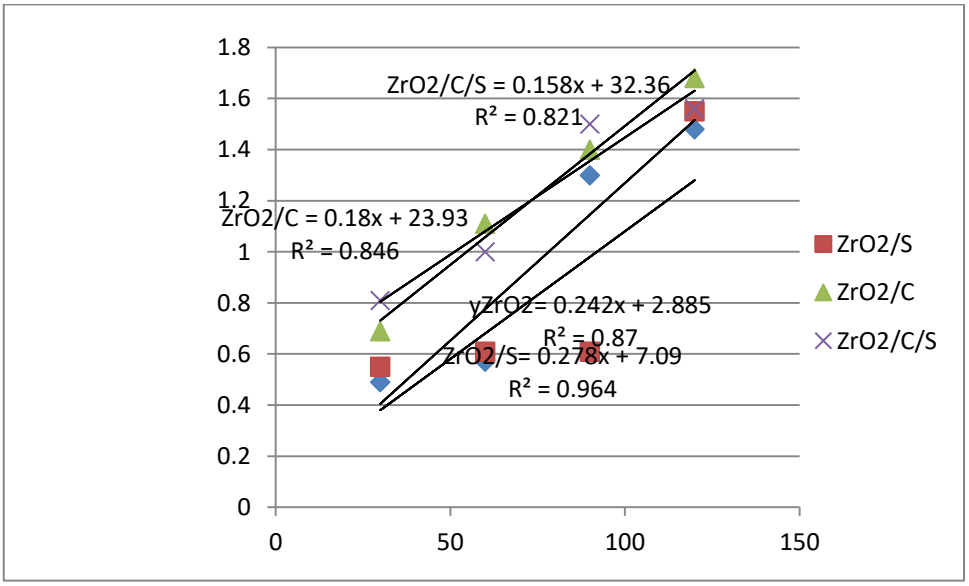

Appendix E: $Cl^-$

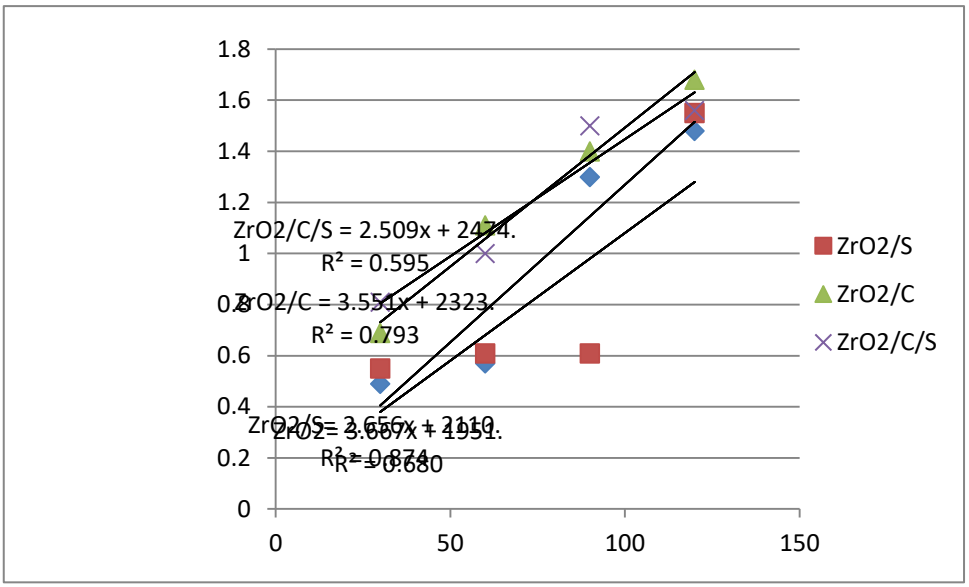


Appendix F: $CO_3^{2-}$

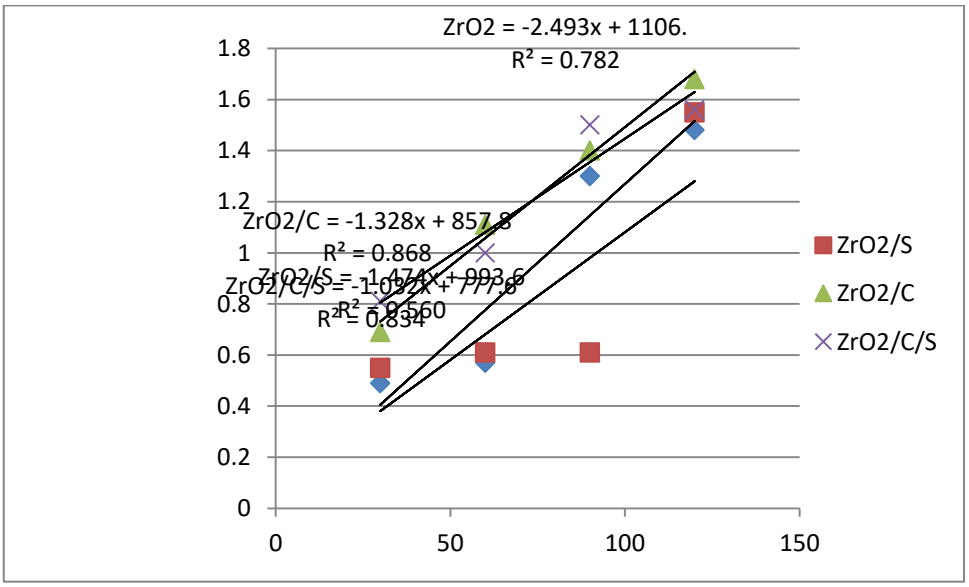

Appendix G: $SO_4^{2-}$

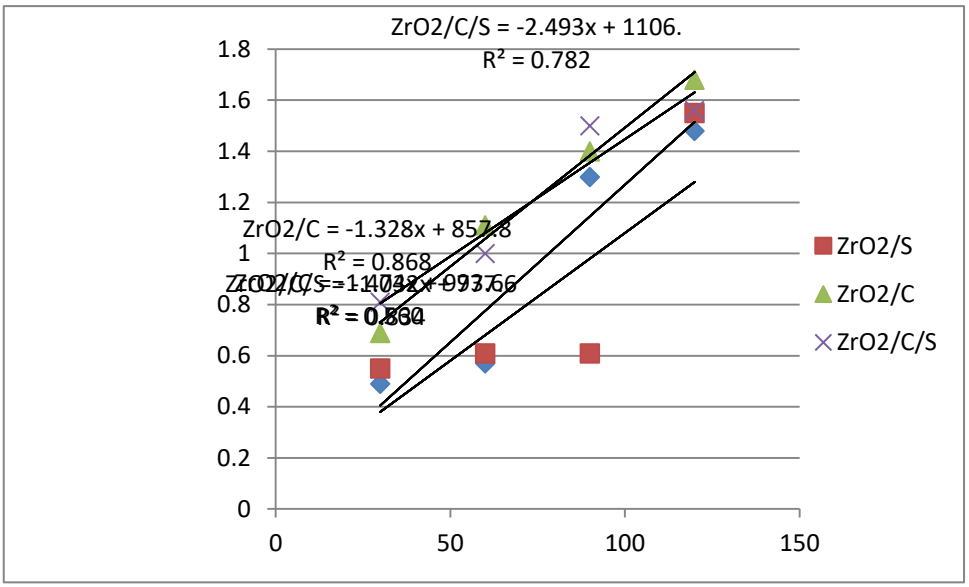


Appendix H: pH